Interannual variability of tropical upper tropospheric humidity and cloud: Current climate variation and future climate change

By

Hui-Wen Chuang

A dissertation submitted in partial fulfillment
of the requirements for the degree of
Doctor of Philosophy
(Atmospheric, Oceanic, and Space Science)
in The University of Michigan
2012

Doctoral Committee:

Assistant Professor Xianglei Huang, Chair
Assistant Professor Mark G. Flanner
Associate Professor Christopher J. Poulsen
Professor Richard B. Rood

Acknowledgements

This dissertation would not have been possible without many people's help and encouragement.

First and foremost, I own my deepest gratitude to my advisor, Prof. Xianglei Huang, for his support, patience and generosity. He has shown me an excellent role model of his broad knowledge and enthusiasm in science. It is my greatest fortune to be his first PhD student. With his support and encouragement, I have been able to attend as many conferences and workshops as I can during these five years. Without his guidance and help, I would not have finished this study. Thank you.

I would also like to thank my other dissertation committee members: Professors Mark Flanner, Christopher Poulsen, and Richard Rood for their time to evaluate my research work. I also greatly appreciate Drs. Hui Su and Jonathan Jiang for their support and help when I worked as a summer intern at NASA JPL in my second PhD year.

I am grateful to my classmates and colleagues who have helped my inside and outside of the AOSS. Thank you, my friends. We have spent wonderful time together and I really enjoy your company which makes my PhD life much more delightful.

Last but not least, many thanks to my dear family. Without your confidence in me and encouragement all the years, I wouldn't have been here today. I love you.

Table of Contents

List of Figures

List of Tables

Abstract

The theme of this research is to study the tropical water vapor and clouds, especially their relation with the large-scale environment at the interannual time scale as well as their changes in the future climate. The study employs extensive data analysis with high-quality satellite observations that have not been made available until recently, the NCEP and ECMWF reanalyses and the model simulations archived for the CMIP (coupled-model intercomparison project) phase-3 and phase-5 projects. A simple radiative-convective equilibrium (RCE) model is also used to interpret some of the analysis results.

The current interannual variability of tropical upper tropospheric humidity (UTH) is examined. The correlation between UTH and SST anomalies over the tropical convection region is found to be generally higher than that between the UTH and the SST anomalies over the entire tropics, corroborating the role of deep convection in the vertical transport of moisture. The variability over each tropical ocean basin is investigated and reveals the discrepancies between models and observations on such regional-scale variability. How the atmospheric bridge and the tropical eastern Pacific affect the climate in other basins is further highlighted.

Though each GCM-simulated ice water path (IWP) differs from others by a factor ~10, this study shows that the models agree much better on the fractional variation of IWP with vertical velocity at 500 hPa (ω_{500}). The models and observations also agree on such a fractional change. Moreover, a relation can be found between the interannual

variability in the current climate and the projected long-term future change regarding the IWP and ω_{500} anomalies. It can be estimated that over the tropical Pacific region, such a relation projects a ~3.38±0.42% decrease of IWP associated with circulation change due to every 1K global warming, which can then imply a ~0.37Wm^{-2} decrease in the net atmospheric absorption of radiation. The contribution of radiative cooling to the circulation change based on a RCE framework and NOAA GFDL simulations are further examined. The change of vertical velocity, which is inferred from this simple RCE framework, is consistent with what the GFDL GCM simulated. For the middle and lower troposphere, the changes of the lapse rate and of the clear-sky radiative cooling are equally important for weakening of the circulation.

Chapter 1

Introduction

1.1 Background

As a consequence of the evolution of our habitable planet, water exists in all three phases in our atmosphere concurrently. All three phases are radiatively active and crucial to the radiation budget at both the top of atmosphere (TOA) and the surface. The latent heat due to the phase transitions of water fuels the moist dynamics of atmospheric motions. Water vapor strongly absorbs over a vast spectral range of infrared (IR), making it the most important greenhouse gas in our atmosphere. Among all of the greenhouse gases, water vapor accounts for 75% of the total terrestrial greenhouse effect [*Lacis et al.*, 2010]. Without the greenhouse effect, the surface temperature of the earth would be 33K lower than its present value [*Smil*, 2003; *Le Treut et al.,* 2007]. For the same reason, water vapor also provides a strong positive feedback that amplifies the surface warming which is due to the increase of anthropogenic greenhouse gases. The condensed phases of water, i.e. clouds, generally enhance the greenhouse effect of the atmosphere by their strong IR absorptions. Meanwhile, they also cool the atmosphere by their strong

reflection of shortwave radiation back into space (the cloud albedo is usually much higher than that of the surface). These opposite radiative effects at longwave and shortwave, together with the tight coupling between clouds, large-scale circulation and cloud microphysics, makes understanding cloud change in future climate one of the most challenging, yet imperative, tasks [*Stephens*, 2005; *Sherwood et al*., 2010; and references therein].

One particular interest and focus over the last two decades is the tropical upper tropospheric humidity (UTH). The attention to tropical UTH can be dated back to *Lindzen* [1990], which raised concerns about the limitation of our understanding and modeling capacity of UTH and its feedback. This research motivated a series of studies on both the sources and sinks of tropical UTH as well as the estimation of its feedback [to name a few, *Betts*, 1990; *Salathe and Hartmann*, 1997; *Held and Soden* 2000; *Soden et al*., 2002; *Minschwaner and Dessler*, 2004; *Soden et al.,* 2005; *Dessler et al.*, 2008]. From a Lagrangian trajectory point of view, the large-scale distribution of UTH can be largely understood by the concept of "the last time of saturation" [*Sherwood,* 1996b; *Pierrehumbert and Roca*, 1998; *Dessler and Sherwood*, 2000; *Pierrehumbert et al.*, 2007; *Wright et al*., 2009]. The source of UTH is mainly from the tropical deep convection that inject boundary layer moisture directly into the upper troposphere [*Betts and Albrecht*, 1987; *Sun and Lindzen*, 1993; *Udelhofen and Hartmann*, 1995; *Soden and Fu*, 1995; *Sherwood*, 1996b; *Pierrehumbert*, 1998; *Pierrehumbert and Roca*, 1998; *Dessler and Sherwood*, 2000; *Wright et al.*, 2009].

More attention has been paid to tropical high clouds since the debates about the tropical thermostat, a hypothesis proposed by *Ramanathan and Collins* [1991]. It was

argued that high clouds would exert a negative feedback due to the strong reflection of shortwave radiation that limits further warming of sea surface temperatures (SST) underneath the high clouds. Follow-up studies on both sides of the debate deepened our understandings of the tropical high clouds, its role in tropical energy balance, tropical circulation and future climate change, as well as the challenges in observing the long-term change of such clouds [*Fu et al*., 1992; *Hartmann and Michelsen*, 1993; *Pierrehumbert*, 1995; *Hartmann et al.,* 2001; *Hartmann and Larson*, 2002; *Wielicki et al.*, 2002; *Wong et al*, 2006]. The complicated relations between SST and cloud distribution have been studied in detail and the role of dynamics has been taken into account [*Wallace*, 1992; *Fu et al*., 1992; *Lindzen et al*., 2001; *Hartmann and Michelsen*, 2002; *Lin et al*., 2002; *Su et al*., 2008a]. Several studies in the last decades focused on understanding the change of high cloud top pressure (height) in future climate [*Hartmann and Larson,* 2002; *Kuang and Hartmann*, 2007; *Zelinka and Hartmann*, 2010]. They proposed that the temperature of the convective anvil cloud top remains roughly constant in a warmer climate and thus longwave cloud altitude feedback is robustly positive. *Zelinka et al*. [2011] proposed a new kernel technique to efficiently estimate cloud feedback by perturbing a joint distribution function of cloud top and cloud optical depth. They showed that changes in high clouds produce largely opposite feedbacks at longwave and shortwave and that the spread of these two opposite feedbacks of high clouds is larger than that of low cloud. Though low cloud is deemed as a major uncertainty of climate feedbacks, these results indicate a potentially large uncertainty in both the longwave and shortwave feedbacks of high clouds. These studies stress the important radiative role of high clouds in the current climate and future climate change.

In spite of these studies over the last two decades, there are still a few interesting questions left unanswered that are pertinent to future climate change. For example, correlations between UTH and SST over the entire tropics are high and often discussed in relevant studies. However, tropical upper troposphere can only directly communicate with the surface over deep convective regions via convection "pipeline" pumping moistures from near surface to the upper troposphere. On the other hand, SST over tropical subsidence regions has no direct connection with the UTH at all. Therefore, it is interesting to explore further why, overall, such a high correlation exists between the UTH and the entire tropical SST. Though global climate model (GCM) simulations largely agree with each other on the increase of tropical mean UTH and precipitation for the future climate change, the regional patterns from different GCMs still show considerable discrepancies. Simulations of ice water cloud in the GCMs still pose a major challenge: GCMs differ in their ice water path (IWP) by a factor as large as 10 [*Waliser et al.,* 2009; also shown in Figure 1.1]. Such a large difference was not alleviated in the most recent CMIP5 output (the fifth phase of the Coupled-Model Intercomparison Project, the lower two rows of Figure 1.1), which is the modeling archive for the upcoming IPCC (Intergovernmental Panel on Climate change) assessment report. Moreover, very little attention has been paid to the interannual variations of IWP and its connections with interannual variations of dynamic fields with similar discrepancies that exist in the satellite-based observations of IWP over the tropics [*Wu et al.,* 2009]. Furthermore, IWP feedback has not been fully studied. Even though we have some understanding about how the cloud altitude will change (e.g. the FAT hypothesis proposed by *Hartmann and Larson* [2002] and PHAT hypothesis by *Zelinka and Hartmann* [2010]), how the cloud

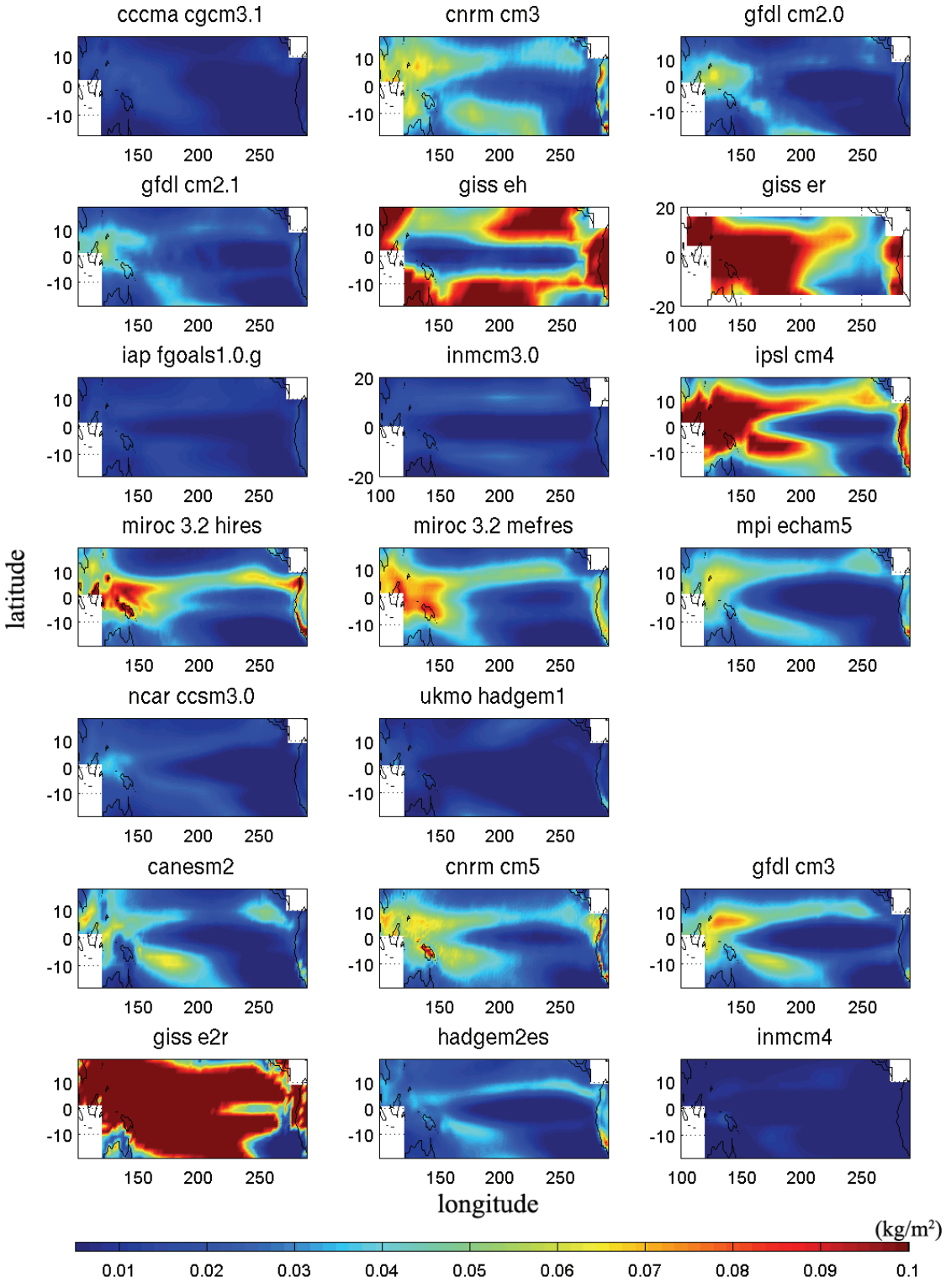

Figure 1.1. The climatological mean (Jan 1980 – Dec 1999) of ice water path distribution at tropical Pacific from 20 GCMs. Fourteen of them (the upper five rows) are from CMIP3 and six of them (the lower two rows) are from CMIP5. Full name of these GCMs can be found at Table 4.a.1.

amount or cloud water content will change is not studied equally. The links between hydrological and circulation changes, especially over the interannual timescale, remain a frontier for further study.

Climate variability related to the El Niño/Southern Oscillation (ENSO) has coherent and structural changes in temperature and hydrological variables. ENSO is the dominate mode of interannual variability for the tropics. ENSO events are useful for analyzing the climate responses and for evaluating climate feedbacks [*Soden*, 1997; *Dessler et al*., 2008]. To understand and correctly simulate the interannual variations of tropical UTH/clouds, especially with the response to variations of surface temperature and dynamic/thermodynamic variables, is particularly important for a complete understanding of the atmospheric branch of hydrological cycle. It is also beneficial to explore the relation between current climate variability and future climate changes. Based on arguments rooted in the equilibrium statistical mechanics, it has been long speculated that the fluctuation of climate system (i.e. variability) is related to its dissipative behavior (i.e. response to external forcing such as anthropogenic CO_2) [*Leith*, 1975; *Bell*, 1980; *North et al.*, 1993; *Cionni et al.*, 2004]. Studies on the snow albedo feedback show a close relationship between simulated strengths of snow albedo feedback with the amplitudes of seasonal cycles of snow albedo [*Qu and Hall*, 2006; *Hall and Qu*, 2006]. Therefore, it is also intriguing to explore whether the simulated ENSO behavior can be related to the simulated future climate change.

1.2 Limitations of traditional measurements

Though the important roles played by the UTH and high clouds have been recognized for decades, we are still lacking a comprehensive understanding of connections between

UTH/high clouds and many other components in the climate system [*Randall et al*., 2007]. One of the major reasons is the lack of long-term high-confidence UTH and high cloud measurements with the desired temporal and spatial coverages. Although radiosonde measurements can provide the longest record of UTH, they are known to be unreliable at cold temperatures (~above 300 hPa) and suffer instrument-dependent biases in the upper troposphere [*Soden and Lanzante*, 1996; *Miloshevich et al*., 2001; *Miloshevich et al*., 2004; *Miloshevich et al.,* 2006]. As a consequence, large discrepancies among radiosonde observations, GCMs and reanalysis data on the relations between interannual anomalies of tropical mean water vapor and temperature have been noticed for decades [*Sun and Held*, 1996; *Sun et al.* 2001; *Huang et al.*, 2005; *Chen et al*., 2008b]. The main advantage of using satellite measurements, comparing to radiosonde measurements, is their global coverage. High-resolution Infrared Radiation Sounder (HIRS) aboard the National Oceanic and Atmospheric Administration (NOAA) operational polar-orbiting satellites has been providing global radiance measurements since 1978. However, due to its coarse spectral resolution, the NOAA HIRS (6.7 μm narrow-band water vapor channel) can only provide a layer-averaged humidity weighted over a broad layer (~ 500-200 hPa). Additionally, clouds largely attenuate radiance at IR channels so studies using HIRS observations must be restricted to cloud-free areas [*Bates and Jackson,* 2001; *Soden et al*., 2005]. Better observations of UTH and high clouds are crucial for us to advance our understandings of the roles played by them in the current and future climate.

1.3 A golden era of data analysis

The advances in observations and modeling during the last two decades have been

enormous. With the accumulation of these datasets, it is worthwhile to revisit some unanswered questions mentioned in the previous section with a synergistic use of observations, models and reanalyses. This section reviews the advances in observations and the improvements in reanalyses and modeling, setting the stage for the analyses in following chapters.

1.3.1 Advances in satellite observations

The Atmospheric Infrared Sounder (AIRS) is a high spectral resolution grating spectrometer aboard NASA's Aqua satellite launched in May 2002. With 2378 channels covering mid-IR to near-IR spectral range at a resolving power of 1200 (i.e. $\frac{\lambda}{\Delta\lambda} = 1200$), AIRS provides retrieval of UTH at a much higher vertical resolution than that of HIRS. For example, Figure 1.2 shows the six-year averages of AIRS humidity at 200 and 250

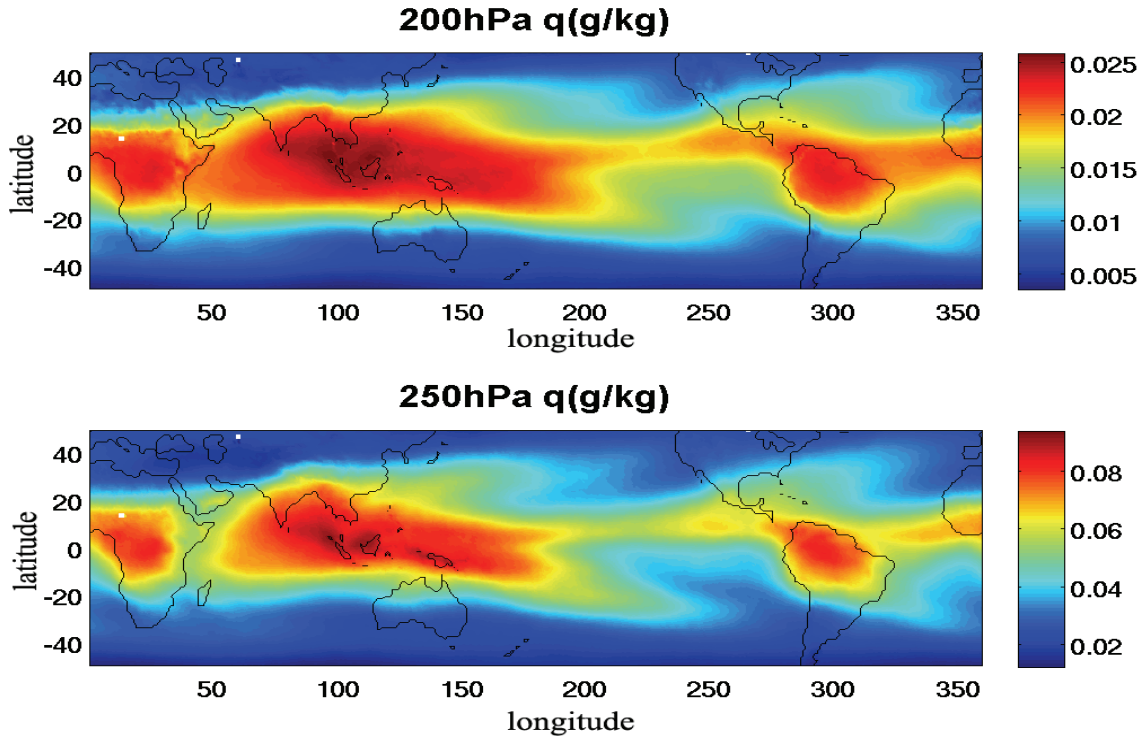

Figure 1.2. The distribution of climatological mean AIRS specific humidity at 200 and 250 hPa from Jan 2003 to Dec 2008.

hPa. The high concentration of the UTH is within 20°S-20°N with maxima over the region known for frequent occurrence of deep convection (e.g. central Africa, South America, Maritime Continents, the Inter-Tropical Convergence Zone (ITCZ), and the South Pacific Convergence Zone (SPCZ)). A unique advantage of AIRS is its retrieval of temperature and humidity in the presence of clouds. Using a cloud-clearing technique [*Chahine*, 1974], AIRS is capable of retrieving temperature and humidity profiles below clouds in the presence of up to 70% cloud coverage [*Susskind et al*., 2006].

The Earth Observing System (EOS) Microwave Limb Sounder (MLS) aboard the Aura satellite was launched in July 2004. It employs the limb-viewing technique and offers better accuracy for cloud detection at high altitudes [*Schoeberl et al*., 2006; *Waters et al*., 2006]. Unlike IR sounders, most clouds do not affect the microwave sounder as long as the cloud's particle size is much smaller than the wavelength of microwave radiation. Therefore, MLS can provide a more comprehensive distribution of UTH for both cloudy and cloud-free regions. The 240GHz radiance of MLS measurement also provides reliable retrievals of ice water content (IWC) in the upper troposphere [*Wu et al.,* 2006]. The six-year-mean UTH and IWC at 215 hPa from MLS retrievals are shown in Figure 1.3. The distribution of the UTH resembles that of IWC very well, indicating the tight connection between water vapor and high clouds.

Both AIRS and MLS instruments have been stable since the starting of operation. Several cycles of data reprocessing have been done to ensure the integrity of data and to correct any identified issues. Therefore, nine years of AIRS data and seven years of MLS data can be used with large confidence for the study of interannual variations of tropical UTH and UT clouds.

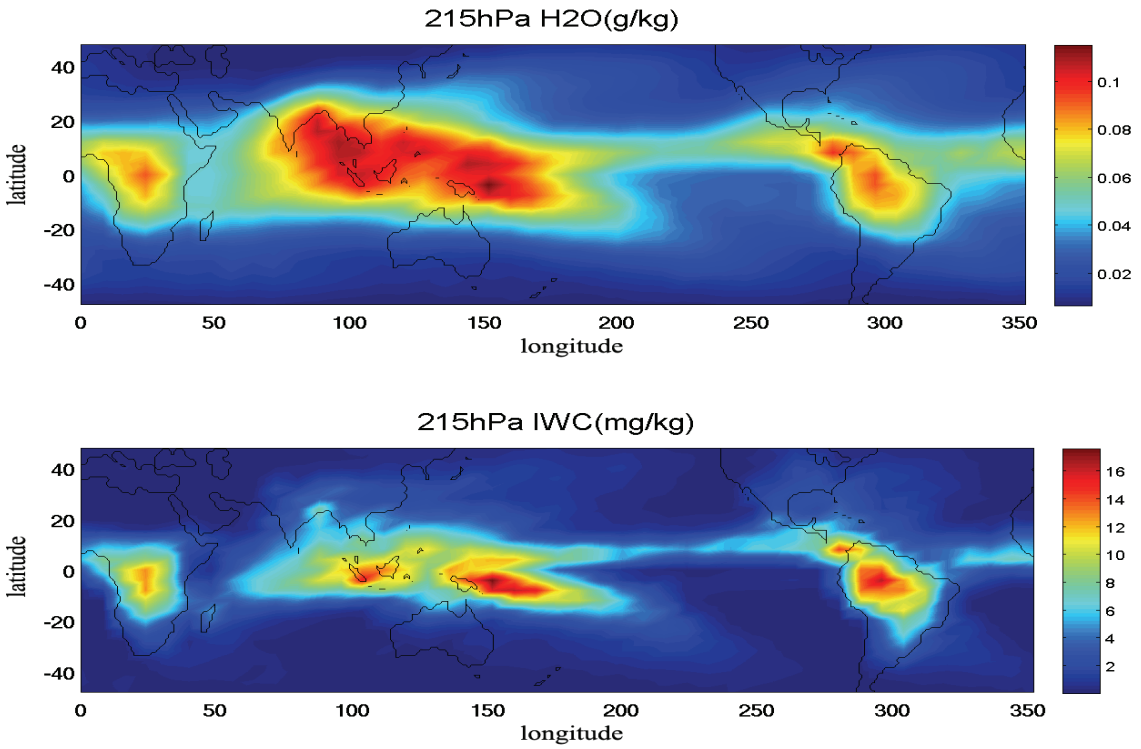

Figure 1.3. The climatological mean (Sep 2004 – Aug 2010) distribution of MLS specific humidity and ice water content at 215 hPa.

While AIRS and MLS are the two major satellite observations analyzed in this thesis, other satellite products are also occasionally used. Specifically, the IWP retrieved from MODIS (Moderate Resolution Imaging Spectroradiometer) is used in conjunction with MLS IWC products in our estimation of high-cloud feedback. The precipitation rate derived from TRMM (Tropical Rainfall Measuring Mission) observation is used in our investigation of the atmospheric bridge mechanism. The details of MODIS retrievals of IWP can be found in *King et al*. [2003] and the TRMM precipitation retrievals were documented by *Huffman et al.* [2007].

1.3.2 Reanalysis datasets

Making use of data assimilation techniques originally developed for weather forecast, reanalysis projects ingest large amounts of observations from various sources into a

numerical model of the atmosphere to seek an optimal compromise between observations and modelings. As a result, it can provide self-consistent and comprehensive data sets for multiple decades. Because of the meteorological origin of data assimilation techniques, the optimization is designed for matching the observations and model simulations at forecast time steps instead of over long-term average (i.e. climate mean states). Moreover, changes of observational systems assimilated into the reanalysis can produce artificial spurious trends and make the long-term time series of reanalysis record unrealistic. Such issues have been identified for the first-generation reanalysis projects such as NCEP-NCAR reanalysis and ECWMF ERA-40 reanalysis. For example, an opposite trend in column water vapor was found between these two reanalyses [*Trenberth et al*., 2005]. Figure 1.4 shows the UTH difference between two generations of ECMWF reanalyses (ERA-40 and a recently available reanalysis, ERA-interim) that was noticed in *Chuang et al*. [2010].

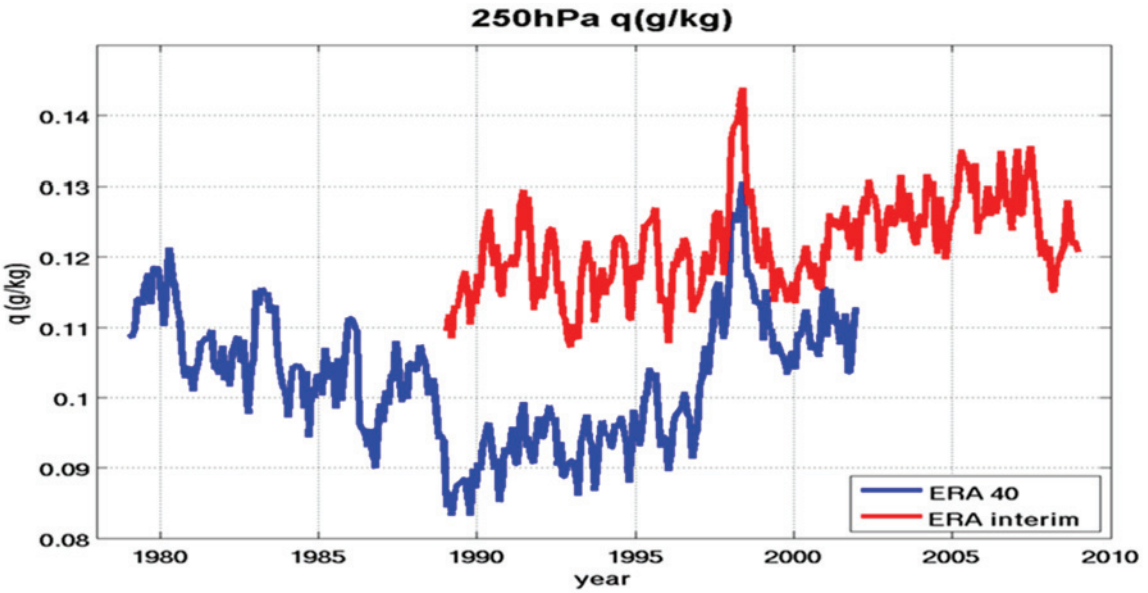

Figure 1.4. The time series of tropical mean (30°S-30°N) specific humidity at 250 hPa from ERA-40 and ERA-interim.

The latest reanalysis projects have invested a significant amount of effort to address the change of observational systems and introduced different correction methods [*Uppala et al*., 2005; *Simmons et al*., 2006; *Uppala et al.*, 2008; *Saha et al*., 2010]. As a result, significant improvements can be seen from the new reanalyses. For example, Figure 1.5a (adopted from Figure 2 in *Huang et al.*, [2005]) displays the fractional change of specific humidity anomalies with respect to temperature anomalies ($\frac{1}{\bar{q}}\frac{dq_a}{dT_a}$, subscript "a" denotes the anomalies) from two reanalyses (NCEP-1 and ECMWF ERA-40), and one GCM. Above 400 hPa, the two reanalyses are on the different sides of the constant relative humidity (RH) profile, indicating opposite changes of RH with respect to the temperature

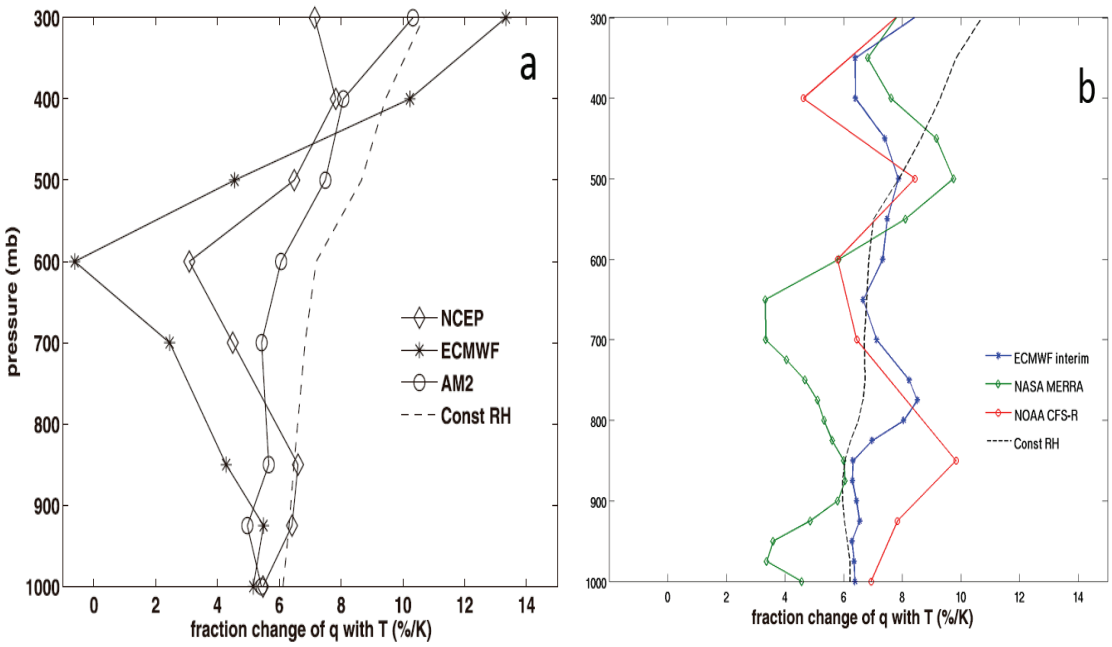

Figure 1.5. (a) Adopted from Figure 2 in *Huang et al*. [2005]. The fractional change of interannual anomalies of tropical mean specific humidity with temperature anomalies at the same pressure levels, i.e. $\frac{1}{\bar{q}}\frac{dq_a}{dT_a}$, where $\bar{q}$ denotes climatology mean and subscript "a" denotes interannual anomalies. The dash line is the result from assuming constant relative humidity at all pressure levels. NCEP-1 and ECMWF ERA-40 reanalyses are included here, so are the results from the NOAA GFDL AM2 simulation. (b) Same as (a) except for three recently available reanalyses, ECMWF interim, NASA MERRA, and NOAA CFS-R.

anomaly in these two reanalyses. *Huang et al.*, [2005] suggested this difference is largely due to the assimilation of humidity by the two reanalyses: ERA-40 directly assimilated humidity from HIRS radiance, while NCEP relied on radiosonde for humidity. An updated plot using three recent release reanalyses is shown in Figure 1.5b. The three reanalyses are ERA-interim from ECMWF [*Simmons et al*., 2006; *Uppala et al.*, 2008]; Modern Era Retrospective-Analysis for Research and Application (MERRA) from NASA [*Rienecker et al.,* 2011] and Climate Forecast System Reanalysis (CFSR) from NCEP (National Centers for Environmental Prediction) [*Saha et al*., 2010]. Above 400 hPa, the three reanalyses now show much more consistent results.

These advances in reanalyses give us more confidence of using them in the study of the interannual variations. They provide us not only globally comprehensive and continuous datasets but also the dynamic variables (e.g. vertical velocity), which are not directly measurable from observations. With the information from reanalyses, we are able to analyze the dynamics of the climate system, for example, using them to study the relation between the IWC and the large-scale circulation. Figure 1.6 shows the distribution of 225hPa IWC from Aura MLS observations and 500hPa vertical velocity (ω) from ERA-interim reanalysis. The pattern of 225hPa IWC is similar to that of 500hPa vertical velocity, since both of them are tightly related to the tropical deep convection.

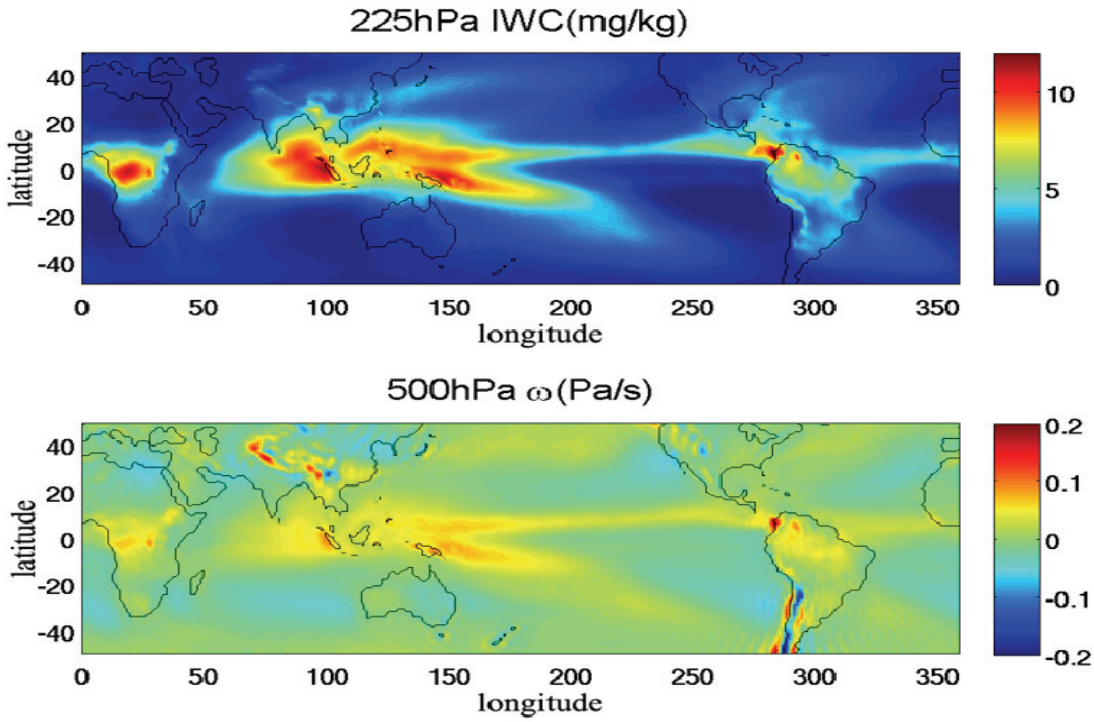

Figure 1.6. The mean 225hPa ice water content and 500hPa vertical velocity (ω) of ERA-interim reanalysis from Jan 1989 to Nov 2010. Note the negative ω is upward motion.

1.2.3 GCM simulations

GCMs are designed to simulate the climate system with the practical goal of projecting future climate changes. They are used to study the dynamics of the climate system and to understand the complex interactions between the atmosphere, ocean, land and cryosphere. Previously, it was hard to seek common features represented by different GCMs because few GCMs made their simulations available for community-wide analysis and scrutiny. Individual results from one GCM can be informative enough to understand the mechanism behind that particular GCM but may not be repeatable in other GCMs. The parameterizations of each GCM are different in many aspects. If there is a common feature across all the GCM outputs, we have more confidence in the robustness of this feature. As an example, *Held and Soden* [2006] studied hydrological changes in a warmer

climate across 20 GCMs, pointing out the consistent behavior of "warm gets warmer and dry gets drier" and then using a thermodynamic scaling argument to explain such behavior across all GCMs. It was also shown that the mean behavior of GCMs agrees better with observations than does an individual GCM [*Gleckler et al.,* 2008]. It then becomes a trend to seek the common behavior across all major GCMs (e.g. calculating the ensemble mean of all GCMs, instead of using individual GCM) as a robust simulation result. Therefore, it is desirable to have outputs from major GCMs under experiments stipulated specifically for coherent comparisons.

Since 2004, an unprecedented collection of model outputs from leading modeling centers around the world has been made available for the scientific community. DOE's (Department of Energy) PCMDI (Program for Climate Model Diagnosis and Intercomparison) collects a large amount of data from ~20 different GCMs that simulate the present climate, the historical climate of the 20th century and the future climates in the 21st/22nd centuries under several scenarios. These data constituted phase 3 of the Coupled-Model Intercomparison Project (CMIP3). CMIP3 is the first comprehensive dataset for intercomparisons of various variables among GCMs under the same predefined numerical experiment protocols. Research using this dataset crucially contributed to the Fourth Assessment Report (AR4) of the IPCC. In 2008, over 20 climate modeling groups agreed to construct a new series of climate model experiments which now compose CMIP5 (the fifth phase of CMIP). The recently released CMIP5 is expected to be used in preparation for the Fifth Assessment Report (AR5). Part of CMIP5 data was already available for analysis and used in this thesis.

Overall, we have more advanced datasets from observations, reanalyses and GCMs to examine the interannual variability and the dependence of tropical UTH and high clouds on large-scale dynamic and thermodynamic parameters. These motivated us to visit the research questions mentioned in Section 1.2.

1.4 Motivations and research objectives

The theme of this thesis is to study the tropical UTH and high clouds, especially their relationships and interactions with the large-scale thermodynamic and dynamic environment at the interannual time scale as well as their change in the future climate. Using multiple years of high-quality satellite observations that have not been available until recently, the reanalyses from NCEP and ECMWF, the large amount of simulation outputs archived for the CMIP phase-3 and phase-5 projects, in addition to the conceptual model of tropical climate in a framework of radiative-convective equilibrium, this thesis strives to address the following questions:

1. What is the relation between the interannual variations of tropical UTH and those of tropical SST over the convective region? Why is tropical UTH closely correlated with tropical mean SST, even with those SST over subsidence regions?
2. What mechanisms regulate the interannual variations of UTH and high clouds in each tropical ocean basin? How will these mechanisms change in the future climate, as simulated by different GCMs?
3. How can the interannual variations of total amount of ice water presented in the tropical upper troposphere be understood? Based on observations

and models, can we provide a constraint for the change of ice water amount in the future climate?

4. Are there connections between the weakening of Walker circulation and the change of clear-sky radiative cooling in the future climate?

The chapters of this thesis are organized as follows: Chapter 2 investigates the relation between the interannual variability of tropical UTH and SST only in convection regions. Chapter 3 explores the connections among interannual variations of tropical UTH and ice clouds and also the dynamic and thermodynamic fields over four tropical ocean basins. Chapter 4 analyzes the relation between the interannual anomaly of ice clouds and that of large-scale vertical velocity and explores connections to the future ice cloud feedback. Chapter 5 explores the contribution of clear-sky radiative cooling to the weakening of tropical circulation in response to global warming from a simplified radiative-convective equilibrium point of view. Finally, a summary of these findings and thoughts on future work are presented in Chapter 6.

Chapter 2

Interannual variations of tropical upper tropospheric humidity and tropical rainy-region SST: comparisons between models, reanalyses, and observations

The material in this chapter was published in

Chuang, H., X. Huang, and K. Minschwaner (2010), Interannual variations of tropical upper tropospheric humidity and tropical rainy-region SST: Comparisons between models, reanalyses, and observations, *J. Geophys. Res*., 115, D21125, doi:10.1029/2010JD014205.

2.1 Introduction

Owing to its roles in radiation, dynamics, cloud microphysics, and the complex interactions between these processes, water vapor lies at the heart of projecting future climate change. Water vapor feedback is the most important positive feedback to amplify the surface warming caused by increases of greenhouse gases in the atmosphere [*Held*

and Soden, 2000; *Bony et al.*, 2006; *Soden and Held*, 2006]. Particularly, owing to its important role in regulating the radiation budget and close connection to tropical deep convection, the tropical upper tropospheric humidity (UTH) has been a focus in climate research since the 1990s [*Lindzen*, 1990; *Soden and Bretherton*, 1994; *Soden and Fu*, 1995; *Sherwood*, 1996a; *Pierrehumbert and Roca*, 1998; *Dessler and Sherwood*, 2000; *Sherwood and Dessler*, 2003; *Soden et al.*, 2005; *Sherwood et al.*, 2006; *Su et al.*, 2006; *John and Soden*, 2006; *Dessler et al.*, 2008; *Sherwood et al.*, 2010]. The major source of tropical UTH is tropical deep convection [*Houze and Betts*, 1981; *Held and Soden*, 2000] while its large-scale distribution is influenced by moisture advection and diffusion, as well as condensation [*Betts and Albrecht*, 1987; *Sun and Lindzen*, 1993; *Udelhofen and Hartmann*, 1995; *Sherwood*, 1996a; *Pierrehumbert*, 1998; *Pierrehumbert and Roca*, 1998; *Dessler and Sherwood*, 2000]. Tropical deep convection transports moisture upward and injects it to the upper troposphere. The deep convection also plays an indispensable role in maintaining a nearly moist-adiabatic profile for the entire tropical troposphere [*Stone and Carlson*, 1979; *Xu and Emanuel*, 1989; *Wallace*, 1992]. From this point of view, deep convection is the venue from which the upper troposphere can directly "communicate" with the surface. For the same reason, the surface temperature over non-convective regions has no such direct connection with upper tropospheric temperature, nor with the UTH. Therefore, the tropical mean UTH variations could be expected to correlate more closely with the variations of surface temperature in deep-convection regions rather than those in large-scale subsidence (non-convective) regions.

Many previous studies [*Sun and Held*, 1996; *Sun et al.*, 2001] about the tropical UTH and upper-tropospheric temperature employed the tropical-mean SST variations

instead of the SST variations over deep-convection regions. *Sobel et al*. [2002] explained, from a statistical point of view, the coincidence of obtaining similar interannual variations from different ways of sampling the tropical SST. In the same study it has been argued that, for large ENSO events, the variations of tropical-mean SST and SST over the deep-convection regions could be significantly different. There also have been studies which used different convective indices such as SST threshold, OLR (outgoing longwave radiation), precipitation, and high-cloud fraction to filter SST and analyzed relations between such filtered SST and upper tropospheric properties. For example, *Minschwaner and Dessler* [2004] (hereafter *MD*04) used monthly mean OLR less than 250 Wm^{-2} as a filter to obtain monthly mean SST over the deep-convection region and then studied its interannual variation with UTH anomalies observed from UARS MLS (Upper Atmosphere Research Satellite, Microwave Limb Sounder). Convective-region SST has also been approximated in some studies [*Lindzen et al.*, 2001; *Hartmann and Michelsen*, 2002; *Su et al.*, 2008a] by weighting SST by cloud fraction. *Kubota and Terao* [2004] on the other hand, used daily precipitation rate (> 6mm day^{-1}) as a convective index to compile SST only over such strong precipitating regions (hereafter, rainy-region SST) and then examined decadal variability of such rainy-region SST.

Relationships between tropical mean water vapor and temperature over the interannual timescale were first studied by *Sun and Held* [1996]. They found large discrepancies between the GFDL GCM and radiosonde observations: modeled correlations being much larger than observed. When the same analysis was performed to GCM output archived for Atmospheric Model Intercomprison Project (AMIP) [*Sun et al.*, 2001], the discrepancies were essentially same even though the models were significantly

different from each other in many aspects. *Huang et al.*, [2005] showed inconsistent interannual co-variability of tropical temperature and humidity between two reanalyses (ECMWF ERA-40 and NCEP reanalyses), the GFDL AM2 model, and HIRS observations from NOAA satellite. A discrepancy in the water vapor field in ERA-40 and NCEP reanalysis was also found by *Chen et al.* [2008a]. In other words, such model-observation discrepancies remain unchanged in fifteen years, although both models and observations themselves have been improved substantially.

In this chapter, we examine correlations between interannual anomalies of tropical UTH and rainy-region SST (as an index of convection-region SST) in the observations, reanalyses, and GCM simulations. Given the fact that the area covered by the deep convection could vary significantly at intraseasonal and even shorter timescales (e.g. due to monsoon onset or tropical intraseasonal oscillation), it would be meaningful to construct rainy-region SST based on precipitation data at daily or pentad timescales, instead of monthly timescales. Then interannual rainy-region SST anomalies can be obtained from compilations of such daily- or pentad-resolution rainy-region SST. Such anomalies then can be correlated with the tropical UTH anomalies. The chapter uses newly available reanalysis (ECMWF ERA-interim), satellite observations (AIRS humidity profiles), and IPCC AR4 GCM simulations to revisit the discrepancies mentioned in the previous paragraph, with a focus on the influence of rainy-region SST on the UTH anomalies. An idealized equilibrium model that has convection as the sole source of tropical UTH will also be used to further understand such control of UTH variation by the deep convection as seen from the reanalyses and GCM simulations.

The sections of this paper are organized as follows. Datasets and methodology are presented in Section 2.2. Section 2.3 describes the results from analyzing reanalyses, observations, and GCM simulations. Section 2.4 discusses the tropical UTH profiles computed from the idealized equilibrium model and comparisons with those produced from reanalyses and GCM simulations. Conclusion and discussion are given in Section 2.5.

2.2 Data and Method

2.2.1 Datasets and definition of rainy-region SST

Monthly-mean specific humidity from Atmospheric Infrared Sounder (AIRS) [*Fetzer et al.*, 2006] and from two ECMWF reanalysis products, ERA-40 [*Uppala et al.*, 2005] and ERA-interim [*Simmons et al.*, 2006; *Uppala et al.*, 2008], are analyzed in this study. Compared to the ERA-40, noteworthy advances in ERA-interim data assimilation system are (1) 12-hour 4D-var instead of 6-hour 3D-var; (2) higher horizontal resolution (T255 vs. T159, i.e. ~75 km vs. 125 km); (3) a new humidity analysis algorithm and improved model physics; (4) variational bias correction of satellite radiance data instead of the static bias correction in ERA-40, as well as other improvements in bias handling. More detailed improvements and impacts on data assimilation can be found in *Uppala et al.* [2008]. As a result, its assimilated UTH properties are noticeably different than from the ERA-40 model, which shall be seen in Section 2.3. Observational precipitation data are taken from the pentad-resolution GPCP (Global Precipitation Climatology Project) data [*Huffman et al.*, 2001; *Adler et al.*, 2003; *Xie et al.*, 2003]. Pentad-resolution rainy-region SST is then obtained as follows: first the monthly NOAA Optimum Interpolation (OI) SSTs [*Reynolds and Marsico*, 1993; *Reynolds et al.*, 2002] are temporally

interpolated to the mid-point of each five-day period used in the GPCP data, then rainy-region SST is defined as SST over regions with GPCP precipitation higher than 6 mm/day. Such a threshold, which encompasses the 16.54% high end of probability distribution function (PDF) of GPCP precipitation in the tropics, has been used in previous studies as well [*Sobel et al.*, 2002; *Kubota and Terao*, 2004]. The overall results are not sensitive to the moderate change of the choice of such 6mm/day rain threshold. Other relevant details of observational and reanalysis data are summarized in Table 2.1.

Data Sources	**Variables**	**Horizontal resolution**	**Time period analyzed here**	**Focused area**
AIRS L3 monthly means	Specific humidity	1°×1°	2003.01-2008.12	30°S-30°N
NOAA OI v2 SST	SST	1°×1°	1982.01-2008.12	15°S-15°N
GPCP v1.0	Precipitation	2.5°×2.5°	1982.01-2008.12	15°S-15°N
ECMWF ERA-40	Specific humidity	2.5°×2.5°	1982.01-2001.12	30°S-30°N
ECMWF ERA-interim	Specific humidity and SST	1.5°×1.5°	1989.01-2008.12	30°S-30°N

Table 2.1. Summary of observational and reanalysis data used in this study.

Figure 2.1(a) shows the time series of fractional area defined as rainy region in this way over the entire tropics (30°N-30°S) and over the inner tropics (15°S-15°N), respectively. The rainy region occupies 14.91% of the entire tropics and 20.37% of the inner tropics on average.

For comparison, monthly-mean UTH and SST as well as daily precipitation from the 20th-century run (20C3m) of four IPCC-AR4 coupled GCMs (GFDL-CM2.0, ECHAM5,

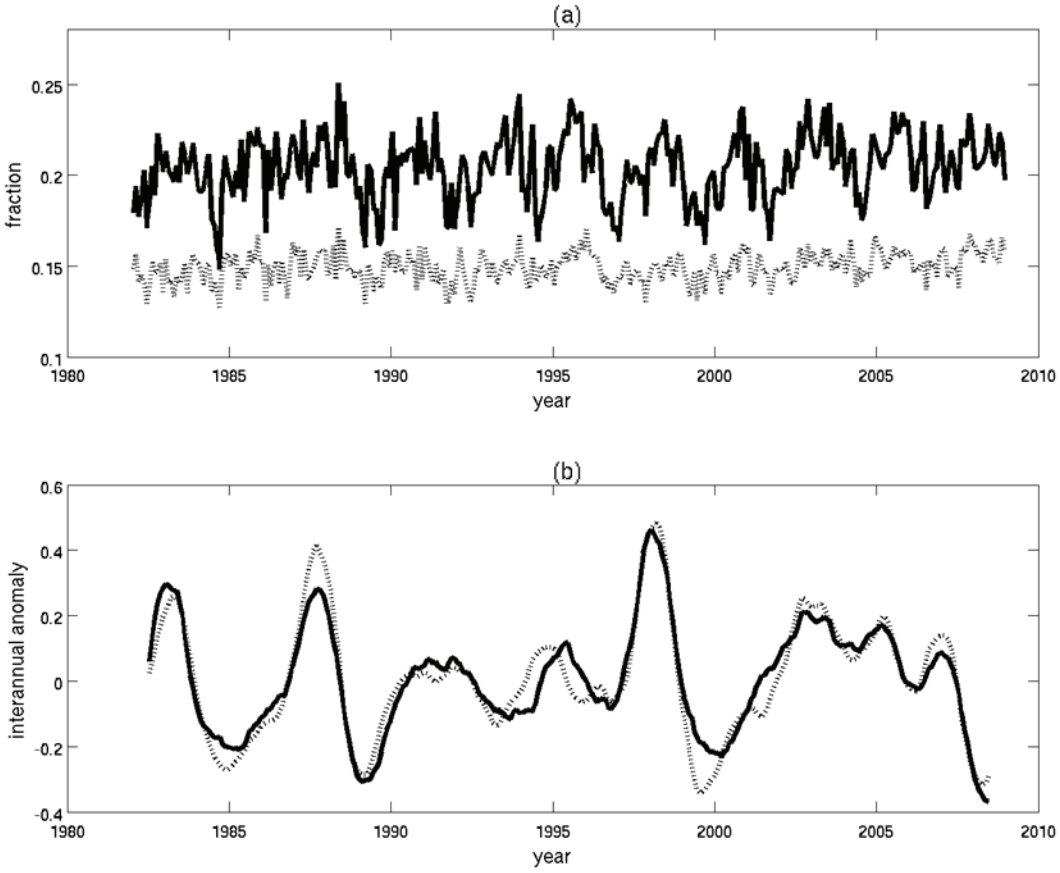

Figure 2.1. Dotted gray curve is the time series of the percentage of tropical area (30°S-30°N) with GPCP pentad-resolution precipitation larger than 6mm/day. Solid curve is same except for the inner tropics (15°S-15°N). (b) Dotted line is the interannual anomalies of observed NOAA SST averaged over the entire inner tropics. Solid line is the interannual anomalies of observed rainy-region SST in the inner tropics. Definition of the rainy-region SST and method to compute the interannual anomaly can be found in Section 2.2 of the context.

MRI-CGCM2.3.2, and NCAR-CCSM3) are analyzed. The relevant details of the four GCMs are listed in Table 2.2. The four GCMs used here have different native vertical resolutions even though the archives at PCMDI were provided at the IPCC AR4 mandatory levels. The number of layers in the upper troposphere (e.g. 100-400 hPa) varies from five to ten, providing enough vertical levels for interpolating onto the IPCC AR4 levels. *Ingram* [2002] showed that the UT water vapor variation and feedback are not sensitive to the vertical resolution of such GCMs or even higher ones.

Given that the large-scale SST varies smoothly with time, that no daily SST

GCMs	**Horizontal resolution**	**Time period**	**Convection scheme**	**Dynamic Core**
NCAR-CCSM3	T85 (~1.4°)	1980.01-1999.12	*Zhang and McFarlane* [1995]	Spectral
GFDL-CM2.0	2.0°×2.5°	1980.01-1999.12	Relaxed Arakawa-Schubert [*Moorthi and Suarez*, 1992]	Finite difference (Horizontal) and finite volume (vertical)
ECHAM5 (Germany)	T63 (~1.875°)	1980.01-1999.12	*Tiedtke* [1989] and *Nordeng* [1994]	Spectral
MRI-CGCM2.3.2 (Japan)	T42 (~2.8°)	1980.01-1999.12	Prognostic Arakawa-Schubert [*Randall and Pan,* 1993]	Spectral

Table 2.2. Summary of the four GCM simulations (the 20th century run) used in this study, all archived for IPCC-AR4 GCM 20th and available from the PCMDI, Lawrence-Livermore National Laboratory.

observations over the entire tropics are available for the period of 1980-1999, and that GCM simulations usually are done with SST interpolated from monthly mean SST, we adopt here the same approach and linearly interpolate monthly SST to daily resolution. Precipitation simulated by a GCM could be significantly different from observed in both the magnitude and in the PDF. Therefore, for each GCM, we first compute the PDF of simulated daily precipitation over the entire tropics then define the rainy regions on any given day as being regions with daily precipitation falling into the 16.54% high end of the PDF, the same PDF criterion used in the observational analysis.

2.2.2 Data analysis

In this study, we focus on the interannual variation of UTH profiles over the entire tropics and its relation to the interannual variation of rainy-region SST in the inner tropics. Monthly-mean rainy-region SST is obtained from pentad (for observations and reanalyses) or daily (for GCM simulations) rainy-region SST interpolated from monthly mean SST as we describe in the previous paragraph. Then interannual anomalies are computed from the monthly-mean rainy-region SST and UTH profiles in the same way as in *Huang et al.* [2005]: a linear trend is first removed by regression, next the mean seasonal cycle is computed and subtracted from the data, and finally a 13-month moving average is applied to the data to obtain the interannual anomalies (for brevity, hereafter interannual anomalies and anomalies are used interchangeably). The interannual anomalies of SST and rainy-region SST obtained in this way are shown in Figure 2.1b. As shown in previous studies such as *Sobel et al.* [2002], the two anomalies resemble each other to a large extent although the rainy-region SST anomalies generally have smaller amplitude than the tropical mean SST anomalies.

The statistical significances of correlations between the two time series of interannual anomalies are assessed with a monte-carlo isospectrum method [*Camp et al.*, 2003]. The method first generates 100,000 surrogate time series with power spectra identical to one of the two time series but randomized phases, and then the correlation with the other time series is computed for each surrogate time series. By doing so, a probability of obtaining a correlation coefficient as large as any specified value can be estimated in a double-sided test.

2.2.3 Idealized model

An idealized, single-column steady-state radiative-convective model is used here to further understand results from data analysis. A detailed description of the model can be found in *MD*04. The model describes the balance between adiabatic warming and clear-sky radiative cooling outside the cores of deep convection as well as the conservation of humidity through detrainment process, assuming negligible contribution from evaporation of condensates. Specifically, it calculates the downward air mass flux (M) by

$$M = \frac{Q_R}{C_p(\frac{dT}{dz} + \Gamma_d)} \tag{5.1}$$

where C_p is the heat capacity of dry air, T is the temperature, z is the altitude, Γ_d is the dry-adiabatic lapse rate, and Q_R is the clear-sky radiative cooling rate,

$$Q_R \cong Q_R(T, q) \tag{5.2}$$

where q is the specific humidity. In this study Q_R is computed from the stand-alone NCAR CCM3 radiation column model [*Kiehl et al.*, 1998] for any given (T, q) profiles.

The model further assumes that convection detrainment is the sole source of tropical UTH and evaporation of condensate during detrainment is negligible. Then the

vertical convergence of the upper-tropospheric downward mass flux should be compensated by the detrainment from the deep convection, i.e.

$$\frac{dM}{dz}[q - q^*(T)] = -M\frac{dq}{dz} \tag{5.3}$$

where q* is saturation specific humidity.

In this study we specify the temperature profile to be either the tropical-mean (30°N-30°S) profiles from a GCM simulation or that from a reanalysis product. The three equations described above are solved simultaneously by iteration to obtain steady-state solutions of M, q, and Q_R. Hereafter, we denote the humidity profiles obtained from this simple model as q_{DC}, where the subscript "DC" is used to emphasize that the only source of q in this model is deep convection.

2.3 Data analysis results

The correlation coefficients between the interannual anomalies of tropical-mean UTH profiles (from 400 hPa to 150 hPa) and that of rainy-region SST are shown in Figure 2.2. For comparison, the correlations with SST interannual anomalies averaged over the entire inner tropics are shown in the same plot. For ERA-40 reanalysis, when mean SST is used, only correlations at 200 hPa and 150 hPa are statistically significant. When rainy-region SST is used, the correlation is noticeably improved from ~0.4 to ~0.5 and such correlation is statistically significant from 400 hPa to 150 hPa. For AIRS, the correlation coefficients between mean SST and UTH anomalies are ~0.80-0.90, much higher than those of ERA-40. When rainy-region SST is used instead of mean SST, the correlation is slightly improved by ~2.0% for 200-400 hPa but reduced by 4.75% at 150 hPa. Note such slight increase or decrease of correlation is within the uncertainty due to the short time period of AIRS data (please see the next paragraph for an estimate for such

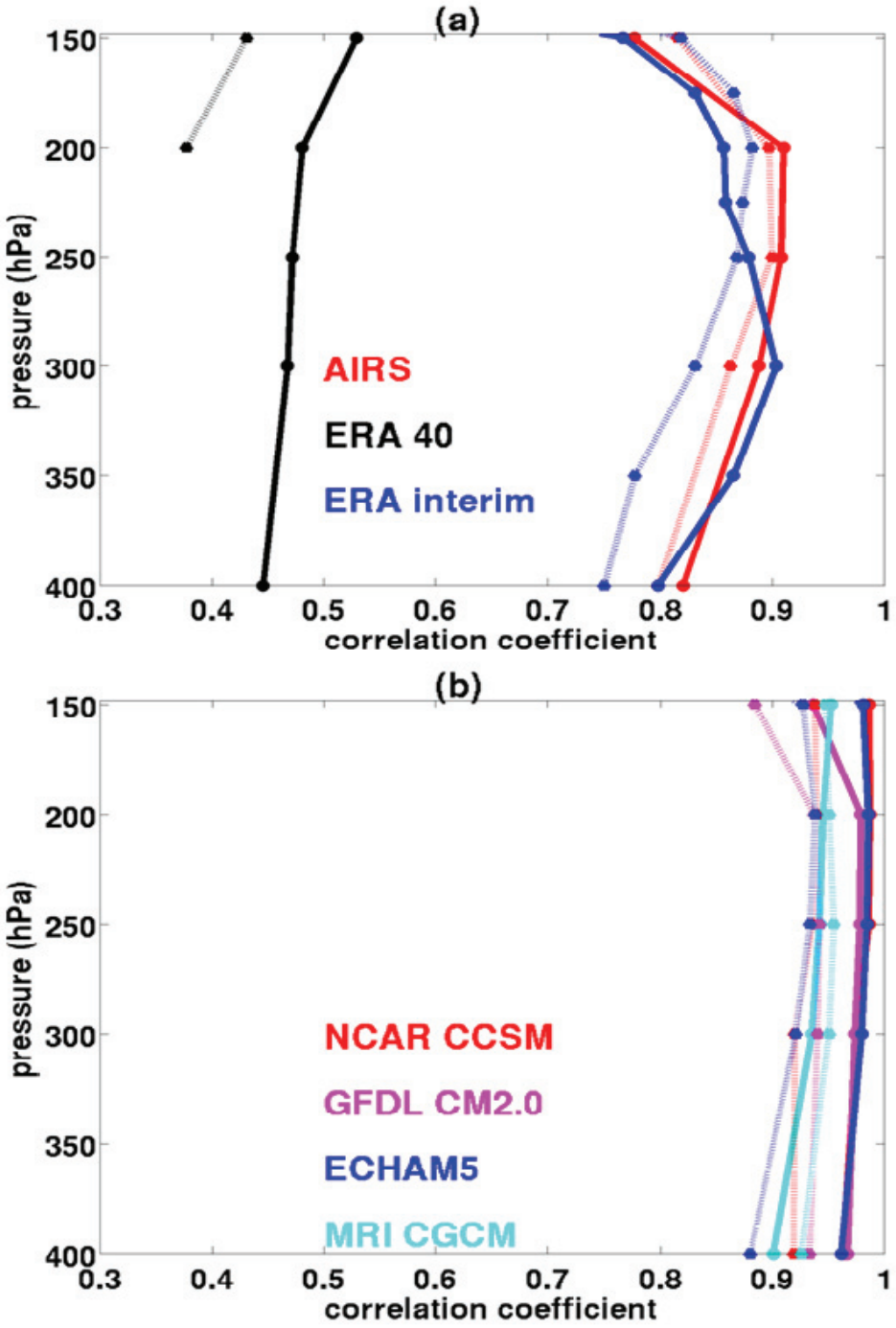

Figure 2.2. (a) Solid (dash) lines are correlation coefficients between interannual anomalies of tropical mean specific humidity and those of inner-tropical (15°S-15°N) rainy-region SST (inner-tropical mean SST). Only statistically significant correlations are plotted. Results from AIRS data are in red, ERA-40 in black, and ERA-interim in blue. (b) Same as (a) except for four GCM results.

uncertainty) and AIRS humidity retrieval is less confident at levels above 200 hPa [*Fetzer et al.*, 2006].

For the ERA-interim reanalysis, its correlation coefficients are close to those of AIRS (a cautionary note here is that the degrees of freedom of 6-year AIRS data are significantly different from those of 20-year ERA-interim data). When rainy-region SST is used, slight to moderate improvements can be seen for 400-250 hPa, largest of which is 11.3% at 350 hPa. Similar to the case of AIRS, the correlation is reduced slightly above 250 hPa.

It has been noted before that the interannual anomalies of ERA-40 UTH are different from those of NCEP reanalysis and satellite measurements [*Huang et al.*, 2005]. The discrepancies between ERA-40 and ERA-interim are most likely due to the changes implemented in ERA-interim that are related to moist physics and elimination of volcano contamination in the satellite radiances assimilated into the reanalysis. The correlations of AIRS data are derived from six years of data, in contrast to the twenty years of data used in ERA-40 and ERA-interim. To assess the influence of such limited period on the derived correlations, we calculated the correlations for six consecutive years of ERA-interim data and compared such correlations with those derived from the 20 years of ERA-interim data. For four segments of such 6-year data segment that we examined, all yield correlations clustering around the correlations computed from the 20-year data, with difference less than ~±10% between 400-150 hPa.

All four GCMs examined here exhibit consistently higher correlation between UTH and SST anomalies than shown by the AIRS data and reanalyses products over all levels from 400 hPa to 150 hPa. The correlations between the mean SST and UTH anomalies

are as high as ~0.88-0.95. When rainy-region SST is used, the correlation is even higher for three GCMs with improvements of up to ~5%.

To illustrate the contrast between model and observation in a more explicit way, Figure 2.3a shows scatter plots of ERA-interim humidity anomalies at 300 hPa versus SST (or rainy-region SST) anomalies and Figure 2.3b show the counterpart from the GFDL model output. For SST anomalies less than 0.2 K, the spread of mean SST is only slightly wider than that of rainy-region SST. But for large positive anomalies (>0.2 K), the spread of mean SST is substantially wider than that of rainy-region SST. This is consistent with what Sobel et al. [2002] described about the deviation between SST and rainy-region SST anomalies when the SST anomalies become large during an El Nino phase. It is such differences over the large positive SST anomalies that lead to the improved correlations shown in Figure 2.2a. In contrast, the GFDL CM2 (Figure 2.3b) does not exhibit such distinctive changes in terms of the spread of scatter plots when SST anomalies are large and positive. This behavior is consistent among all GCMs studied (not shown here), thus the difference between scatter plot of SST anomalies and that of rainy-region SST anomalies are insignificant over the entire range. Figure 2.4 shows the corresponding UTH anomalies (q_a) regressed onto the SST anomalies (SST_a) to obtain a fractional change of UTH with respect to SST anomalies, i.e. $(\frac{1}{\bar{q}}\frac{dq_a}{dSST_a})$ where $\bar{q}$ is the mean humidity. For both AIRS and the two reanalyses (Figure 2.4a), the fractional changes at all levels are larger when rainy-region SST is used instead of mean SST. For ERA-interim, the 95% confidence levels of fractional changes do not overlap each other from 400 hPa to 200 hPa, indicating that the improvement is statistically significant. As for the GCM simulations (Figure 2.4b), the regression of fractional change is larger for

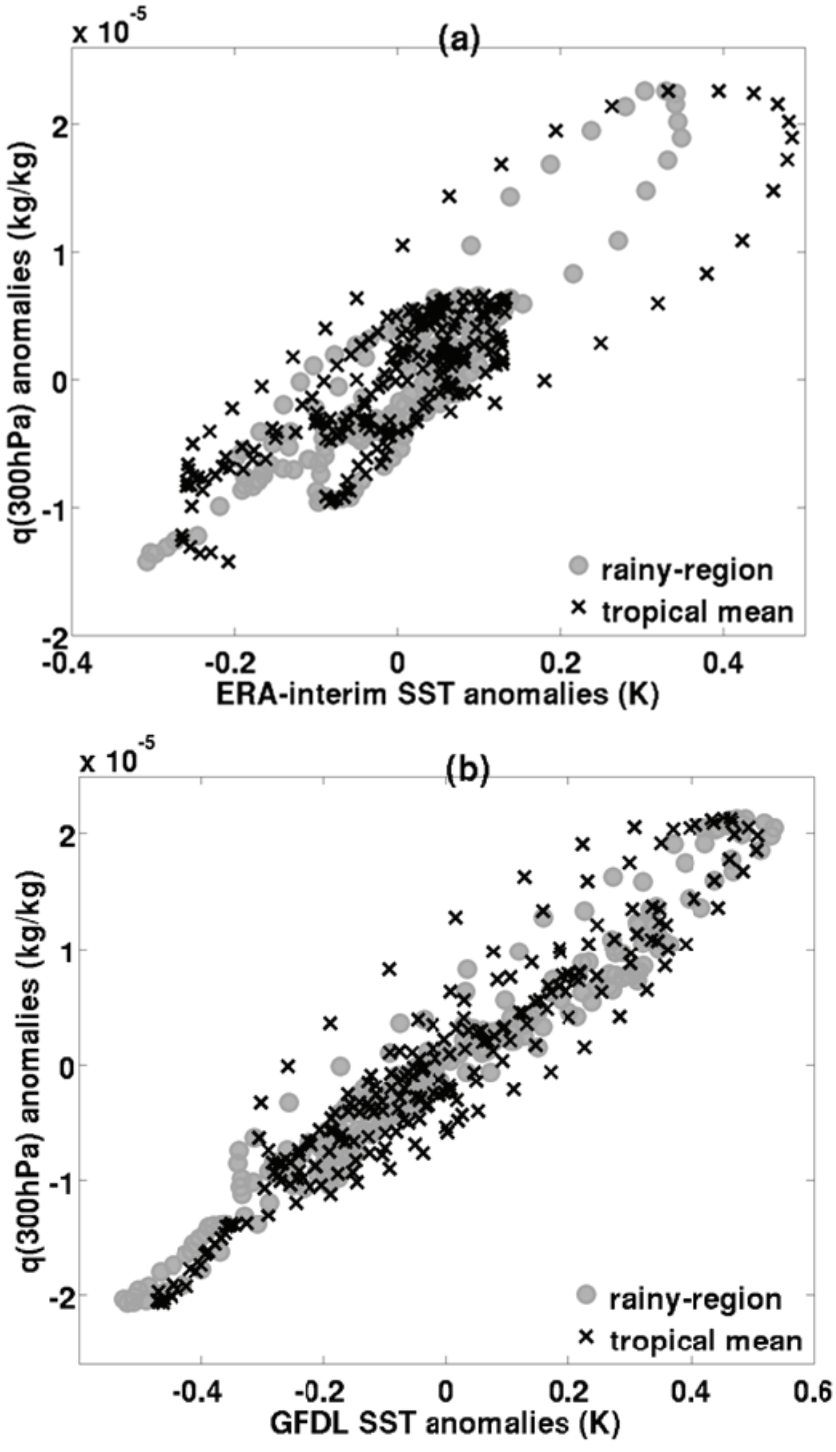

Figure 2.3. (a) Scatter plot of ERA-interim humidity anomalies at 300 mb versus SST anomalies. The black crosses denote the inner-tropical mean SST anomalies, and the gray circles denote the rainy-region SST anomalies. (b) Same as (a) except for the GFDL CM2.0 simulation.

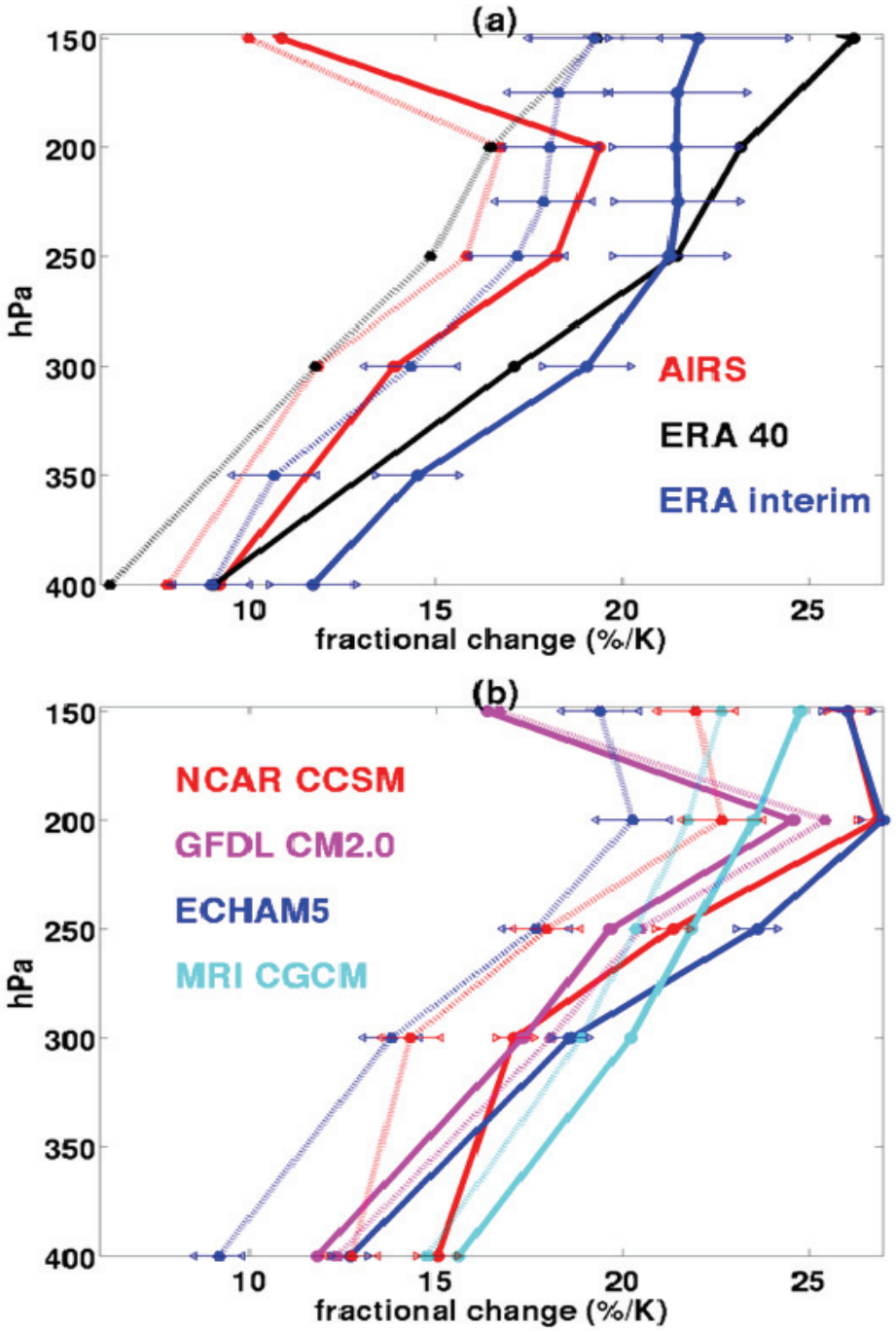

Figure 2.4. (a) Dotted (solid) lines are fractional change of specific humidity anomalies with respect to the inner-tropical-mean SST (rainy-region SST) anomalies. Only statistically significant results (i.e. p-value < 0.05) are plotted. AIRS results show in red, ERA-40 in black, and ERA-interim in blue. The horizontal thin blue lines represent the 95% confident intervals of the regressed fractional change of the ERA-interim data. (b) Same as (a) except for modeled fractional change. Different colors represent different GCMs as labeled on the plot. The 95% confident intervals for the ECHAM5 and NCAR CCSM models are plotted in horizontal thin lines.

all levels when rainy-region SST anomalies are used instead of mean SST anomalies for three GCMs. The improvements for NCAR CCSM and ECHAM5 are statistically significant at more than the 95% confidence level. GFDL model shows slightly decrease in regressed fractional change at all levels when rainy-regions SST is used, but all decreases here are statistically insignificant.

Referring to Figures 2.2a and 2.2b, the significant differences in modeled and observed correlation coefficients between UTH and mean SST anomalies were noted in *Sun and Held* [1996]. Such model-observation discrepancies in correlation are substantially reduced here when AIRS or ERA-interim are used. Although the ERA-interim and ERA-40 have large disagreements on the correlations (Figure 2.2a), the regressed fractional changes of UTH for the two reanalyses are in fact in much better agreement (Figure 2.4a). This indicates that the low correlations between ERA-40 UTH and SST (mean or rainy-region) might be a result of relatively "noisy" UTH interannual anomalies in the ERA-40. ERA-interim, on the other hand, has improved moist physics and more refined methods to assimilate multiple years of HIRS H_2O band radiances. These new features seemingly provide an improved capability for ERA-interim to represent the interannual anomalies of UTH.

When rainy-region SST anomalies are used instead of mean SST anomalies, both AIRS and ERA-interim show changes in the correlations between UTH anomalies and SST anomalies, but the sign of such changes is not the same through all vertical levels. For AIRS, there is no improvement in correlation between 200 and 150 hPa (Figure 2.2a); note that 200 hPa is also the level where the maximum fractional change in UTH anomaly is attained (Figure 2.4a). Below this level, the AIRS fractional change in UTH

anomalies is decreasing quickly from 19.4% to 9.2% at 400 hPa. For ERA-interim, the improvement of correlation stops at 250 hPa. Similar to the case of AIRS, 250 hPa is also the level below which the fractional change of ERA-interim UTH anomalies decreases quickly and above which the fractional change essentially levels off (Figure 2.4a). The results suggest that 200 hPa (250 hPa) could be the level at which moisture anomalies have been influenced most by year-to-year variations in deep convection as seen from AIRS (ERA-interim), presumably via corresponding variations of the level of maximum detrainment since it is near this level where deep convection injects most saturated air into the upper troposphere. Previous studies suggest that the mean maximum outflow level from tropical deep convection is around 200 hPa (~350 K in potential temperature) [*Folkins et al.*, 2000; *Folkins*, 2002; *Fueglistaler et al.*, 2009] with certain geographical variations. For example, *Thompson et al.* [1979] suggested that it is at about 13 km in the western Pacific and 11 km in the eastern Atlantic. Our findings here suggest that, if we are able to compile a probability distribution function (PDF) of maximum outflow level of tropical deep convection, the largest interannual variation of such PDF is likely concentrated around 200 hPa for AIRS but equally spread around 150-250 hPa for the ERA-interim reanalysis. All GCMs, except MRI CGCM, also show such a "turning point" at 200 hPa in terms of the fractional change of UTH anomalies with rainy-region SST anomalies.

2.4 Results from an idealized model

In this section we explore the relations between simulated and observed UTH anomalies and deep convection from the perspective of an idealized model described in Section 2.2. Figure 2.5 displays the tropical climatology of clear-sky net radiative cooling

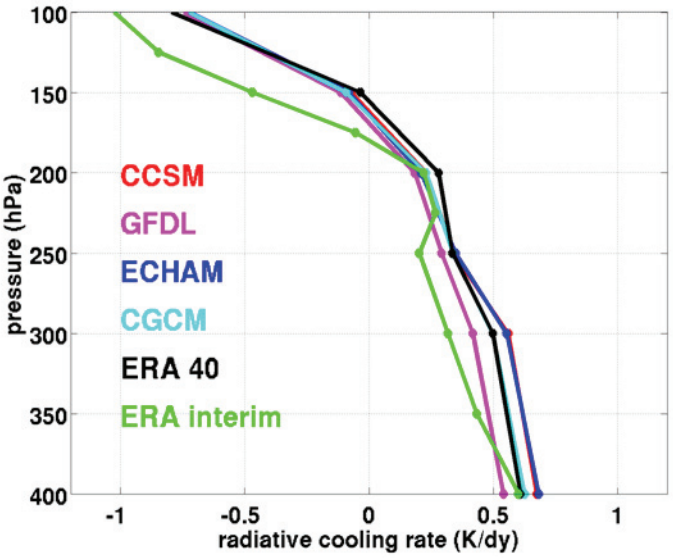

Figure 2.5. 20-year-averaged radiative cooling rate (K/day) profile in the upper troposphere. Different colors represent different datasets as labeled on the plot. Note that the radiative cooling rate is signed positive for cooling.

rates of four GCMs and two reanalysis datasets. The level of zero radiative cooling, for all cases, resides between 150 hPa and 200 hPa. This level is assumed to be the highest level of convective detrainment in the idealized model. As in *MD04*, the humidity profile (q_{DC}) is iteratively obtained from the Eqs. (5.1)-(5.3) for a detrainment layer about 100 hPa in thickness below the level of zero radiative cooling (i.e. 200-300 hPa in this study). Therefore, below we will focus solely on this layer.

Multiple-year means of the ratio of q_{DC} to the humidity in GCM simulations (or reanalysis) is shown in Figure 2.6a, accompanied by the yearly time series of such ratios at 250 hPa in Figure 2.6b. At the top part of the detrainment layer (~200 hPa), the ratio varies from 1.5 to 2.1 with a median value of 1.74. In the middle and lower levels (250-300 hPa), the ratios for all GCMs and ERA-interim are clustered around 1.0 with a median value of 0.99 for 250 hPa and 0.94 for 300 hPa. All GCMs and ERA-interim have small year-to-year variations. This corroborates that the contribution from deep-

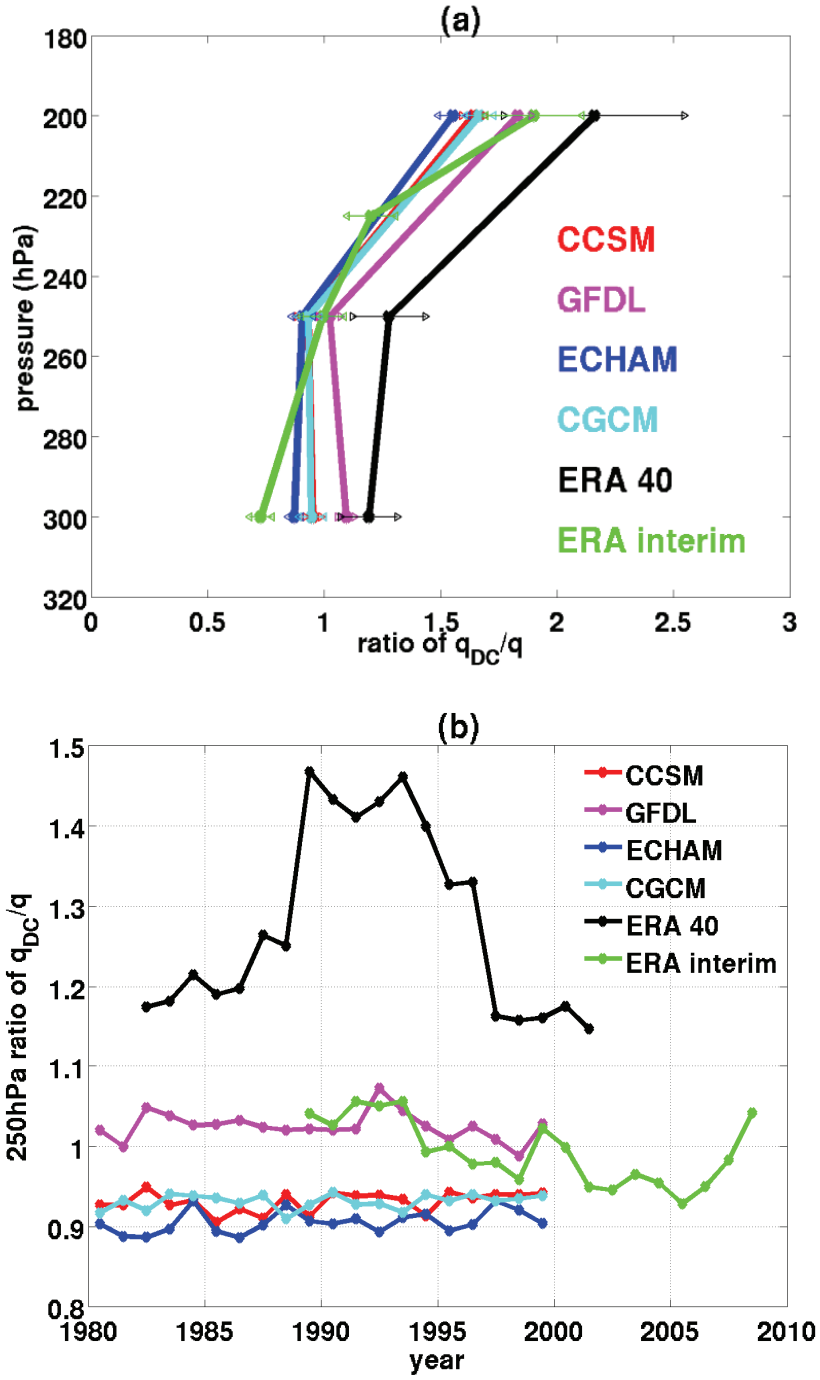

Figure 2.6. The ratio of 20-year mean q_{DC} to 20-year mean specific humidity from GCM simulations (or ERA reanalysis datasets). The horizontal lines present one standard deviation. (b) The time series of yearly mean ratio of q_{DC}/q at 250 mb. Different colors represent different datasets as labeled on the plot.

convective detrainment dominates the humidity variations at 250-300 hPa [*Folkins et al.*, 2002] in these GCMs and the ERA-interim reanalysis, but that other mechanisms (especially drying mechanisms) are not negligible at 200 hPa. The ERA-40 is an exception with a ratio of ~1.2 for 250 hPa and 300 hPa layers and 2.1 for 200 hPa, largest among all models and reanalyses examined here. When the annual-mean time series of such ratios are examined (Figure 2.6b), it becomes clear that ERA-40 has a distinctly elevated ratio ~1.4 between 1989 and 1994. Given the fact that ERA-40 assimilated HIRS 6.7 μm radiances directly and that the NOAA-11 HIRS radiance record is over the time frame from October 1988 to July 1994, this elevated ratio in ERA-40 might be related to how the HIRS on NOAA-11 has been assimilated, in addition to any possible contamination of Mt. Pinatubo eruption on the HIRS water vapor channels [*Uppala et al.*, 2004; *Uppala et al.*, 2005].

2.5 Conclusion and Discussion

The relations between tropical mean UTH anomalies and the inner tropical SST anomalies over the interannual timescale are studied here with two reanalysis datasets from ECMWF, AIRS retrievals, and GCM simulations. The mean correlation between interannual anomalies of UTH and rainy-region SST is 0.4615, 0.8611, and 0.8721 for the ECMWF ERA-40, ERA-interim, and AIRS dataset, respectively. For AIRS and ERA-interim, when rainy-region SST anomalies are used instead of mean SST anomalies, it introduces discernible increases in the correlation with UTH between 400 and 150 hPa (though the increase for the AIRS result is within the estimated uncertainty due to its short time period). All four GCMs examined here consistently show significantly higher correlation coefficients between UTH anomalies and mean SST (rainy-region SST)

anomalies (between 0.88 to 0.95). For AIRS observations and the two ECMWF reanalysis datasets, the fractional changes ($\frac{1}{\bar{q}}\frac{dq_a}{dSST_a}$) at all levels are larger when rain-region SST anomalies are used instead of the mean SST anomalies. As for the GCM simulations, three of the four GCMs studied show larger fractional changes when rainy-region SST anomalies are used. When GCM or reanalysis temperature fields are fed into an idealized model with deep convection being the only source of tropical UTH, the specific humidity at 200 hPa (near the top of the mean detrainment layer) calculated by this idealized model is almost twice as humid as it in the reanalysis and GCMs. This indicates that other drying effects (e.g. mixing, extra-tropical air intrusion, etc.) might be equally important for the humidity variations in this level. Between 250 and 300 hPa (the lower part of convective detrainment layer), the specific humidity from this idealized model agrees relatively well with those from GCM and reanalyses, suggesting a more dominant control of the deep convection over other processes. The detrainment layer of deep convection has a finite vertical thickness. One implication here is that the competition between deep convection and other mechanisms for regulating UTH might vary significantly within such vertical ranges of the detrainment layer.

Another finding of this study is the higher correlation between surface temperature and UTH anomalies in the ECMWF ERA-interim reanalysis compared to previous results from the ERA-40 reanalysis. A good agreement between the ERA-interim reanalysis and AIRS observations is also demonstrated. All reanalyses, based on algorithms originally designed for the variational analysis in numerical weather prediction, are aimed at achieving an optimal compromise between observation and modeling at each time step. To what extent such products can faithfully represent the climate aspect (e.g., annual-

mean, interannual anomalies, decadal trends) of certain fields less constrained by observations cannot be easily quantified. The improvements made to ERA-interim reanalysis, on both the model physics and the quality control of radiances to be assimilated into the reanalysis, seemingly contribute to the better agreements between ERA-interim and AIRS, at least for the tropical UTH interannual variability.

Because of the exponential dependence of saturation pressure on temperature, the saturation water vapor pressure could change by a factor of 10 or even more from the bottom part to the top part of the detrainment layer for tropical deep convection systems. Therefore, a reasonable representation of vertical detrainment profiles and its relation with large-scale circulation features, at least in a statistical sense, is vital to success in simulating the moistening of upper troposphere. If the moist convection scheme in a GCM puts water vapor at a wrong altitude in a wrong amount, it then gives following dynamic transport an incorrect starting point. Current GCMs tend to exhibit a prominent wet bias in the simulated UT specific humidity climatology when compared to observations. By comparing coupled-GCM simulations archived for the IPCC 4^{th} Assessment Report with tropical UTH retrieved from AIRS observations, *Pierce et al.* [2006] and *John and Soden* [2007] both showed large moist bias (25%-100% in the former and 100% and even more in the latter studies) in the free troposphere virtually for all GCMs that they had examined. These studies indicate that some common defects among these models should be responsible for such bias. Moreover, *John and Soden* [2007] showed that modeled planetary boundary layers (PBLs) also have a dry bias compared to the AIRS. By directly using spectrally-resolved radiances instead of retrieved UTH, *Huang et al.* [2006] reached the same conclusion about such contrast of

moist and dry biases between the free troposphere and the PBL in the GFDL GCM-AM2. *Huang et al.* [2006] also showed the dependence of such moist bias on the dynamic regimes: a stronger large-scale upward motion is associated with a larger moist bias. Both *John and Soden* [2007] and *Huang et al.* [2006] suggested that vertical transport of moisture to the UT (presumably by deep convection since it dominates the vertical transport) should be related to the moist bias in the mean climatology. The study here focuses on interannual variability and finds that the connections between tropical UTH and SST in tropical deep convection regions as seen in GCMs, reanalysis, and AIRS observations are different, which reaffirms the prerequisite need of improving the treatment of deep convection in order to correct any UTH moist bias in GCMs.

On the other hand, recent coordinated observations such as CloudSat and AIRS provide unprecedented opportunities to characterize the detrainment and outflow structures of convective systems over the entire tropics, as well as the associated moistening effect. Such multiple years of records from both instruments will be able to help us further understand discrepancies and issues discussed in this study.

The monthly-mean NOAA OI SST is used in this study primarily because of its long coverage since 1980s, which is desired for the analysis of ERA-40 and ERA-interim data. This SST dataset is based on both in-situ measurements and AVHRR SST retrieval [*Reynolds et al.*, 2002], latter of which is limited by the overcast clouds and heavy precipitation. Note the SST used in this study is large-scale SST (e.g. SST averaged over a 2°×2.5° grid box) and the subgrid variation of such SST is usually small. On the other hand, AVHRR has very high spatial resolution (~1.1km for IR imageries) and is capable of utilizing clear-sky gaps between cloud systems to obtain SST retrievals. A microwave-

based SST retrieval such as TMI SST is less subject to the issue of overcast clouds and heavy precipitation [*Bhat et al.,* 2004] and is capable of producing daily SST map. The TMI SST has been available only since December 1997 and is unsuitable for our study, but in the future when the data record becomes long enough, it will be a better candidate for this type of analysis.

This study focuses on the variation of tropical or inner-tropical mean upper tropospheric specific humidity since the mean specific humidity is linearly proportional to the total mass of water vapor, which in turn is mostly determined by the vertical transport of water vapor mass flux from the boundary layer by deep convection. Such mean specific humidity is often the variable used to characterize the zonally averaged moisture field and appropriate for simple idealized model. We do note here that the arithmetical mean is not enough for a complete understanding of water vapor effects on the climate. *Sherwood et al.* [2006] and *Ryoo et al.* [2009] showed departures from normal distribution for the tropical upper troposphere relative humidity, indicating the limited usage of the mean to characterize the PDF of tropical relative humidity. Such departures are important for the radiative impact of water vapor because of the highly nonlinear relation between UTH and OLR. Therefore, understanding how the PDF of the tropical UTH varies with surface variables or other dynamic factors is also important aspect in terms of advancing our knowledge of water vapor feedback, which is the focus of our future work.

2.6 Acknowledgments

We wish to thank Drs. Z. Johnny Luo, Hui Su, and Jonathon Wright for valuable discussions and comments. We also thank the two anonymous reviewers for their

thoughtful comments. AIRS data was obtained from NASA GSFC DAAC and ECMWF reanalyses from http://data.ecmwf.int/data/. GCM simulations were obtained from the WCRP CMIP3 Multi-model data archived at PCMDI, Lawrence Livermore National Laboratory. NOAA_OI_SST_V2 data was provided by the NOAA/OAR/ESRL PSD, Boulder, Colorado, USA, from http://www.esrl.noaa.gov/psd/. This study is partly supported by NSF ATM 0755310 awarded to University of Michigan.

Chapter 3

Interannual variations of basin-scale upper tropospheric water vapor and other climate variables

3.1 Introduction

While understanding the features associated with tropical mean upper tropospheric water vapor (UTWV) is important for us to delineate the overall UTWV variations in the tropics, equally interesting and important is to understand the regional variations of UTWV in the tropics. Tropical UTWV could exhibit regionally dependent variability because the roles played by local thermodynamics and large-scale dynamics can be different from one tropical ocean basin to another. For example, by analyzing four years of SSM/I data, *Bretherton et al.* [2004] investigated the relationship between total water vapor column (*Wt*) and surface precipitation rate (*Pr*) over four tropical oceanic regions and found that the relation between *Wt* and *Pr* varies from one region to another although the relations between column-mean relative humidity and *Pr* of all four basins follow roughly the same exponential curve. *Shin and Sardeshmukh* [2011] suggested that biases of the simulated mean state and the variation of tropical regional SST could lead to

significant errors in the projection of future precipitation, which highlighted the importance of tropical regional SST on the overall precipitation pattern and its long-term change. Figure 3.1 shows another example to highlight the differences between the tropical means and regional means. Using six-year retrievals of 215hPa water vapor mixing ratio and ice water content (IWC) from MLS [*Waters et al.*, 2006], Figure3.1a

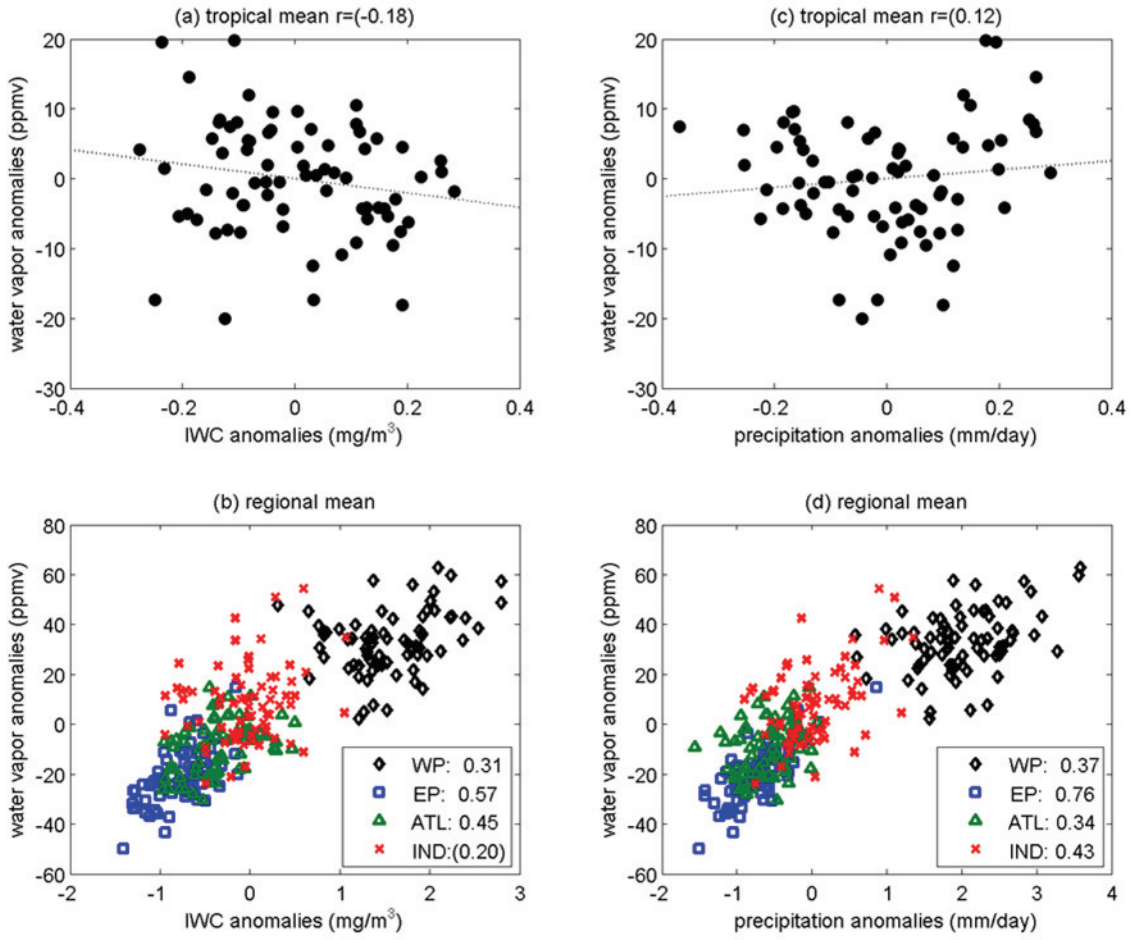

Figure 3.1. (a) Scatterplot of the deviation of tropical mean MLS 215hPa water vapor mixing ratio from its seasonal averages against that of ice water content over the whole tropics. (b) Scatterplot of the deviation of regional-average water vapor from tropical mean seasonal averages of water vapor against that of ice water content over four tropical ocean basins, namely the Western Pacific (WP), Eastern Pacific (EP), Atlantic (ATL) and Indian Ocean (IND). (c) and (d) are similar to (a) and (b), but against TRMM precipitation rate. The correlation coefficient between the two anomalies is also shown. The results with parentheses do not pass the significant test at 95% confidence level.

presents the scatterplot of tropical mean UTWV anomalies (i.e. deviation from tropical mean seasonal cycle) against the tropical mean IWC anomalies. These two anomalies of tropical mean quantities show little correlation and a statistically significant linear slope can not be obtained. In contrast, when the anomalies (still the deviation from the tropical mean seasonal cycle) of regional mean 215 hPa water vapor are plotted against those of IWC (Figure 3.1b), they show much better correlation and a statistically significant slope can be derived from regression analysis. A similar contrast between the tropical mean anomalies and regional mean anomalies (both are the deviation from the tropical mean seasonal cycle) is also obvious in terms of the precipitation anomalies from Tropical Rainfall Measuring Mission (TRMM) measurements when compared to the 215hPa water vapor anomalies (Figure 3.1c and 3.1d). Figures 3.1b and 3.1d stress the different regional behaviors over the tropical ocean: the western Pacific (WP) tends to be the wettest environment with the largest values of UTWV, IWC and precipitation, while the eastern Pacific (EP) is the driest environment with the smallest UTWV, IWC and precipitation.

As far as the regional variation of UTWV is concerned, it is related by local variables within the same region (e.g. sea surface temperature, SST) as well as factors in remote regions, the latter of which is usually referred to as teleconnections. The impact of remote-region SST on geophysical variables in a given region can be determined by the atmospheric circulation [*Wallace and Gutzler*, 1981; *Deser and Blackmon*, 1995; *Lau,* 1997; *Klein et al.*, 1999; *Alexander et al.,* 2002; *Liu and Alexander,* 2007] or through the ocean tunnels [*Liu and Yang*, 2003; *Liu and Alexander,* 2007]. The atmospheric branch of it is usually termed as the “atmospheric bridge”, which connects the equatorial eastern

Pacific and remote regions through atmospheric wave propagation and circulation in both latitudinal and zonal directions [e.g. *Klein et al*., 1999; *Alexander et al*., 2002; *Su and Neelin,* 2002; *Liu and Yang,* 2003; *Su et al.*, 2003; *Alexander et al.*, 2004; *Liu and Alexander*, 2007]. As shown in *Klein et al*. [1999], the atmospheric bridge is prominently dependent upon the seasonal cycle.

Based on facts in the previous paragraphs, two interrelated questions that are worthy for investigation are: (1) what are the observed and simulated relations between UTWV and the local variables over the same ocean basin at the interannual time scales and how can these relations be understood, and (2) how the atmospheric bridge is represented in the current GCMs and what are its impact on the simulated regional variations at the interannual timescale? In this chapter, we will use multiple years of UTWV and IWC measurements made by the Aura MLS to characterize such regional-scale (i.e. scale of ocean basin) interannual variations of UTWV and IWC from MLS measurements, and then evaluate how such regional features have been represented in several GCMs that participated in the IPCC AR4 assessment. Also examined will be the atmospheric bridge as simulated by these GCMs and how it would change in a simulation of future climate. The observed and simulated datasets, as well as the analysis methods, are summarized in Section 3.2. Section 3.3 describes the regional UTWV variations from the MLS observations and GCM simulations of the current climate. Section 3.4 examines how the atmospheric bridge, an important mechanism that affects the basin-scale climate, has been represented in the GCMs for both the current and projected climates. Conclusions and discussion are given in Section 3.5.

3.2 Data description and methodology

The MLS on Aura has provided simultaneous measurements of UTWV, IWC, upper troposphere (UT) temperature and several atmospheric chemical species [*Schoeberl et al*., 2006; *Waters et al*., 2006] since September 2004. MLS Version 2.2 Level 2 [*Livesey et al.*, 2007] products which contain water vapor, IWC and temperature at 215 hPa are used in this study. Detailed descriptions and validation of these parameters can be found in *Read et al.* [2007], *Wu et al.* [2008], and *Schwartz et al.* [2008]. The cloud fraction is computed according to the occurrence frequency of the IWC existence. In general, these parameters are scientifically useful for the levels at 215 hPa and above with a vertical resolution of ~3 km and a horizontal resolution of ~200 km for a footprint measurement along the satellite track. Such footprint measurements were used to generate monthly mean products over a 4° latitude by 8° longitude grid boxes as done in *Li et al*. [2005] and *Su et al.* [2006]. Monthly mean products from September 2004 to August 2010 are used in the analysis here. Monthly SST is obtained from NOAA Optimum Interpolation (OI) SSTs [*Reynolds and Marsico*, 1993; *Reynolds et al.*, 2002] with a 1° by 1° resolution. Monthly precipitation from Tropical Rainfall Measuring Mission (TRMM) product 3B43 [*Huffman et al.,* 2007] over the same time period is used in this analysis.

For comparison, the monthly mean outputs from five coupled-GCMs in IPCC AR4 archives are examined, including GFDL CM2.1, ECHAM5, MRI CGCM2.3.2, UKMO HadCM3 and NCAR CCSM3. Relevant details of the five GCMs can be found in the Appendix at the end of this chapter. January 1970 through December 1999 in the 20th century simulation (historical run) is analyzed and is denoted as the current-climate simulations; and January 2070 through December 2099 in the simulations based on the

SRES A2 scenario is denoted as the future-climate simulation in the rest of this chapter. SRES A2 is the scenario with the largest increase of CO_2 concentration among all IPCC AR4 future scenarios.

Four ocean basins within 20°S to 20°N tropics are examined. The definitions of these basins are identical to *Bretherton et al.* [2004], namely, the Western Pacific (WP), Eastern Pacific (EP), Atlantic (ATL) and Indian Ocean (IND) as shown in Figure 3.2. Unless depicted in other ways, interannual anomalies (for brevity, hereafter interannual anomalies and anomalies are used interchangeably) are calculated by removing the trend and mean seasonal cycle from the original dataset and then applying a 13-month running average.

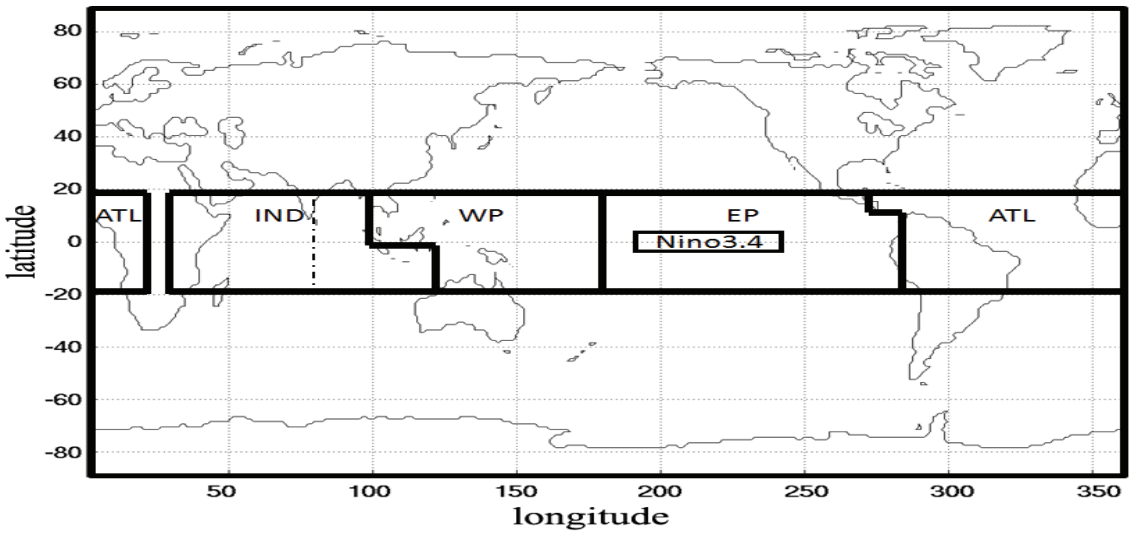

Figure 3.2. Four tropical ocean basins used in the analysis. The Nino 3.4 region is also labeled.

3.3 Basin-scale UTWV anomalies

3.3.1 Observations

Figures 3.3a and 3.3b show the scatterplots of interannual anomalies of the tropical mean water vapor at 215 hPa with respect to those of tropical mean temperature (both the

SST and the air temperature at the same level), while Figures 3.3c, 3.3d and 3.3e are the scatterplots of 215hPa water vapor anomalies with respect to the anomalies of ***cloud variables*** (referring to IWC, precipitation and cloud fraction). As expected, the tropical mean anomalies of 215 hPa water vapor are highly correlated with tropical mean anomalies of temperatures (both surface and 215hPa temperatures) with correlation coefficients larger than 0.95. In contrast, the tropical mean UTWV is negatively correlated with the cloud variables. As shown in following sections, these negative correlations originate from the partial cancellation of positive and negative correlations in

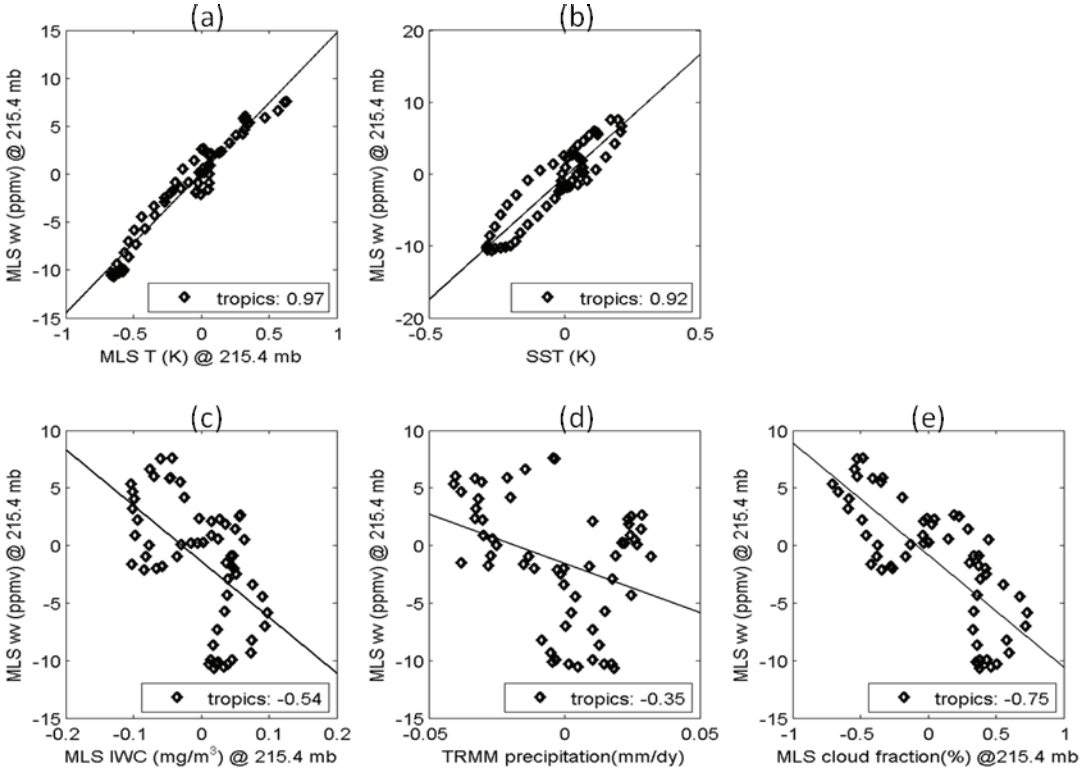

Figure 3.3. Scatterplots of interannual anomalies of the MLS 215hPa water vapor and that of (a) MLS 215hPa temperature, (b) NOAA SST, (c) MLS 215hPa IWC, (d) TRMM precipitation, and (e) MLS 215hPa cloud occurrence. The correlation coefficient is labeled as well.

different regions of the tropics, which have also been mentioned in previous studies such as *Su et al*. [2001], *Su and Neelin* [2002], and *Su et al*. [2003].

The basin-scale anomalies are shown in Figure 3.4. The observed interannual anomalies of basin-mean UTWV are strongly correlated with those of the UT temperature, tropical mean SST and basin-averaged local SST for all four basins (with a mean correlation coefficient of 0.86). However, the correlations with basin-averaged cloud variables exhibit different behaviors in each of the four basins. The UTWV anomalies in the EP have positive correlations with basin-scale anomalies of cloud variables, but the UTWV anomalies in WP and ATL are negatively correlated with based-scale anomalies of cloud variables. All of these correlations are statistically

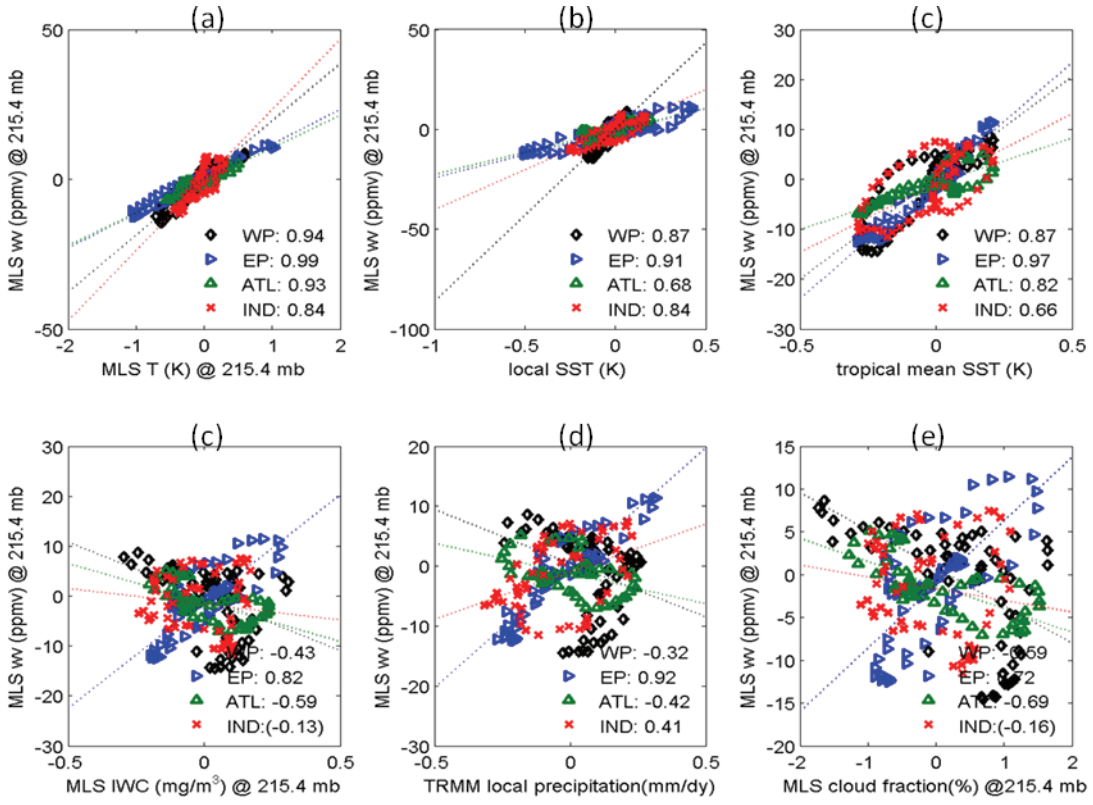

Figure 3.4. Similar to Figure 3.3, but for the basin-average variables in the four ocean basins.

significant. For the Indian Ocean (IND), the correlations between MLS UTWV and MLS IWC and cloud fraction anomalies are negative but statistically not significant, while the correlation between MLS UTWV and TRMM precipitation is positive and statistically significant. These correlations with opposite signs within different basins partially cancel with each other and lead to overall negative correlations in Figures 3.3c, 3.3d and 3.3e when the tropical mean anomalies are examined. These correlation coefficients between UTWV and temperature variables, as well as cloud variables, are summarized in Figure 3.5a.

3.3.2 Model simulations of the 20th century

Similar correlation analyses are applied to the five CMIP3 GCMs archived for the IPCC AR4: GFDL CM2.1, ECHAM5, MRI CGCM2.3.2, UKMO HadCM3 and NCAR CCSM3. Since the models do not have an output at 215hPa, the anomalies of 200hPa specific humidity from the 20th century experiment (20c3m run) are used to correlate with anomalies of temperature variables; i.e., 200hPa temperature (Tair), basin-scale local SST (basinSST), tropical mean SST and the EP (eastern Pacific) SST in addition to anomalies of cloud fraction and precipitation rates in the same basin. IWC is not available in the GCM output archived for the IPCC AR4. The EP SST is chosen for the role of eastern Pacific SST in the atmospheric bridge and ocean tunnels. The results are summarized in Figure 3.5b. Similar to the observations, the correlations between UTWV anomalies and temperature anomalies (same-level or SST, same-basin or EP or tropical mean) are all strongly positive. But the correlations with local cloud variables are different from model to model and do not always agree with the observations. The only exception is the EP (blue bars in Figure 3.5), where all the models agree with the observations of a strong

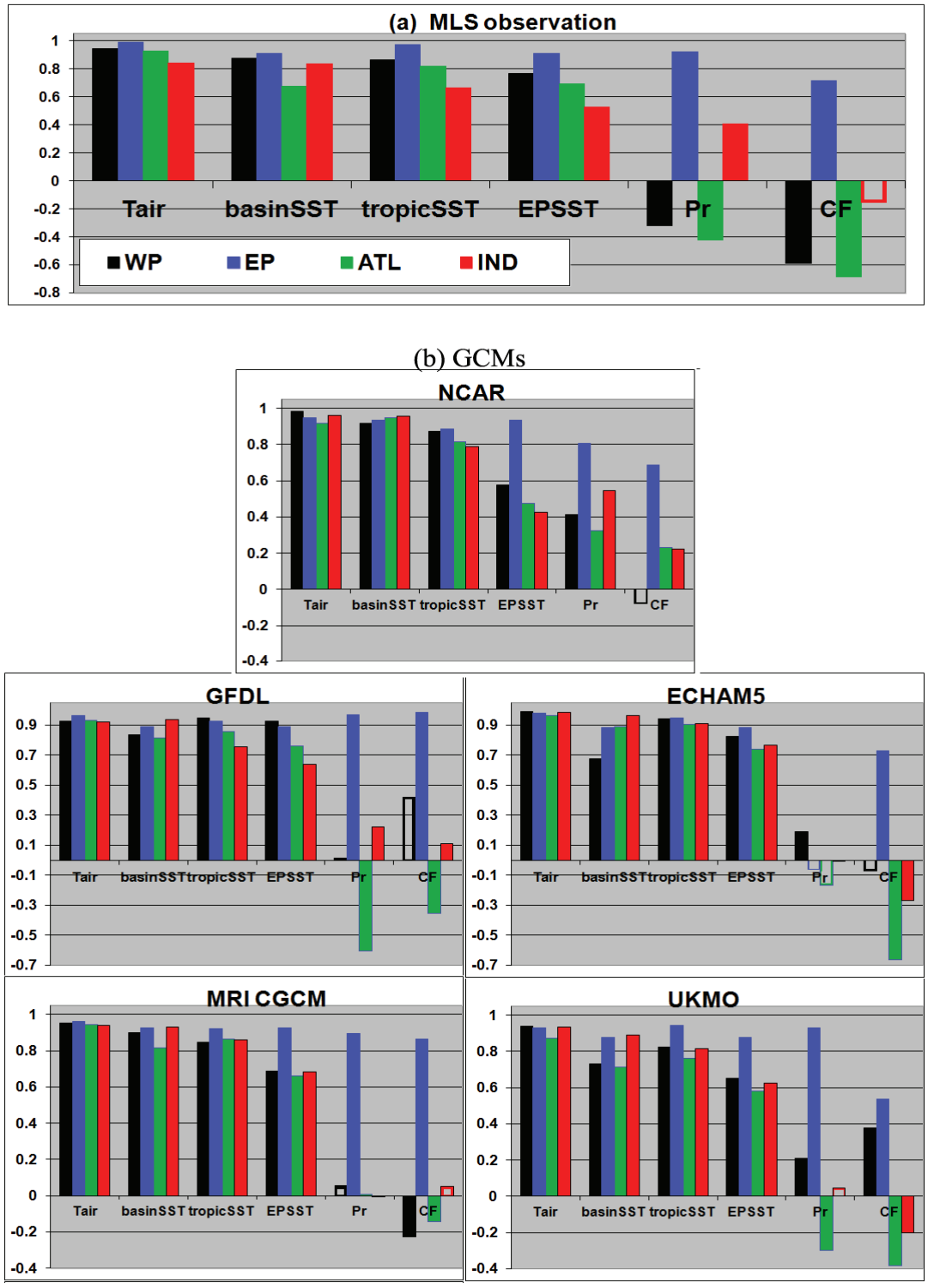

Figure 3.5. (a) The correlation coefficients between MLS 215hPa water vapor and several variables from observations. (b) Similar to (a), but for the five GCMs. Hollow bars are results which do not pass the 95% confidence level.

positive correlation between UTWV anomalies and cloud fraction or precipitation anomalies.

3.3.3 Characteristics of each basin

Figure 3.5 is useful to help understand the control mechanism of UTWV and cloud variations at the interannual timescale. The largest interannual variation in the tropics is the ENSO (El Nino and Southern Oscillation) cycle. At the El Nino phase of the cycle, ascending branch of the Pacific Walker circulation moves eastward beyond the date line (i.e. into the EP basin in this study), thus increased deep convection activates which brings more moisture into the EP upper atmosphere and leads to a warmer upper troposphere (below the tropopause) than that of the climatological mean. Such UTWV and UT temperature anomalies, however, will quickly propagate and mix over the entire tropical belt. Meanwhile, the SST in other regions will be also affected by such anomalies [*Klein et al.*, 1999]. These chains of action explain the high correlation between temperature and UTWV anomalies, as well as the high correlations between UTWV anomalies and anomalies of cloud variables in the EP. For other basins, the correlation between UTWV anomalies and local cloud variables is now complicated by the fact that UTWV is modulated remotely by the variations in the EP basin as well as by local convective activity. The anomalies of local convective activity, meanwhile, can be affected by the variations at EP basin as well. For example, at the El Nino phase, the deep convection activity will be suppressed in the western Pacific (WP) due to the change of locations for the Walker circulation, but the UTWV anomalies over the WP can be still positive if the influence from the EP UTWV is dominant. If so, the correlations between UT anomalies and cloud variable anomalies would be negative, as shown in the MLS

observation (Figure 3.5a). However, models do not always show negative correlations for the WP UTWV versus cloud variables, which suggest that the local influences on the UTWV anomalies may be too strong in the GCMs. Note a caveat here is that the cloud variables that are used here can be related to both the stratiform and convective clouds. No convective-related variables are available in all models analyzed here or generally speaking archived for the IPCC AR4, hence such cloud variables are used. However, over the WP, the cloud fraction and precipitation should be closely related to deep convection activities.

For MLS observations and the GFDL and NCAR model simulations, the UTWV anomalies in the Indian Ocean (IND) have the weakest correlation with the EP SST anomalies among all basins. For the remaining three GCMs, it is the second weakest correlation among all basins (Figure 3.5). Moreover, in terms of the correlation between the IND cloud variable and UTWV anomalies, the IND results disagree most among all GCMs as well as between models and observations. These warrant a further investigation of the analysis of the IND region.

It has been suggested that the Indian Ocean has a dipole structure of SST pattern that is independent of the ENSO cycle [*Saji et al*., 1999; *Webster et al.,* 1999], normally referred to as Indian Dipole. Several studies have found important influences of the IND SST anomalies on the local and nearby regions [*Goddard and Graham*, 1999; *Vinayachandran et al*., 1999; *Li et al*., 2003; *Hong et al.*, 2008]. Separating the Indian Ocean into western and eastern parts, *Saji et al.* [1999] found that different SST anomalies lead to different rainfall patterns in these two sub-basins. Recently, *Hong et al.* [2010] attributed the different responses of two sub-basins in IND to the asymmetry of

the mixed layer depth (MLD). During the ENSO warm events, the western portion of the IND has a deeper MLD than the eastern portion. Since the eastern and western sub-basins are different in many aspects regardless of the physical origins of each, we separate the IND into western (W_IND) and eastern (E_IND) sub-basins by 80°E, as done in studies mentioned previously in this paragraph. Figure 3.6 shows the observed correlations between the UTWV anomalies and those of several variables in the IND as well as the two sub-basins of the IND. The W_IND (pink bars in Figure 3.6) have positive correlations between UTWV anomalies and all cloud variables while the E_IND have negative correlations for the cloud fraction and IWC. It is such opposite correlations for the cloud fraction that makes the correlation for the entire IND basin insignificant (Figure 3.5a). This suggests that, in terms of regional climate analysis, it is worthwhile to study the two sub-basins of the Indian Ocean separately.

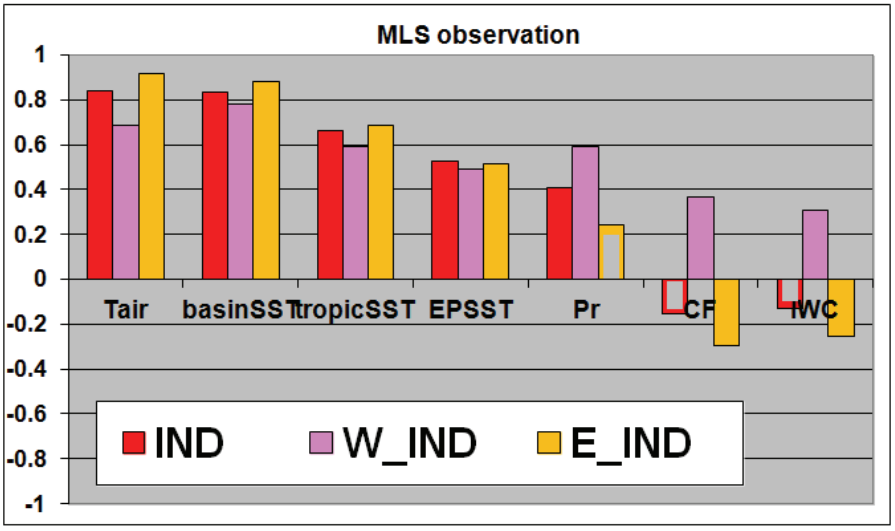

Figure 3.6. The correlation coefficient between MLS 215hPa water vapor anomalies and anomalies of several variables over the IND basin and its two sub-basins (western and eastern portions). Hollow bars are results which do not pass the 95% confidence level.

3.4 Atmospheric bridge

Atmospheric bridge refers to the atmospheric teleconnection between the SST anomalies over the equatorial Pacific region and SST anomalies region away from the equatorial Pacific region (referred to as remote region) during the ENSO events. The impact of ENSO on remote regions can be achieved through the atmospheric bridge and through the ocean tunnel. Figure 3.7 illustrates the concept of how the atmospheric bridge and the ocean tunnel system work. In this section, we first connect the basin-scale variables to the EP SST (since it can be deemed as the main forcing for the atmospheric variations at the interannual timescale). Then we apply the atmospheric bridge concept to explain such basin-scale averaged variables and SST variations, and finally we explore how the atmospheric bridge as well as its seasonal dependence have been represented in the GCMs.

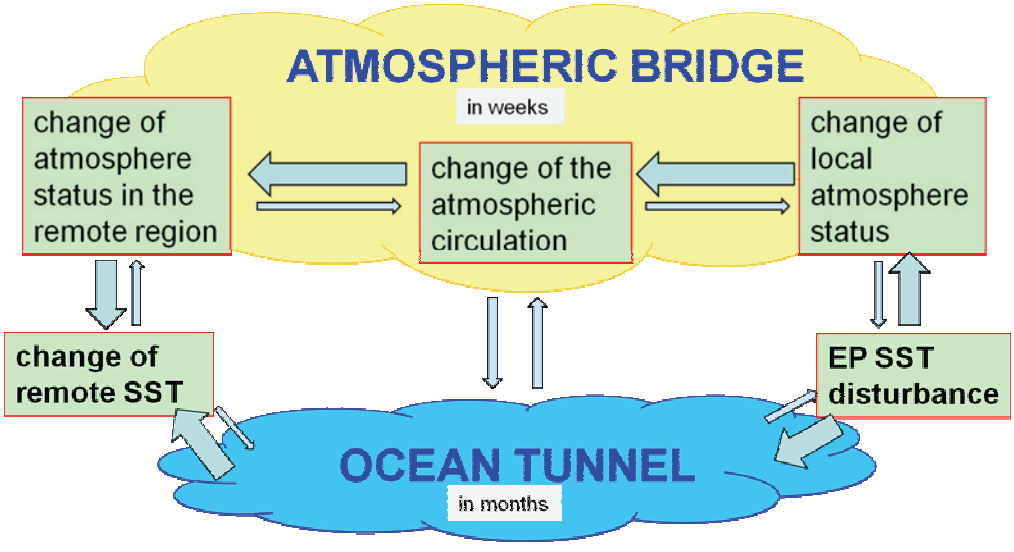

Figure 3.7. A sketch of how the EP SST influences the remote regions via ocean tunnel and atmospheric bridge.

3.4.1 Responses to the EP SST forcing

Changes in tropical convection related to the EP SST anomalies during an ENSO event influence the global atmospheric circulation and therefore affect the remote region via the atmospheric bridge. From this perspective, the EP SST disturbance (anomaly) is deemed as the main forcing signal at the interannual timescale. Table 3.1 shows the correlation coefficients between the anomalies of the observed EP SST and anomalies of basin-mean water vapor, temperature, IWC and CF at 215 hPa from MLS observations. It also shows the correlation between the EP SST anomalies and Pr anomalies from TRMM. The basin-scale UTWV and UT temperature anomalies are strongly correlated to the EP SST anomalies although the correlations in the IND (and its two sub-basins) are relatively small. The correlations between the EP SST and the EP cloud variables are all positive, while the correlations with cloud variables in the other basins are all negative. GCM simulations are generally consistent with the observed result (Figure 3.8). This

w.r.t. EP SST	WP	EP	ATL	IND	W_IND	E_IND
q_{215hPa}	0.77	0.91	0.69	0.53	0.49	0.51
T_{215hPa}	0.74	0.87	0.68	0.62	0.65	0.54
IWC_{215hPa}	-0.71	0.92	-0.59	-0.58	(-0.11)	-0.86
CF_{215hPa}	-0.75	0.85	-0.71	-0.65	(-0.11)	-0.88
$Pr_{surface}$	-0.35	0.92	-0.70	-0.42	(-0.06)	-0.56

Table 3.1. The correlation coefficients between the interannual anomalies of the EP SST and those of other variables in different ocean basins. Results from 6-year data of MLS observation. Results with parentheses do not pass the 95% confidence level.

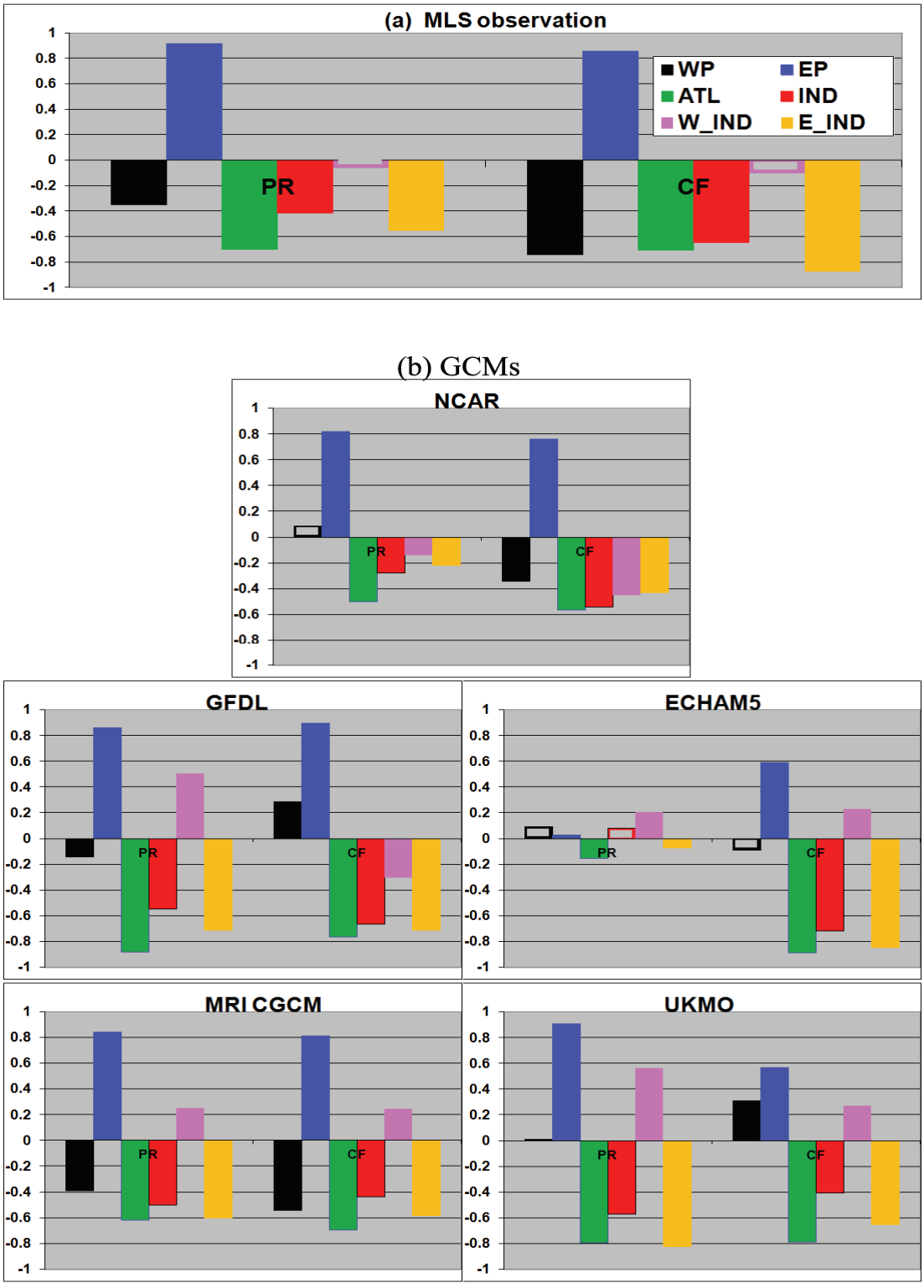

Figure 3.8. (a) The correlation coefficients between the EP SST and several variables from observations. (b) Similar to (a), but for the five GCMs. Hollow bars are results which do not pass the 95% confidence level.

consists with the explanation that the EP SST forcing enhances the anomalous convection over the EP and, correspondingly, reduces the convection (or cloud activities) over the other basins at the interannual timescale. In other words, to a large extent the EP acts as a forcing region while the other three basins act as response regions. The insignificant correlations between the W_IND cloud variables and the EP SST imply that the W_IND cloud and convection variations may be largely modulated by its own SST variations (Figure 3.6) instead of the EP SST via the atmospheric bridge. Figure 3.9 shows a schematic plot of the connection among these interannual variations to the EP SST and illustrates the concepts of the forcing and accordingly the responses. When the EP SST anomaly is positive, the anomalous convection in the EP is enhanced. The UTWV and temperature anomalies from such enhanced convection are "felt" by the entire tropics because the quick mixing (in the timespan of weeks) is mainly through wave

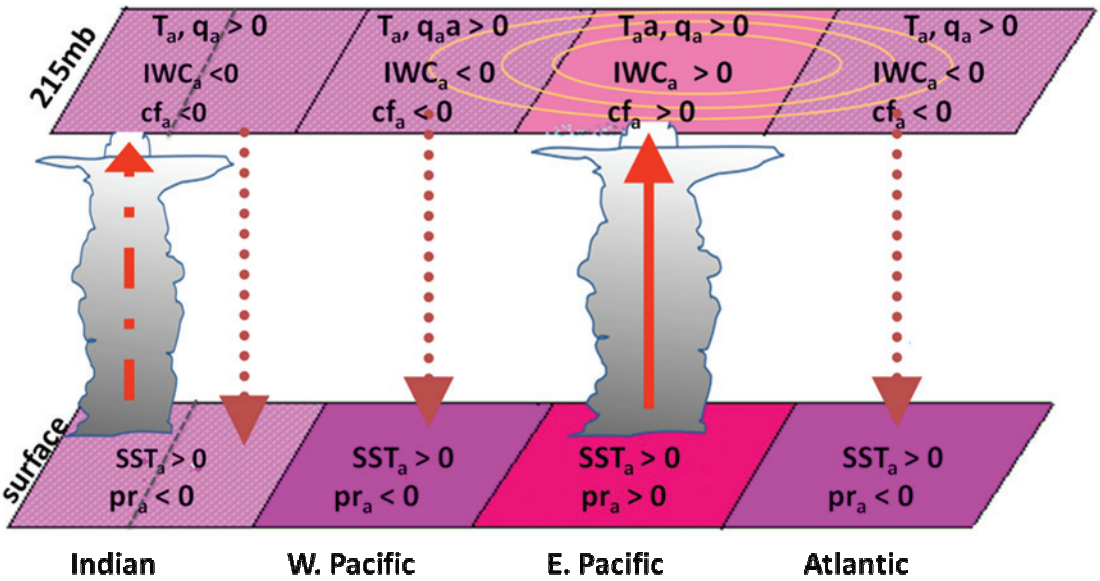

Figure 3.9. Sketch of connections between UT and surface variables of the four ocean basins via the atmospheric bridge. The subscript "$_a$" indicates the interannual anomaly. The signs of these anomalies are with respect to enhanced EP SST anomalies (refer to Table 3.1).

propagations throughout the atmosphere [*Su and Neelin*, 2002]. The convective activity and UT clouds in other basins are meanwhile reduced due to: (1) the SST pattern change within its own basin; (2) a warmer upper troposphere increasing the thermal stability therefore reduces the convection that can reach the UT; (3) a warmer upper troposphere also is less favored for the in-situ cloud condensation and more in favor for the in-situ cloud dissipation via evaporation. For the W_IND sub-basin, the local SST is likely as important as, if not more than, the EP SST forcing.

3.4.2 Representations of atmospheric bridge in GCMs

Klein et al. [1999] showed that the increased surface heat flux is responsible for the change of surface temperatures in the eastern Indian Ocean and South China Sea, and a weakening of the trade winds reduces surface evaporation and thus enhances SSTs in the tropical North Atlantic. The important seasonal dependence of the atmospheric bridge was also stressed in *Klein et al.* [1999]. In this section, the methodology used in *Klein et al.* [1999] is followed to explore how the GCMs represent the atmospheric bridge mechanism as well as its seasonal dependence in the current climate and future climate.

As described in Section 3.2, time series of the basin-averaged SST and surface net heat fluxes are taken from the last 30 years of the 20th century (20c3m) run and from the 21st century A2 scenario run, respectively. All data are detrended by linear regression, deseasonalized by removing their seasonal mean and applied with a 5-month running mean as done in *Klein et al.* [1999]. The EP SST anomaly (using a 5-month running mean instead of a 13-month running mean) is defined as the "ENSO index" in this section. Three basin-mean variables, the SST, surface next flux, and SST tendency, are used to calculate the lead- or lag-regression with the ENSO index in the same way as

done in the *Klein et al*. [1999]. i.e. computing the linear regression of the anomalies with respect to the ENSO index for various lead or lag time periods (-12 to +12 months) and then scaling the regressed slope by the standard deviation of the ENSO index. The surface net heat flux is computed from the surface net shortwave flux, net longwave flux, surface sensible heat and latent heat fluxes. The SST tendency is computed by central differencing of the monthly-mean SST fields.

Figure 3.10 shows the scaled regression slopes for the WP, ATL and IND basin-mean SST anomalies for the 20th and 21st centuries. Positive values of the abscissa indicate that the ENSO index is leading ahead of the SST anomalies while negative values are indicative of lagging behind the SST anomalies. For the 20th century, the WP SST anomalies in the boreal early summer (~May-Jul) are best correlated with the ENSO index 5 months prior (i.e. the preceding winter/spring) for all GCMs except the CGCM. For the 21st century, all five GCMs roughly exhibit a consistent change regarding the seasonal dependence of the WP SST versus ENSO index (the peak is 2 calendar months earlier than that in the 20th century). The SST anomalies in the ATL and IND basins show the largest regression slope in the early boreal springtime of the 20th century and the seasonal dependences remain same in the 21st century, except with the UKMO.

The regression is also computed for the anomalies of the net surface heat flux and SST tendency for three basins (Figure 3.11). For the ATL and IND basins, the regression patterns between the surface net heat flux and the SST tendency are closely tracking with each other. This confirms that SST anomalies in the ATL and IND basins respond to the ENSO variation mainly through the atmospheric bridge [*Lau and Nath*, 1994; *Klein et al*., 1999; *Lau and Nath*, 2001; *Liu and Alexander*, 2007]. Unlike the ATL and IND, the WP

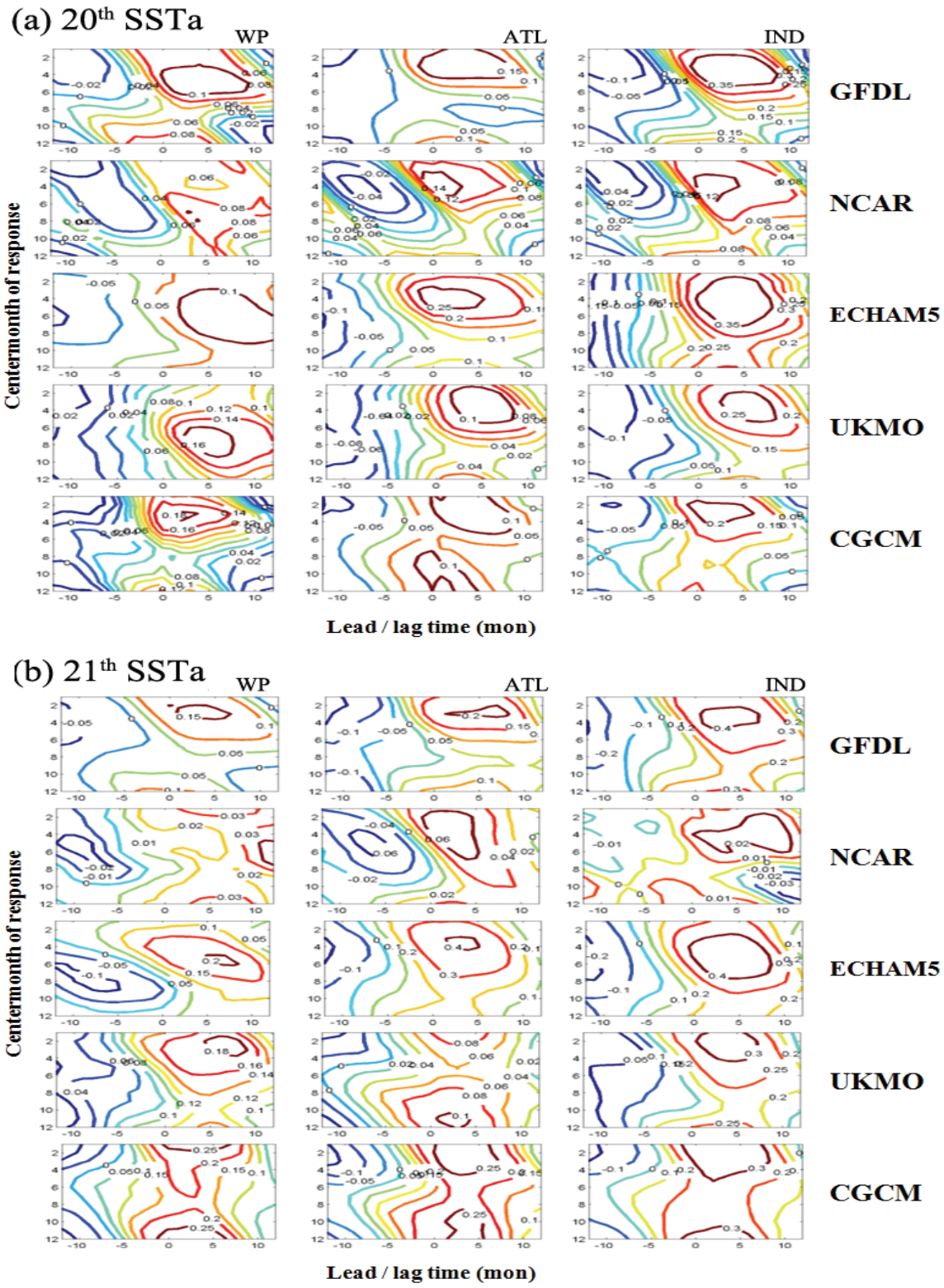

Figure 3.10. Time-lag regression of SST anomalies onto the ENSO index scaled by the standard deviation of the ENSO index. (a) for 20th century and (b) for 21st century. Positive lag indicates that the SST anomalies lag the ENSO index.

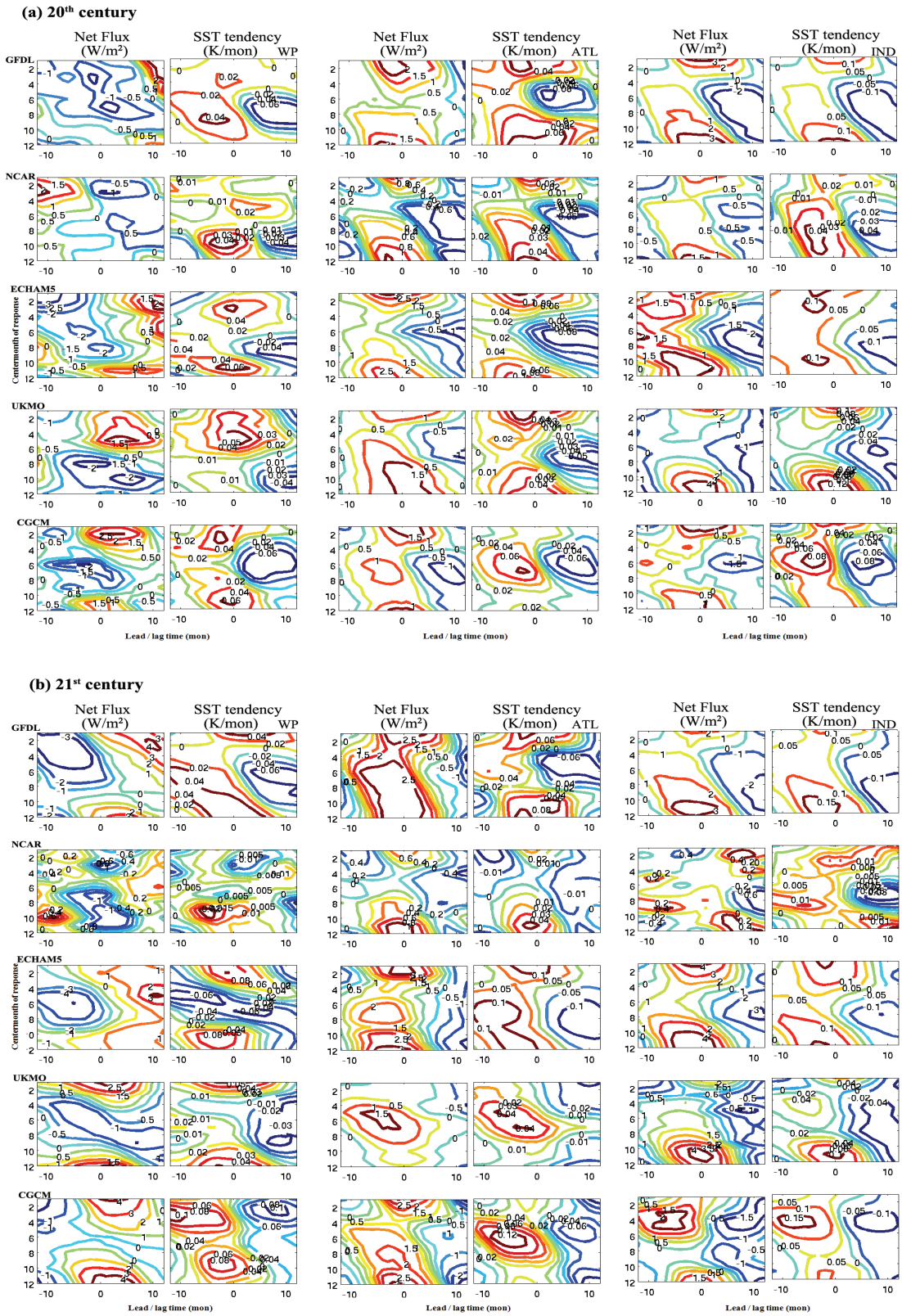

Figure 3.11. Similar to Figure 3.9 but for anomalies of surface net flux and SST tendency. (a) for 20th century and (b) for 21st century.

in all GCMs does not show a strong similarity between the patterns of regression slopes of surface net flux and SST tendency. In addition, the peak amplitude of the WP SST regression slope is the smallest among all three basins in the GFDL, NCAR and ECHAM5 models. The seasonal dependence of the net flux (SST tendency) on the ENSO index remains the same in the two centuries for all basins and for all GCMs except for the UKMO. The UKMO model has the maximum regression advanced by 4-6 months by the end of the 21st century in the A2 scenario run.

The similarity between the surface net flux and the SST tendency over the IND and ATL basins indicates that the major contribution of SST tendency is from the atmospheric bridge mechanism. To evaluate how much SST tendency can be explained by the surface net flux, the estimated corresponding SST tendency for any given surface net flux can be given by:

$$SSTtendency\,|_{flux} = \frac{F_{net}}{MLD \cdot \rho_{sea} \cdot Cp_{sea}} \tag{3.1}$$

where F_{net} is the surface net flux, MLD is the mixing layer depth, ρ_{sea} is the density of ocean waters and Cp_{sea} is the heat capacity of the ocean water. The MLD for each basin is taken from the climatology compiled by *de Boyer Montegut et al*. [2004]. Figure 3.12 shows the time series of the interannual anomaly of the SST tendency (blue line) and that of the SST tendency derived from the surface net flux (SST tendency$|_{\text{flux}}$, red line) over the IND and ATL basins. The amplitude of these two sets of SST tendency anomalies is comparable. The mean correlation coefficients between the two sets of SST tendency anomalies of the five GCMs are 0.80 and 0.74 over the IND and ATL basin, respectively. Then the contribution of surface net flux to SST tendency is estimated by using the linear regression slope of SST tendency$|_{\text{flux}}$ and merging it onto the SST tendency (i.e. for every

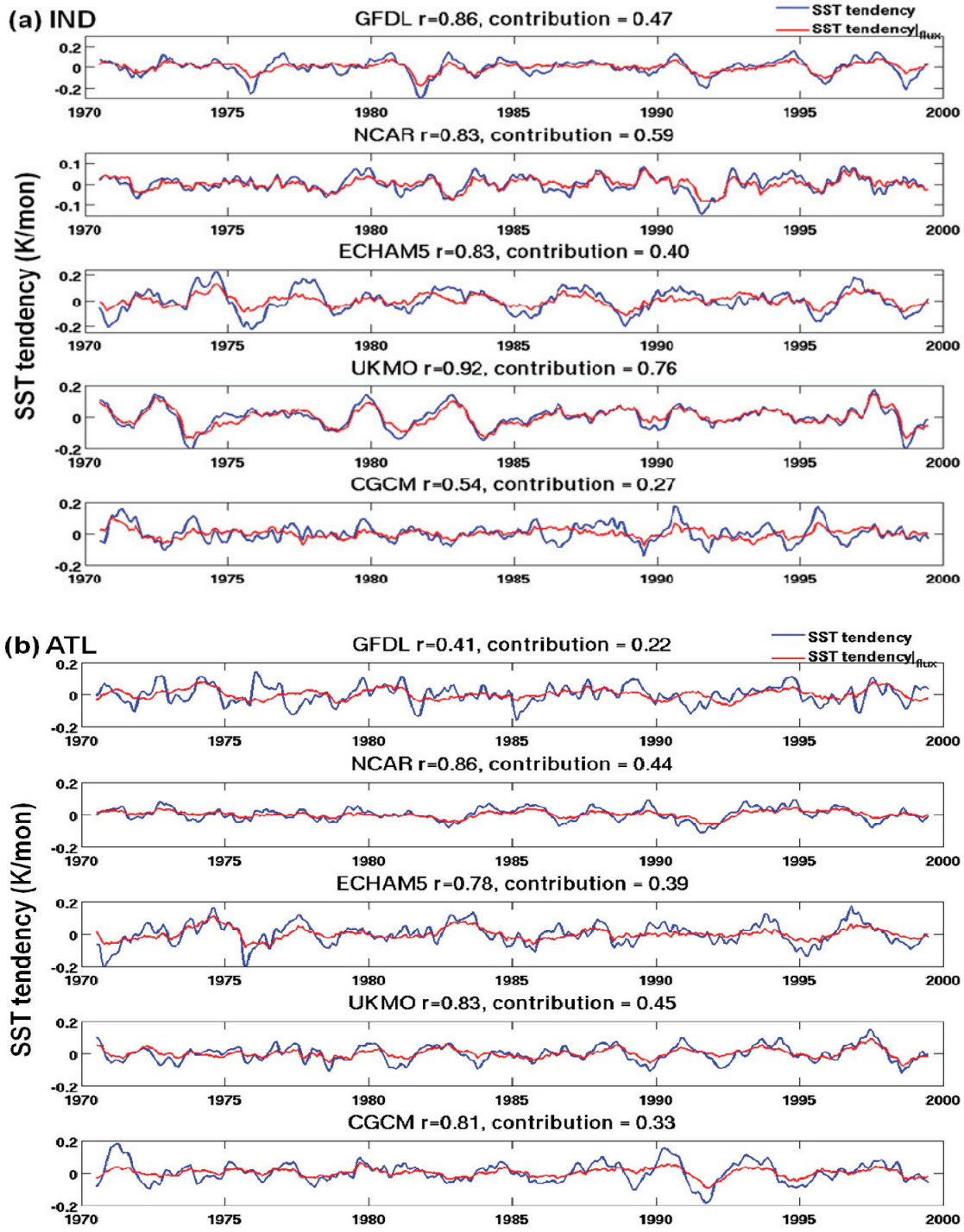

Figure 3.12. Time series of the interannual anomaly of the SST tendency from the GCMs (blue) and that of the SST tendency derived from the surface net flux (red) over the (a) IND and (b) ATL basin. The correlation coefficient between the two sets of anomalies and the contribution from the net flux to the SST tendency are shown. Refer to the context for the definition of the contribution.

1K/mon change of SST tendency, how many K/mon is contributed from the surface net flux according to Eq. 3.1). Over the IND basin, the regression slope varies from 27% to 76% among the five GCMs. Over the ATL basin, they have a smaller range and only vary from 22% to 45%.

Figure 3.13 is a "Taylor-like" diagram for synthesizing multiple aspects of modeled atmospheric bridge for both the current climate and future climate. The radial coordinate shows the standard deviation of the ENSO index in K (i.e. amplitude of SST anomaly in the EP). The angular coordinate is the correlation coefficients between regressed pattern of surface next flux and that of SST tendency (as those in Figure 3.11). As depicted in the previous paragraph, the IND (red points) and ATL (blue points) exhibit larger correlation coefficients between the two patterns than the WP. The change of the ENSO amplitude is different from model to model, similar as what has been documented in the IPCC AR4 report [*Meehl et al.*, 2007].

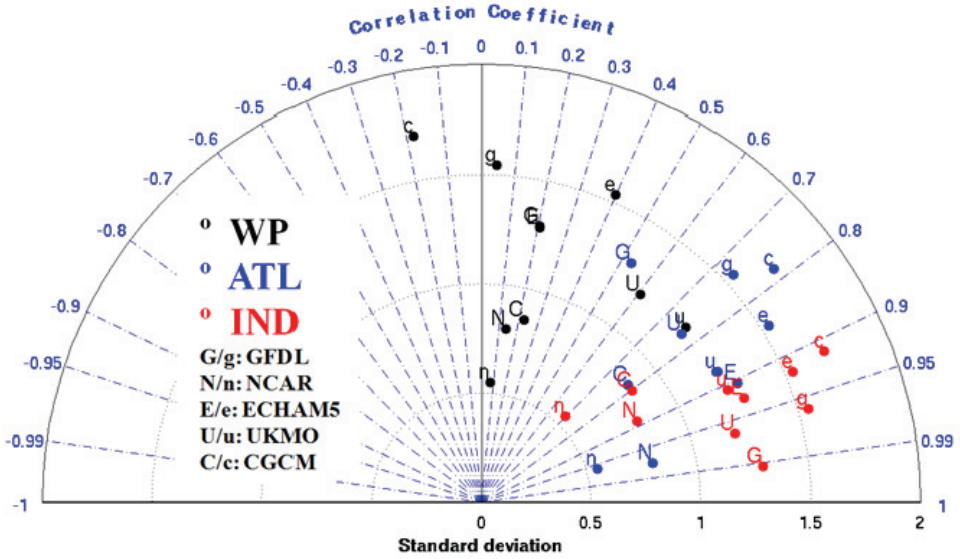

Figure 3.13. A "Taylor-like" diagram. Radial coordinate is the standard deviation of the ENSO index of each GCM in K. Angular coordinate is the correlation coefficient of the patterns between time-lagged net flux and SST tendency as shown in Fig.3.10. Upper-case symbols are for the 20th century.

3.5. Conclusion and discussion

Using six years of 215hPa water vapor and ice water content observed by Aura MLS and SST data set from NOAA (September 2004 − August 2010), the interannual variations of UTWV in the four tropical ocean basins (i.e. the WP, EP, ATL, and IND) are investigated. Both MLS observation and the GCMs show that interannual variations of basin-scale UTWV are strongly correlated with variations in the UT temperature and tropical mean SST for all four basins. However, the correlations with local basin-scale cloud variables (e.g. IWC, CF, and Pr) are different. Models and observations agree mostly on the local correlations in the EP, in which the correlations tend to be positive and statistically significant. For other basins, models and observations show diverse results. The significant negative correlations between the WP and ATL cloud variables and the EP SST anomalies suggest a relationship between the WP and ATL suppressed convection, as well as cloud activities and the EP SST positive anomalies at the interannual time scale, which can be physically explained by the atmospheric bridge in response to the ENSO cycle. The Indian Ocean SST anomalies have a stronger correlation with the local UTWV anomalies than the WP and ATL do. Further separating the IND into two portions at 80°E (namely, W_IND and E_IND) shows that the UTWV correlations with local cloud variables are more prominent in the W_IND than in the E_IND. The UTWV and UT cloud variables in the W_IND are suggested to be dominated by their local SST forcing rather than remotely controlled by the EP SST. On the other hand, the cloud variables in the E_IND show a significant negative correlation with the EP SST anomalies, indicating their vulnerability to the EP SST forcing. Our study confirms that, at the interannual timescale, the EP acts as a forcing region due to

the shift of regions of convective activities over the ENSO cycle and that the WP and ATL are the most likely response to such EP forcings (Figure 3.9).

We also explore how the GCMs represent the regulating of the remote-region SST via the atmospheric bridge. Basin-scale anomalies of SST and surface net flux from the last 30 years of the 20th century (20c3m run) and the 21st century (A2 scenario) from five GCMs are analyzed. Following the study of *Klein et al*. [1999], the ENSO index is used to correlate these anomalies. Similar time-lag regression patterns of surface net flux and SST tendency are found across five GCMs over the IND and ATL basins, but not over the WP. Since the WP and EP are sub-basins of one entire tropical Pacific, the equatorial ocean tunnel may have a considerable contribution on regulating the WP SST. The disagreement on the WP and agreements on the other basins highlight the complicated challenges in GCMs to correctly represent both atmospheric and ocean responses in the WP to the EP SST anomalies. The seasonal dependences of SST, SST tendency and surface net flux on the ENSO index are also examined. The UKMO model exhibits a different seasonal dependence from the rest of the models when the current-climate and future-climate simulations are compared. The maximum regression slope is advanced by 4 to 6 months in the 21st century comparing to that in the 20th century. The remaining GCMs do not show such a significant difference in the change of seasonal dependencies.

This study corroborates the important role played by the atmospheric bridge in regulating the UT water vapor and cloud variables at the interannual time scales and stresses the importance of the eastern Pacific in affecting regional climate in other tropical basins. For the convenience of depiction, we coin the term “EP SST forcing”. As shown in *Shin and Sardeshmukh* [2011], having a correct representation of EP SST is not

only vital to the simulation of tropical climate, but also crucial to the simulation of mid-latitude climate over major continents such as North America. However, the EP SST can be affected by the ocean circulation (e.g. the coastal upwelling along the South American Pacific coast), as well as the atmospheric condition (e.g. the cover of marine stratus off the Peru coast of Pacific) [*Xie and Philander*, 1994]. The change of marine stratus, and more generally low cloud feedback, for future climate projections are still not well understood [*Solomon et al.*, 2007; *Clement et al.*, 2009; Broccoli and Klein, 2010], which in turn increases the uncertainty about the future EP SST change. Another recent study worth to note is the wind-evaporation-SST (WES) feedback hypothesis proposed by *Xie et al.* [2010], which offers a physical mechanism to explain the patterns of SST change in global warming experiments. WES assumes that the increase of downward radiant flux at the sea surface is balanced primarily by the increase of evaporation. For regions with a large increase of surface winds, little SST change is needed for the increase of evaporation. For regions with little change in surface winds, SST change has to be large in order to reach the desired amount of evaporation. *Xie et al.* [2010] uses WES to explain the SST pattern changes in both GFDL CM2 and NCAR CCSM experiments. It would be interesting in any future work to explore whether regional changes at the interannual time scale, like an extension of what have been done in this chapter, support the WES hypothesis or not.

3.6 Acknowledgements

The author is greatly indebted to Drs. H. Su and J. Jiang at NASA JPL for their help on understanding the MLS data. The majority of work of section 3.3 was formulated and mentored by Drs. H. Su and J. Jiang when the author worked as a summer intern at

NASA JPL in her second year of Ph.D. work. The GCM outputs are obtained from the WCRP CMIP3 Multi-model data archived at PCMDI, Lawrence Livermore National Laboratory.

3.7 Appendix

Below is a table summarizing relevant information of each GCM used in the study presented in this chapter.

GCMs	**Horizontal resolution**	**Stratiform cloud scheme**	**Convection scheme**	**Dynamic Core**
GFDL-CM2.1	2.0°×2.5°	Microphysics: [*Rotstayn*, 2000] Macrophysics: [*Tiedke,* 1993]	Relaxed Arakawa-Schubert [*Moorthi and Suarez,* 1992]	Finite volume
ECHAM5	T63 (~1.875°)	[*Lohmann and Roeckner*, 1996]	*Tiedtke* [1989] and *Nordeng* [1994]	Spectral
MRI-CGCM2.3.2	T42 (~2.8°)	Diagnostic [*Yukimoto et al*., 2001]	Prognostic Arakawa-Schubert [*Randall and Pan,* 1993]	Spectral
UKMO-HadCM3	2.75°×3.75°	[*Smith,* 1990] modified by [Gregory and Morris, 1996]	[*Gregory and Rowntree,* 1990] with addition of convective downdrafts [*Gregory and Allen*, 1991]	Finite difference
NCAR-CCSM3	T85 (~1.4°)	[*Rasch and Kristjansson*, 1998] [*Zhang et al.*, 2003] [*Boville et al.*, 2006]	[*Zhang and McFarlane*, 1995] [*Hack,* 1994]	Spectral

Table 3.a.1. Summary of the relevant information about five GCMs used in this study.

.

Chapter 4

A constraint for ice cloud feedback over the tropical Pacific in future climate change

A concise version of this chapter was submitted to and currently under revision for *Nature Climate Change* as

> Huang, X., H. Chuang, Y. Ming and G. L. Potter, A constraint for ice cloud feedback over the tropical Pacific in future climate change.

4.1 Introduction

Due to the significance of tropical ice clouds in radiation budget and hydrological cycle [*Liou*, 1986; *Stephens*, 2005], the complicated interactions among ice cloud microphysics, large-scale dynamics, and radiation [*Liou and Ou*, 1989; *Jakob*, 2002; *Tao et al.*, 2003], as well as the challenges of understanding ice cloud measurements from different remote sensing techniques [*Waliser et al.*, 2009; *Wu et al.*, 2009], simulation of ice clouds and understanding its role in the future climate remain high priority but challenging tasks in the current climate modeling and observing efforts. Progress has

been made in the understanding the altitude feedback of ice clouds, for example the FAT (Fixed anvil temperature) and PHAT (Proportionately Higher Anvil Temperature) hypotheses proposed by *Hartmann and Larson* [2002] and *Zelinka and Hartmann* [2010]. These hypotheses are based on physical arguments of heat budget and balance in the tropics and have been generally supported by data and simulations ranging from cloud resolving model to GCMs [*Kuang and Hartmann*, 2007; *Zelinka and Hartmann*, 2010]. Using the radiative kernel approach to efficiently compute cloud feedback from tens of GCMs archived for IPCC AR4, Zelinka *et al.* [2011] demonstrated a wider spread of longwave and shortwave feedbacks induced by high clouds than those induced by low clouds. Thus, there are still pressing needs to understand feedbacks involved with ice clouds, especially the cloud fraction and ice cloud microphysics properties. Of particular interest is the grid-averaged ice water path (IWP), the integral of in-cloud ice water content weighted by the cloud fraction (i.e. grid-averaged ice water content, IWC) over vertical layers. Even taking the careful comparison into account, large discrepancies still exist among the simulated and observed climatology of tropical IWP and IWC: The inter-model discrepancies of IWP (IWC) in the WCRP CMIP3 (Coupled Model Intercomparison Project, Phase 3) multi-model dataset can be as large as a factor of 10 [*Waliser et al.*, 2009]. On the other hand, in terms of simulating feedbacks in future climate, the natural fluctuation around the climatological mean state is also important because it can be related to the long-term changes in response to the anthropogenic perturbation of greenhouse gases, as articulated from theoretical perspectives [*Leith*, 1975; *North et al.*, 1993] as well as shown in a previous feedback study [*Hall and Qu*, 2006]. Simply put, how a system dissipates the external perturbation is related to how the system

fluctuates in the absence of such external perturbation. It is from this perspective that this study explores the issue of IWP interannual anomalies and the linkage to simulated future climate changes.

In this chapter, we use MLS and MODIS observations together with dynamic fields from ECMWF ERA-interim reanalysis to characterize the relationship among the interannual anomalies of IWC/IWP, temperature, and 500hPa vertical velocity (hereafter, ω_{500}) over the tropical Pacific basin (For brevity, anomaly or a subscript $_a$ is used hereafter to refer to the interannual anomaly). Given the recent advance in reanalysis, we carry out a parallel analysis using the latest ECMWF interim reanalysis (hereafter, ERA-interim) as well as a large collection of GCM simulations archived for both CMIP3 and CMIP5 datasets. CMIP5 datasets are used for the ongoing the fifth IPCC report as well. Then we explore the relations of IWC/IWP anomalies vs. ω_{500} anomaly between current climate and future climate. Furthermore, using GFDL GCM, we estimate the ice cloud feedback associated with the relation inferred from such study. The datasets and methodology are described in Section 4.2. The results and the implication are shown in Section 4.3. Section 4.4 gives the conclusion.

4.2 Data and Methods

MLS Version 3.3 Level 2 products of IWC and temperature at 215 hPa are used. The IWC is retrieved from cloud-induced radiance at the MLS 240-GHz window channel with a typical precision of 1.2-2.1 mg/m^3 and detectable range of 0.6 to 50 mg/m^3 at 215 hPa [*Livesey et al.*, 2011]. As done in *Su et al.* [2006], such Level 2 products were screened with quality control and then used to generate monthly mean products over 4° latitude by 8° longitude grids over six years (from September 2004 to August 2010).

MODIS monthly Level-3 IWP data [*King et al.*, 2003] is collected from Aqua platform (MCD08) and weighted by the monthly ice cloud fraction to get the grid-averaged IWP as done in *Waliser et al*. [2009].

We analyze monthly mean data from the ERA-interim reanalysis over the same period in parallel. ERA-interim is the latest reanalysis product from ECMWF with improved model physics and a new humidity analysis algorithm [*Simmons et al.,* 2007; *Uppala et al.*, 2008]. The improvement in humidity anomalies with respect to ERA-40 has been shown in *Chuang et al.* [2010]. IWC at its native 225 hPa level is used for comparison with MLS IWC at 215 hPa. ERA-interim monthly ω_{500} fields are used in composite analysis for both MLS and ERA-interim IWCs. The integrated IWP is used for comparison with GCM counterparts.

For GCMs, 6 GCMs from recently available CMIP5 multi-model dataset, and 14 GCMs from the CMIP3 dataset are used. Since IWC was not archived in these GCM outputs, we can only use the IWP instead. Accordingly, we use simulated layer-mean temperature (250-400 hPa) instead of temperature at any particular level. Appendix at the end of this Chapter summarizes the basic information about the GCMs used in this study. Two periods are used in this chapter: the last thirty years (1970-1999) of outputs from the 20th century and those from the 21st century (2070-2099) projection. For CMIP5 GCMs, the historical run is examined as the 20th century simulation and the RCP4.5 scenario [*Clarke et al.*, 2007] is for the 21st century projection. For CMIP3 GCMs, the 20c3m run is for the 20th century and SRES A1B scenario [*Solomon et al.,* 2007] is for the 21st century simulation. Both RCP4.5 and SRES A1B scenarios are based on projections of moderate emissions in the future.

The interannual anomaly at each gridbox is constructed by removing the linear trend and mean seasonal cycle from the original time series, then low-pass filtering with a 13-month moving average as in *Huang et al.* [2005] and *Chuang et al*. [2010]. The statistical significance and 95% confidence interval are computed with a degree of freedom estimated from the autocorrelation at time lag one [*Bretherton et al*., 1999].

The cloud radiative effect and feedback calculation are performed using the GFDL simulations and its off-line radiation code. The change of radiative effect in the future climate is calculated by perturbing one year of 3-hourly GFDL simulation output with 14.6% extra ice water path everywhere and computing the differences of radiant fluxes at both the top of atmosphere (TOA) and the surface. The standard deviation is estimated from twelve monthly-mean differences and the mean is estimated from the annual differences.

4.3 Results

4.3.1 Interannual variability in the current climate

Figure 4.1a shows the correlation coefficient between the MLS 215 hPa temperature and IWC anomalies over each grid box in the tropical Pacific basin. In parallel, Figure 4.1b shows correlation map between the MLS 215 hPa temperature anomalies and ERA-interim ω_{500} anomalies. The resemblance of the two plots is self evident: grid boxes with negative correlations between temperature and ω_{500} anomalies tend to have positive correlation between IWC and temperature anomalies, and vice versa. Bearing in mind that ENSO is the dominant interannual variability in the tropics, we formulate a composite of deviations of January ω_{500} fields in El Niño years with respect to January climatology. Zero contour lines of such El Niño composite are shown in the figures (the

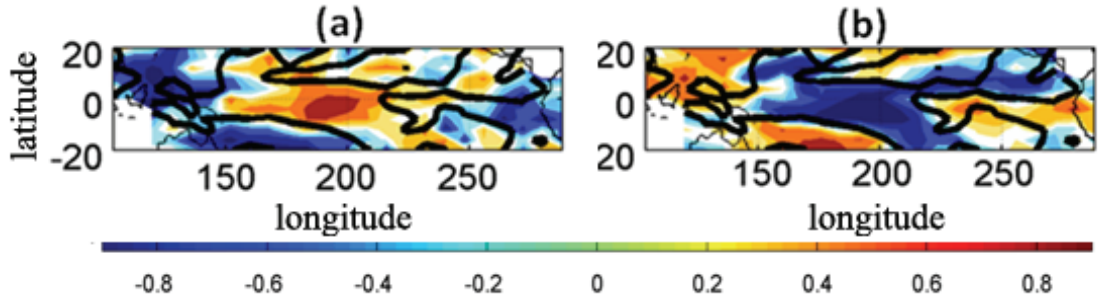

Figure 4.1. The correlation coefficient map over the tropical Pacific region between (a) 215hPa interannual anomalies of temperature and those of IWC for MLS and (b) 215hPa interannual anomalies of temperature for MLS and those of 500hPa vertical velocity (ω_{500a}) for ERA-interim. The black curves are the zero contour lines of January ω_{500} composite of El Niño years within MLS period (i.e. deviation of Januaries of 2005, 2007 and 2010 from the January climatology).

black thick lines). Inside the zero contour lines, the ω_{500} composite is negative due to the shift of ascending branch of the Walker circulation to the tropical central-eastern Pacific in the El Niño years. As expected, such zero lines largely overlap with the transition from negative to positive correlations between temperature and ERA-interim ω_{500} anomalies. The negative correlation indicates that the SST-driven upward motion is associated with anomalous warming in the UT, largely due to the latent heat release from enhanced convection. On the contrary, positive correlation indicates that forced descent anomaly is collocated with warm temperature anomalies related to the wave propagation emanating from anomalous heat source [*Gill*, 1980]. Such resemblance between two correlation maps can be found in ERA-interim reanalysis and all the GCMs we examine, especially within the ascending regions for ENSO composite, which is clearly shown in Figure 4.a.1 for ERA-interim and all CMIP5 GCMs analyzed here.

The resemblances of correlation maps in Figure 4.1 motivate us to examine the composite of IWC anomalies with respect to ω_{500} anomalies. *Su et al.* [2008b] and *Su et al.* [2011] examined such relation between IWC and ω_{500} raw data and showed a

dichotomy relation: IWC correlates negatively with ω_{500} when ω_{500} is negative (i.e., the stronger the upward motion, the larger the IWC) and is essentially flat when ω_{500} is positive (little ice clouds in the subsidence region). Such relations are repeatedly shown in our analysis (Figures 4.2a). A similar dichotomy relation is shown in the observed mean seasonal cycles as well (Figure 4.2b). On the other hand, when the IWC and ω_{500} interannual anomalies are examined in the same way (Figure 4.2c), a linear dependence emerges for all ω_{500} anomalies. As shown in Figures 4.2d-f, similar results are found for the MODIS IWP. In addition, such linear relation between IWP and ω_{500} anomalies can be seen in all GCM composites and ERA-interim reanalysis, as shown in Figure 4.3.

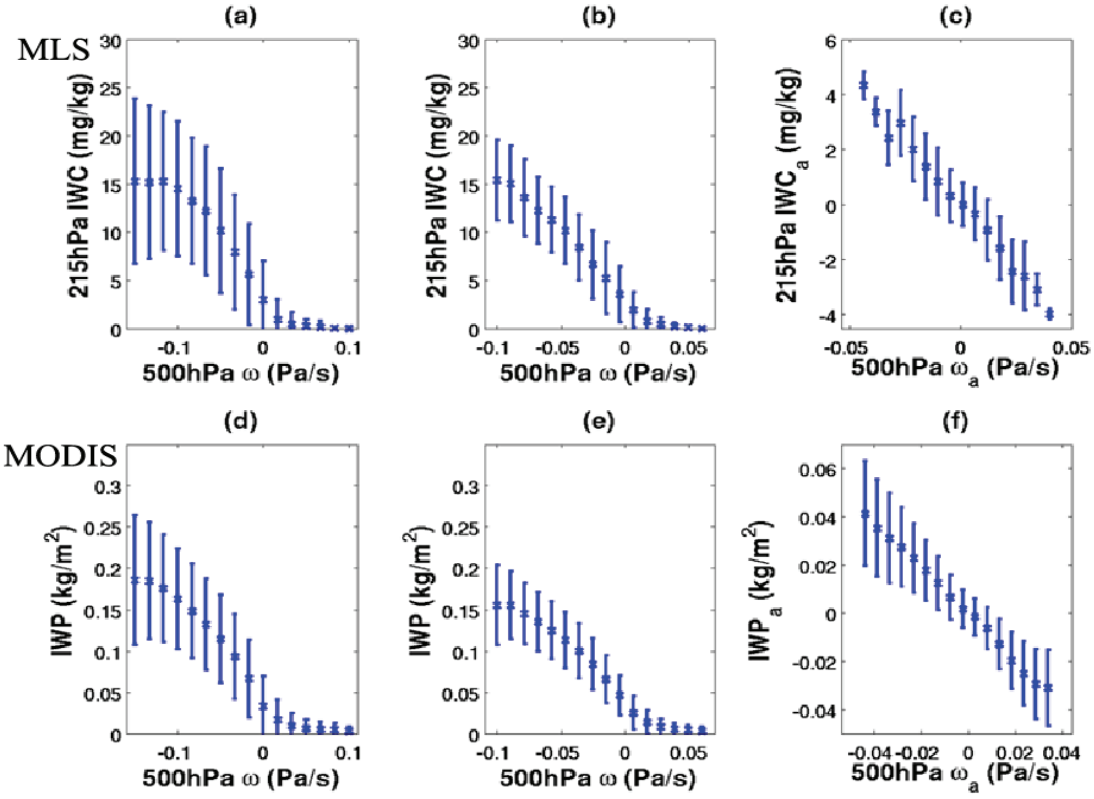

Figure 4.2. Upper panels: the composite of MLS ice water content (IWC) at 215 hPa with respect to the ERA-interim vertical velocity at 500 hPa. (a) The composite of all monthly-mean data from Sep 2004 to Aug 2010. (b) is based on mean seasonal cycles of MLS IWC at 215 hPa and ω_{500}. (c) is based on interannual anomalies of MLS IWC at 215 hPa and ω_{500}. (d-e) Same as (a-c), respectively, except for the Aqua MODIS IWP from Jan 2003 to Dec 2010.

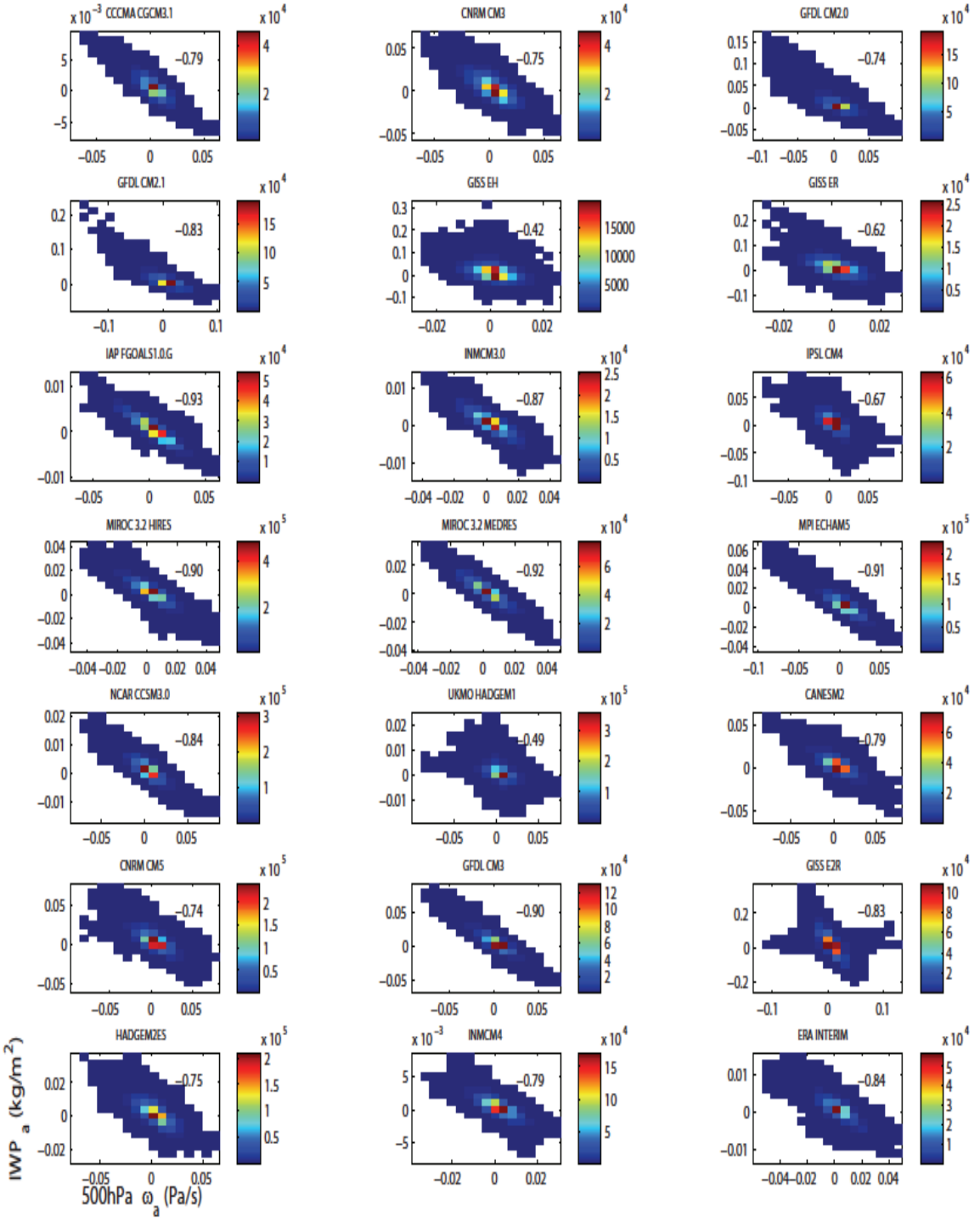

Figure 4.3. Joint histograms of the interannual anomalies of IWP (IWP_a) and the interannual anomalies of 500hPa vertical velocity (ω_{500a}) as simulated by 20 climate models for the current climate (the 20th-century all forcing runs) and as assimilated by ERA-interim. The plots are based on anomalies in the grid boxes over the tropical Pacific Ocean. The number on each panel indicates the correlation coefficient IWP_a and ω_{500a}.

Figures 4.2 and 4.3 indicate that the linear relation between IWP (IWC) anomaly and ω_{500} anomaly is robust across a wide range of observation data sets and GCM simulations. An interesting question to ask then is physically why such linear relations (or negative correlations) between two quantities can be expected at the interannual timescale. Our explanation is twofold:

(1) As indicated in Figure 4.1, the ascending branch of Pacific Walker circulation, which is featured with frequent convection, shifts at the interannual timescale. Normally the ascending branch is centered at western Pacific and Maritime continents (Pacific warm pool). But during El Niño phase, the ascending branch is shifted to the central Pacific (i.e. ω_{500} is more negative in the central Pacific than usual and opposite is true in the warm pool region). Accordingly, deep convection activities are suppressed in the warm pool region and enhanced in the central Pacific. In turn, less clouds (convective clouds and anvil clouds from deep convection) than normal can be expected in the warm pool region and more clouds associated with deep convection can be expected in the central Pacific. Opposite situation can be expected during the La Nina phase. This leads to a negative correlation between IWP anomalies and ω_{500} anomalies.

(2) For the regions where ω_{500} anomaly and temperature anomaly is positively correlated (Figure 4.1a), during El Niño phase, the ω_{500} is less negative (or more positive) and temperature anomaly is positive. A warmer temperature is less favored for in-situ formation of clouds and more favored for the evaporation (dissipation) of clouds. The net effect would favor less in-situ ice clouds than the mean state. Therefore, this leads to a negative correlation between ice cloud path anomaly and ω_{500} anomaly as well. For the regions where ω_{500} anomaly and temperature anomaly is negatively correlated, normally

few in-situ ice clouds are presented (this is also the region sometimes referred as "ocean desert"). Therefore, change of deep convection activity is the major reason for cloud variability at the interannual time scale.

Both (1) and (2) lead to the negative correlation between IWC/IWP and ω_{500} anomalies. Since the interannual anomaly is only a small fraction of the mean value for both quantities, their relations therefore tends to be linear instead of non-linear.

The fractional change of IWP_a (IWC_a) with respect to ω_{500a} is calculated by the linear regression of IWP_a (IWC_a) onto ω_{500a} normalized then by the mean IWP (IWC) averaged over the tropical Pacific basin (i.e., $\frac{1}{\overline{IWC}}\frac{dIWC_a}{d\omega_{500a}}$ or $\frac{1}{\overline{IWP}}\frac{dIWP_a}{d\omega_{500a}}$), as shown in Table 4.1. In spite of the large discrepancies in the mean IWP (IWC) values, Table 4.1 shows that **the IWP fractional change with respect to ω_{500a} is much more consistent among all data sets examined here than the simulated mean states of IWP.** MLS IWC_a changes about 18% for per -0.01 Pa/s variation in ω_{500a}, and similar fractional change is inferred from MODIS IWP_a. The fractional change from all GCMs and ERA-interim reanalysis is 21.6±5.2% (mean±standard deviation) per -0.01Pa/s variations in ω_{500a}. The ratio of maximum to minimum fractional change among all GCMs is only ~2. Moreover, the fraction of variance explained by such linear relation is also consistent among GCMs and ERA-interim reanalysis, with a mean of 62.3% and a standard deviation of 19.0%. Such linear relation explains less fraction of variance in the MLS and MODIS observations, presumably due to the noisy nature of observations. Nevertheless, the linear relation still explains 30.3-48.3% of total variance. These relations imply the interannual variations of large-scale tropical circulation driven by the ENSO cycle [*Battisti and*

Data Source	$\overline{IWC}$ (mg/kg)	$\frac{1}{\overline{IWC}}\frac{dIWC_a}{d\omega_{500a}}$ (% per 0.01Pa/s)	Explained fraction of variance
MLS at 215 hPa	4.69	-18.20 ± 2.29	30.33%
ERA-interim at 225 hPa	3.77	-19.19 ± 0.39	65.66%
	$\overline{IWP}$ (kg/m^2)	$\frac{1}{\overline{IWP}}\frac{dIWP_a}{d\omega_{500a}}$ (% per 0.01Pa/s)	
ERA-interim	1.00×10^{-2}	-22.64 ± 0.37	70.32%
MODIS	6.01×10^{-2}	-17.74 ± 0.25	48.31%
CMIP3 GCMs			
UKMO HADGEM1	0.77×10^{-2}	-15.13 ± 0.28	23.94%
CCCMA CGCM3.1	0.81×10^{-2}	-14.84 ± 0.30	62.85%
IAP FGOALS1.0G	1.01×10^{-2}	-16.34 ± 0.18	86.94%
INMCM3.0	1.21×10^{-2}	-20.19 ± 0.38	75.37%
NCAR CCSM3.0	1.37×10^{-2}	-15.25 ± 0.11	70.53%
GFDL CM2.0	1.85×10^{-2}	-32.05 ± 0.51	55.07%
GFDL CM2.1	1.93×10^{-2}	-27.80 ± 0.38	68.30%
MPI ECHAM5	2.64×10^{-2}	-19.82 ± 0.15	82.34%
MIROC3.2 MEDRES	3.16×10^{-2}	-22.85 ± 0.21	85.46%
MIROC3.2 HIRES	3.22×10^{-2}	-22.06 ± 0.09	80.22%
CNRM CM3	3.48×10^{-2}	-19.54 ± 0.37	56.20%
IPSL CM4	$5.43\times.10^{-2}$	-17.45 ± 0.47	45.15%
GISS EH	7.22×10^{-2}	-26.89 ± 1.62	17.89%
GISS ER	9.29×10^{-2}	-27.95 ± 0.96	38.37%
CMIP5 GCMs			
INMCM4	0.45×10^{-2}	-31.48 ± 0.32	61.85%
UKMO HADGEM2 ES	1.96×10^{-2}	-17.92 ± 0.18	56.13%
CAN ESM2	2.39×10^{-2}	-21.21 ± 0.45	62.66%
CNRM CM5	3.17×10^{-2}	-17.88 ± 0.16	54.64%
GFDL CM3	12.75×10^{-2}	-24.76 ± 0.21	84.85%
GISS E2R	18.07×10^{-2}	-19.94 ± 0.24	68.17%

Table 4.1. Mean ice water content (or ice water path) from each data source over the Tropical Pacific. Regressed fractional change of interannual anomalies of IWC(IWP) with interannual anomaleis of ω_{500}. The fraction of variance explained by such regression. Note that the ERA-interim ω is used to compute the regression to ω for MLS and MODIS.

Sarachik, 1995] account for majority of the year-to-year variations of tropical IWP/IWC. The results also indicate that the models simulate the fractional variation of IWP/IWC with respect to large-scale dynamics better than the mean climatology of IWP/IWC.

4.3.2 The long-term change between the 20th and 21st centuries

Motivated by studies seeking connections between simulated variations in current climate and simulated secular changes due to the increases of greenhouse gases (e.g., *Qu and Hall* [2006], *Hall and Qu* [2006] and *Knutti et al.* [2006]) and aforementioned theoretical consideration about dissipation and fluctuation behaviors of a system, we look the simulated long-term changes of IWP/IWC and the vertical velocity and explore whether any relations exist between such secular change and interannual variation of the same GCM. Using the CMIP3 simulations for the IPCC AR4 A1B scenario and the CMIP5 simulations for the RCP4.5 scenario in the forthcoming IPCC AR5, we calculate the long-term change of IWP (ΔIWP) for each gridbox by subtracting the averages of 1970-1999 from those of 2070-2099. $\Delta\omega_{500}$ is then calculated in the same way. Figure 4.4 shows the joint histogram of ΔIWP and $\Delta\omega_{500}$. A linear regression of ΔIWP with respect to $\Delta\omega_{500}$ is used to derive the long-term change (hereafter, $\Delta IWP/\Delta\omega_{500}$), which explains 44.9±22.6% of total variance of ΔIWP over the tropical Pacific Ocean.

We find an interesting relationship between $\Delta IWP/\Delta\omega_{500}$ and the current-climate $dIWP_a/d\omega_{500a}$ simulated by the climate models, as shown in Figure 4.5a. For models with large $dIWP_a/d\omega_{500a}$ in the present climate, its $\Delta IWP/\Delta\omega_{500}$ for the future climate tends to be large too. For all 19 models that provided simulations of future climate projections, the

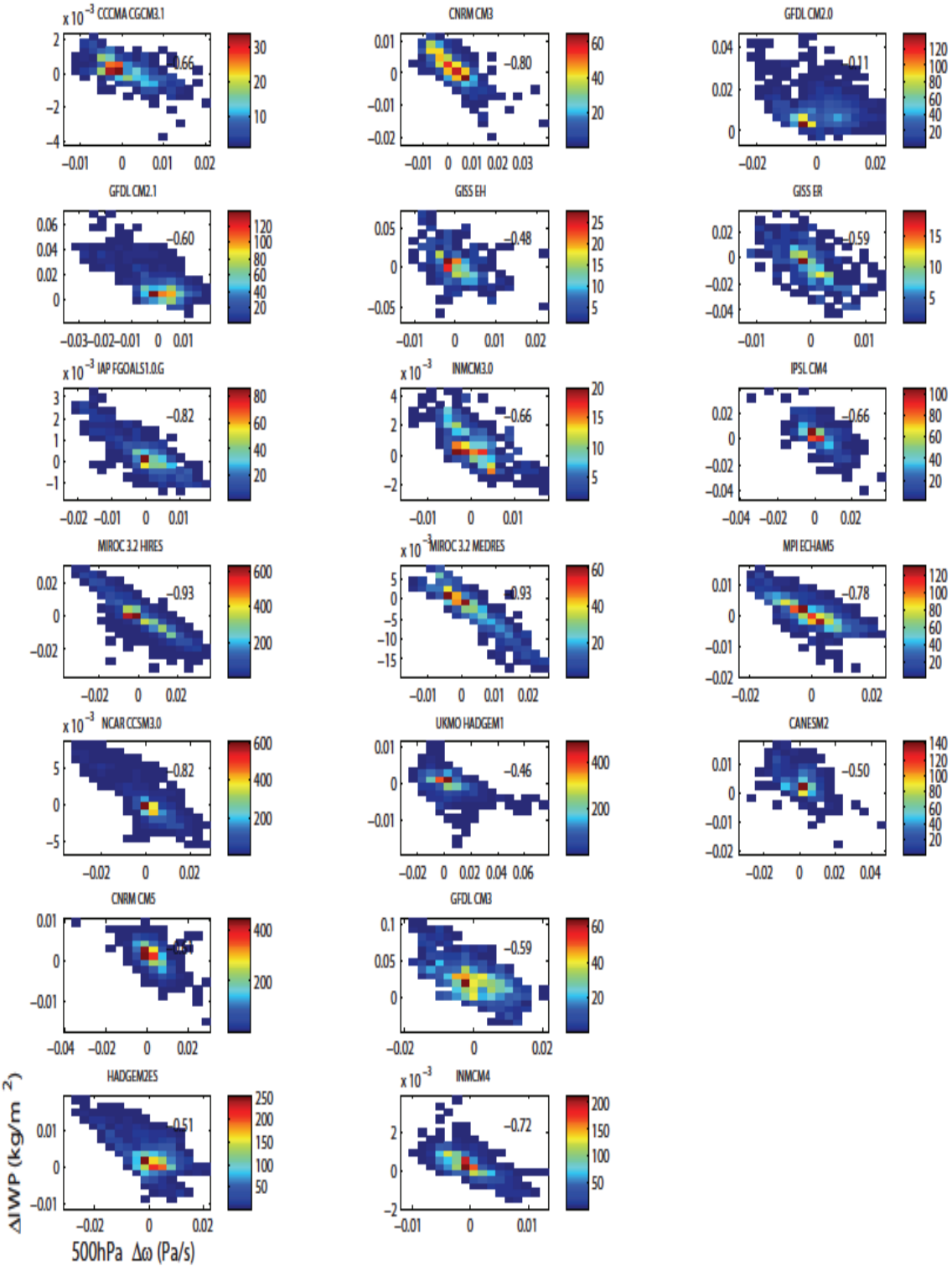

Figure 4.4. Joint histograms of long-term change of IWP (ΔIWP) and the long-term change of 500hPa vertical velocity (500hPa Δω) over the tropical Pacific ocean as simulated by each GCM. The number on each panel indicates the correlation coefficient between two long-term changes.

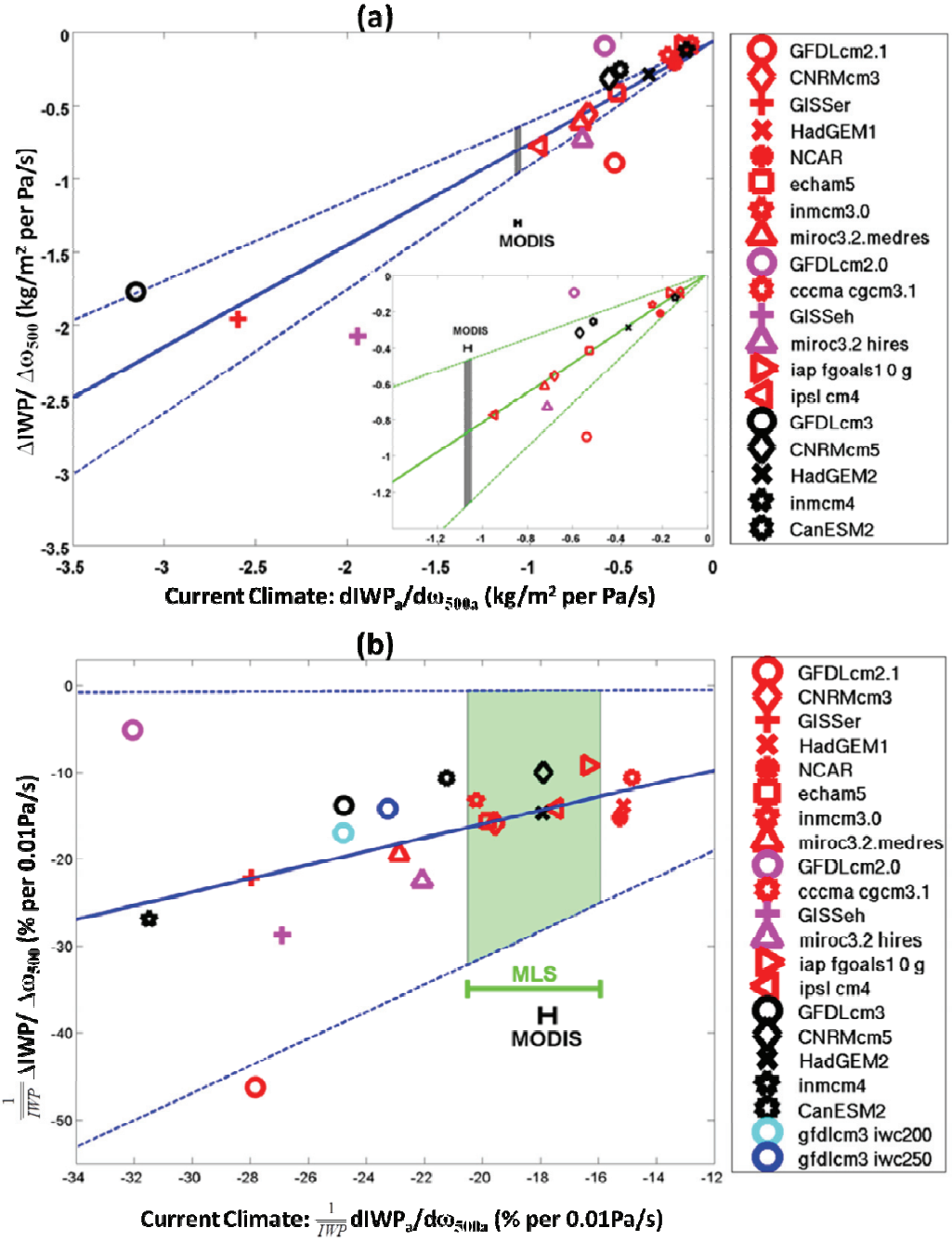

Figure 4.5. (a) The scatter plot of $\Delta IWP/\ \Delta\omega_{500}$ (long-term change of IWP with respect to long-term change of ω_{500} between future climate and current climate simulations) vs. $dIWP_a/d\omega_{500a}$ of current climate as simulated by each GCM. The CMIP3 models are in red and the CMIP5 models in black. The regression slope and 95% confidence intervals are shown as blue solid line and dashed lines, respectively. The MODIS $dIWP_a/d\omega_{500a}$ and projected range of $\Delta IWP/\ \Delta\omega_{500}$ are shown as gray trapezoid intercepted with the 95% confidence intervals of the regressed slope. (b) Similar as (a) except for the relative changes instead of absolute changes. The relative variation of MLS IWC_a with respect to ω_{500a} is shown as green ticked lines and that of MODIS IWP_a shown as a black ticked line. The projected fractional change based on MLS result is shown as a green trapezoid.

resulting regression is

$$\Delta IWP/\Delta\omega_{500} = 0.69\ dIWP_a/d\omega_{500a} - 0.064 \quad (4.1)$$

The 95% confidence interval is [0.54, 0.85] for the slope and [-0.24, 0.11] for the intercept. The positive correlation and statistically significant slope are not dominated by three models (GISS ER, GISS EH, and GFDL CM3) which are outliers from the cluster of remaining models shown in Figure 4.5a. Removing the three models (zoom-in plot in Figure 4.5a), the regressed slope is still 0.83 with a 95% confidence interval of [0.45, 1.20], overlapping with the aforementioned confidence interval for the slope.

Eq. 4.1 indicates a relation between the natural fluctuation (at interannual time scale) and secular change of IWP with respect to the large-scale circulation. By examining the ensemble behaviors of CMIP3 GCMs, *Vecchi and Soden* [2007] showed that simulated changes in the circulation over the tropical Pacific Ocean tend to resemble "El Niño-like" conditions when climate warms. The left panels of Figure 4.6 show the deviation of ω_{500} in the El Niño years from its climatology in the 20th century from five CMIP5 GCMs and the right panels of Figure 4.6 show the change of ω_{500} between the two centuries. Within the equatorial Pacific belt (~10°S-10°N), the similarity between the two panels also leads to similar conclusion about the resemblance of patterns of long-term change and patterns of interannual variability. Phenomenologically, this explains why a relation like the one shown in Figure 4.5a can be expected. Note the relation hence can provide us an opportunity to estimate future change of IWP, an important property of ice clouds, based on current multi years of observations of IWP. For example, the regression in Eq. 4.1 and the $dIWP_a/d\omega_{500a}$ derived from MODIS observations would project a 7.9 to 8.2 g m^{-2} increase of IWP for every -0.01 Pa/s change in future ω_{500} over the tropical Pacific ocean.

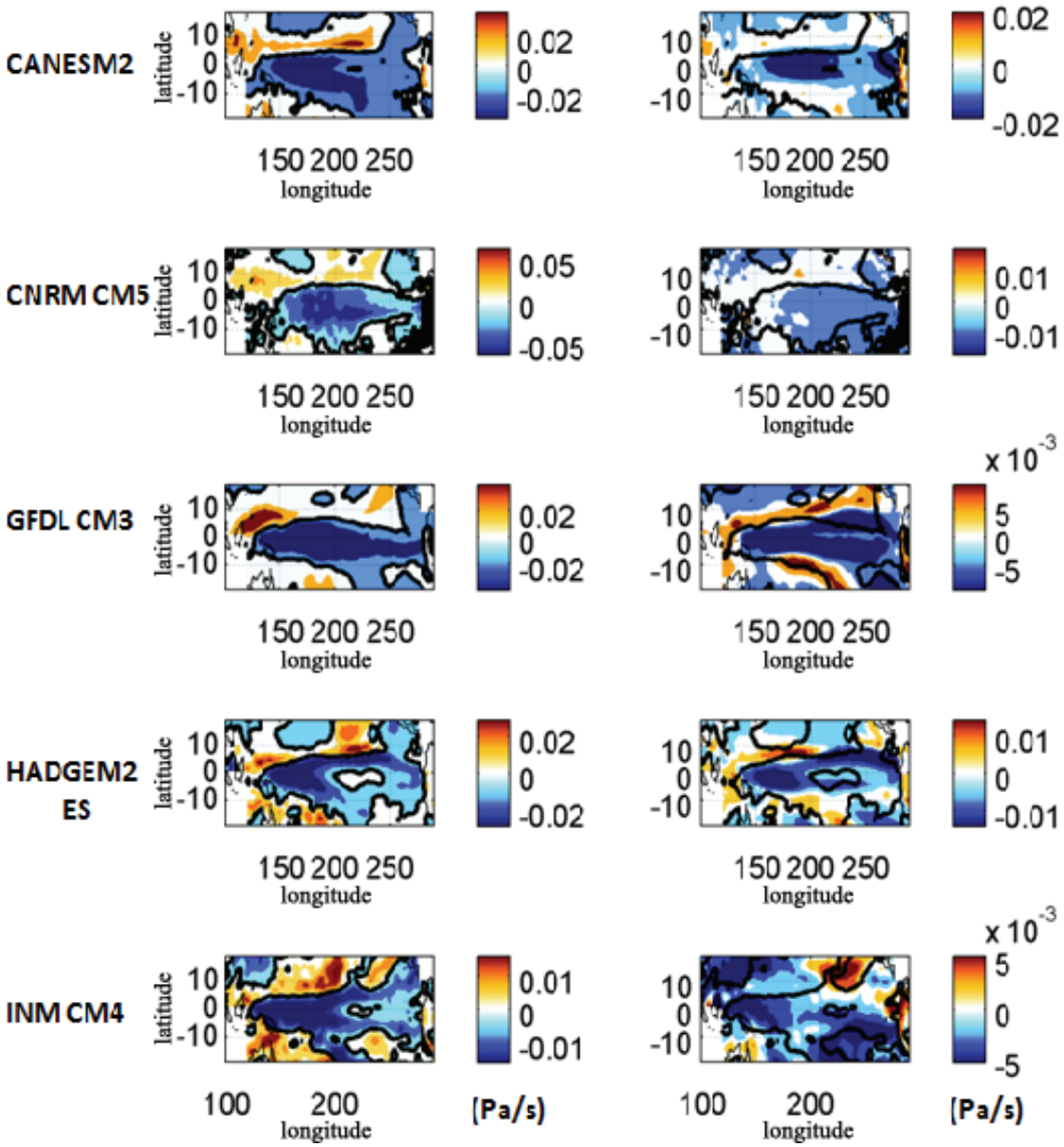

Figure 4.6. The left panel shows the deviation of ω_{500} in the El Niño years from its climatology in the 20th century of each GCM over the tropical Pacific. The right panel shows the long-term change of vertical velocity at 500 hPa ($\Delta\omega_{500}$) of each GCM.

Figure 4.5b shows a similar correlation exists in the current-climate fractional variations of IWP_a/IWC_a with respect to ω_{500a} and the long-term fractional change of IWP or IWC with respect to ω_{500} (as normalized by the mean IWP or IWC in the current climate). A linear regression using all models shown in Figure 4.5b yields

$$\frac{1}{\overline{IWP}}\frac{\Delta IWP}{\Delta\omega_{500}} = 0.78\frac{1}{\overline{IWP}}\frac{dIWP_a}{d\omega_{500a}} - 0.36 \qquad (4.2)$$

with 95% confidence interval being [0.012, 1.55] for the slope and [-17.53, 16.80] for the intercept. The large confidence intervals here are due to the large spread of mean IWP among climate models (Table 4.1) in the denominators of both predictor and target variable. Nevertheless, the slope is still statistically significant. Though the IWC is not available in the CMIP3 and CMIP5 archives, the IWC from GFDL CM3 model [*Donner et al.*, 2011] is available to us and can be plotted onto such fractional change chart together with IWP changes. Figure 4.5b shows that the fractional changes of IWCs at both 200 hPa and 250 hPa in the GFDL CM3 are very close to the fractional changes of IWP in the same model, for both the present climate variations and projected future change. Note the 95% confidence interval of observed fractional variations of MLS IWC_a at 215 hPa also overlaps with the confidence interval of fractional variations of MODIS IWP_a. Using Eq. 4.2 as a constraint, the MLS and MODIS results imply a 12.8-16.4% change in IWP (IWC) for per -0.01 Pa/s change of ω_{500a} in future climate, with 95% confidence interval forming the green trapezoid in Figure 4.5b and the long diagonal bracketing 0.6% to 32.2%. Using the ensemble mean of 22 CMIP3 GCMs, *Vecchi and Soden* [2007] suggested a weakening of vertical velocity ~2 hPa/day K^{-1} global warming at both the ascending and descending branches of Walker circulation over the tropical Pacific (Figure 4.7a, adopted from Figure 7b of *Vecchi and Soden*, [2007]). We do a similar ensemble calculation for the five CMIP5 GCMs which provides simulations of future climate projections. Figure 4.7b shows the ensemble mean ω_{500} change over the

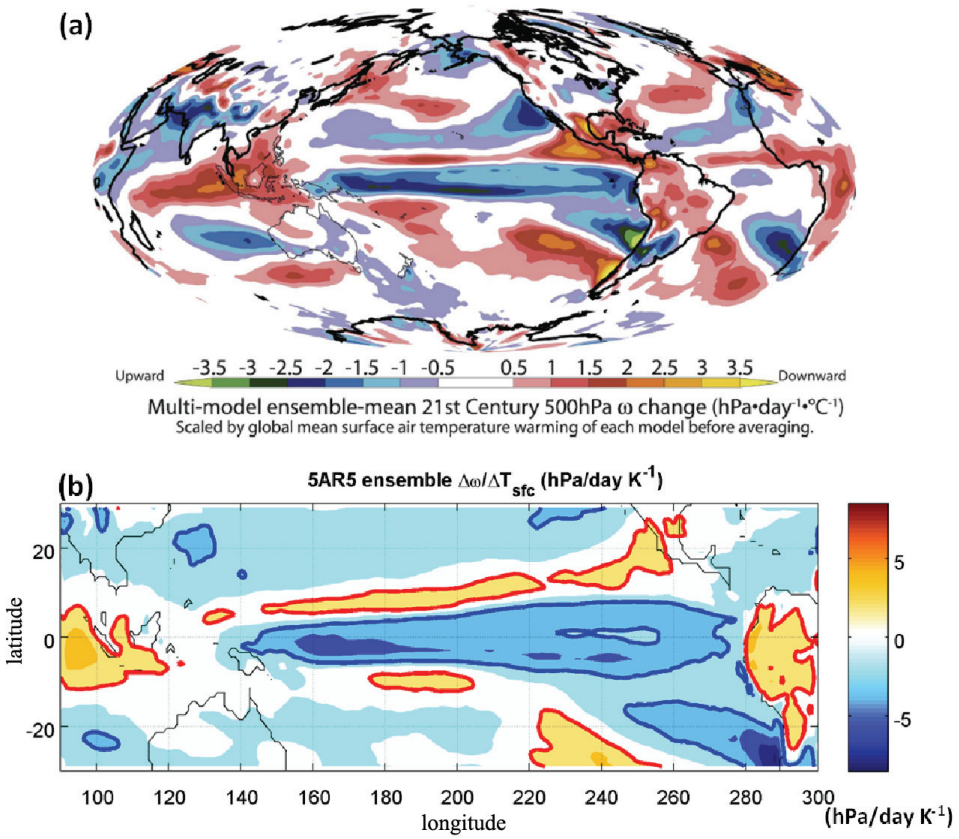

Figure 4.7. (a) Adopted from the figure 7 of *Vecchi and Soden* [2007]. The ensemble mean of the change of ω500 per 1K global warming from 22 CMIP3 GCMs. (b) Similar to (a), but for the ensemble mean of the five CMIP5 GCMs (GFDL CM3, CNRM CM5, HAD GEM2, INM CM4, and CANESM2) over the tropical Pacific. Changes of 2 hPa/day K^{-1} and -2 hPa/day K^{-1} are contoured in red and blue, respectively.

tropical Pacific scaled by the global surface temperature change. The result from these five CMIP5 GCMs is similar to that from CMIP3 GCMs. Figure 4.8 shows the histograms of the ω_{500} change over the tropical Pacific. The mean value of these 19 GCMs from both CMIP3 and CMIP5 is 1.36 hPa/day K^{-1} and -1.31 hPa/day K^{-1} for descending and ascending branch, respectively. If we use the weakening circulation of 2 hPa/day K^{-1}, then the MLS and MODIS results here would imply a ~ 2.96%-3.80% decrease of IWP in tropical Pacific for such circulation change with per 1K global warming.

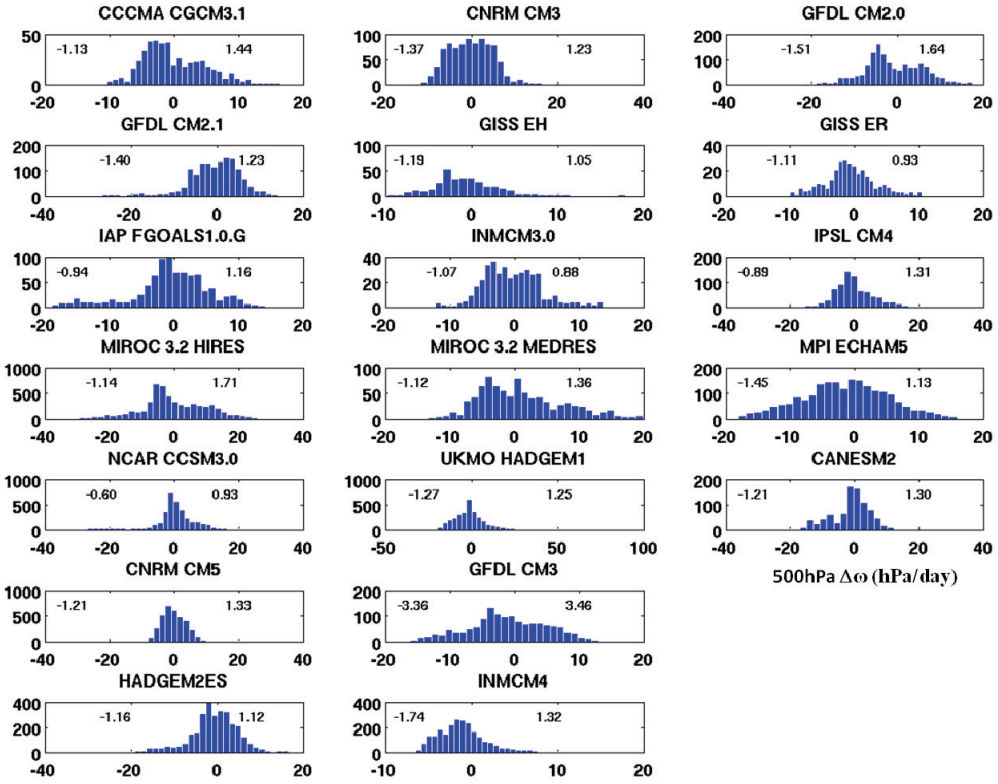

Figure 4. 8. The histograms of the ω_{500} change over the tropical Pacific for the 19 GCMs provided simulation of future climate projection. The upper-left value shows the mean change of ω_{500} in the ascending branch scaled by the global surface temperature warming. The upper-right value shows the mean change of ω_{500} in the descending branch scaled by the global surface temperature warming.

4.3.3 Cloud radiative effects

The above analysis allows us to further estimate the change of radiative effect of ice clouds associated with the circulation change in the future climate. Such forcing calculations are performed using the GFDL simulations and its off-line radiation code. Figure 4.9 shows the change of net cloud radiative effect as a result of a 14.6% increase of IWP at the TOA and the surface[1]. When IWP increases, it reduces the amount of

[1] Please note the calculation was carried out for a positive change of IWP. In the global warming scenario, the IWP change due to circulational change is negative, as we articulated in the previous section.

longwave radiation escaping to the space and increases the amount of reflected sunlight, leading to only a small change in the TOA net cloud radiative effect. For the median value of the IWP change (14.6% per -0.01Pa/s) showed in Figure 4.5b, the averaged change of cloud radiative effect at TOA is slightly positive at 0.23±0.03 Wm^{-2} over the tropical Pacific. The maximum changes of cloud radiative effect are found along the intertropical convergence zone and the southern Pacific convergence zone. At the surface, due to abundant downward emissions in the lower part of the troposphere, the longwave radiative effect of high clouds is much smaller compared to its shortwave effect. As a result, the shortwave effect dominates and a 14.6% increase of IWP reduces surface cloud radiative effect by 1.38±0.12 Wm^{-2}. For a decrease of ω_{500} ~2 hPa/day K^{-1} global

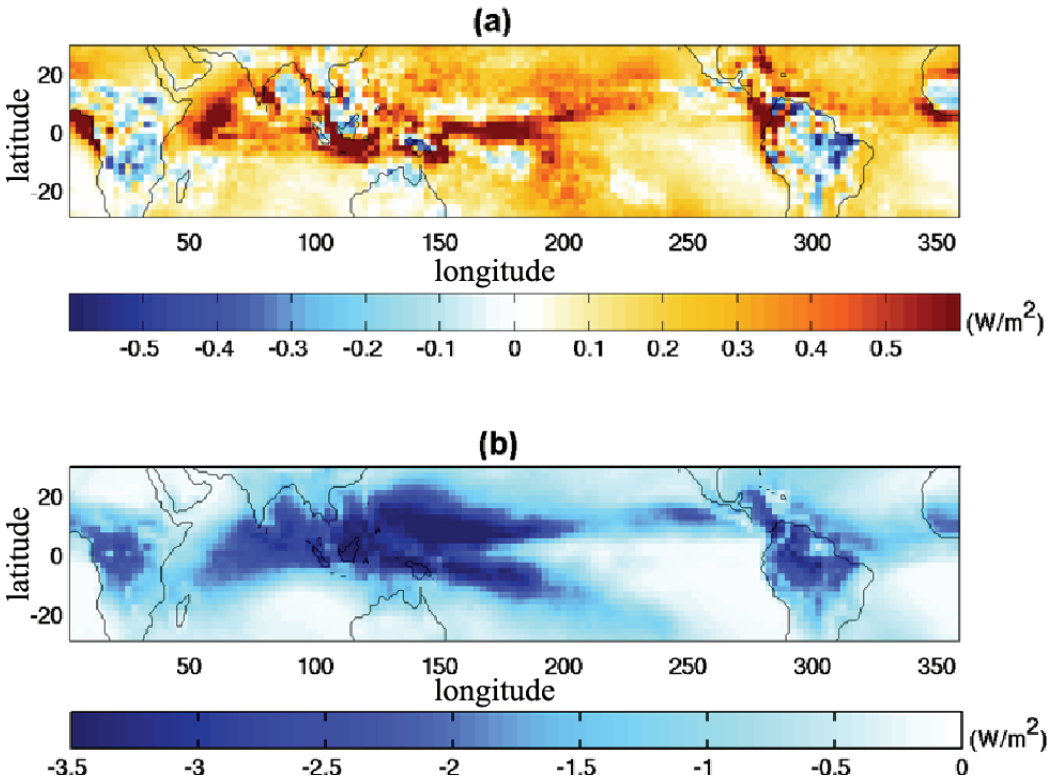

Figure 4.9. (a) The change of net cloud radiative effect at the top of atmosphere as a result of a 14.6% increase of ice water path in the GFDL AM3 model. (b) The change of net cloud radiative effect at the surface as a result of a 14.6% increase of ice water path in the GFDL AM3 model.

warming, changes of cloud radiative effect at TOA and surface are ~-0.05±0.007 Wm^{-2} and ~0.32±0.03 Wm^{-2}, respectively. Such different changes at TOA and surface imply a net change of cloud absorption in the atmosphere by ~-0.37±0.037 Wm^{-2} over the tropical Pacific per 1K global warming. Given the close diagnostic relations between radiative flux divergence (i.e. radiative cooling) and the latent heating due to precipitation [*Ming et al*., 2010], such change of cloud absorption needs to be taken into account for studying the change of hydrological cycle. Moreover, the thermal stability and lapse rate can be affected by such change of cloud absorption as well. If only this contribution is considered, reduced cloud absorption of shortwave in the upper troposphere would lead to a decrease of upper-tropospheric temperature, which in turn increases the lapse rate and thermal instability of tropospheric atmosphere. Such environment would be favors for more frequent occurrence of convective events including tropical cyclones.

4.4 Conclusion and discussion

In this chapter, we examine the interannual variability of IWP, an important property of ice clouds, with respect to large-scale vertical velocity in observations, reanalysis and climate model simulations, and by relating the unforced variability to the human-influenced climate change. Here we show that a statistically significant linear relation between interannual anomalies of IWP and ω_{500} with similar values of slope can be identified from all data sets. Moreover, such relationship in each model is closely correlated with its simulated IWP change with respect to ω_{500} change for the future climate, suggesting a robust constraint for the future tropical ice cloud change associated with the large-scale circulation change.

Such constraint and observed IWP-ω_{500} relation projects a 12.8%-16.4% increase of IWP for every -0.01Pa/s change of ω_{500}, equivalent to ~2.96%-3.80% decrease of IWP for Walker circulation change associated with every 1K global surface warming. Such IWP change corresponds to a decrease of 0.05±0.007 Wm^{-2} at the TOA and an increase of ~0.32±0.03 Wm^{-2} at the surface for per 1K global warming over the tropical Pacific, both implying a decrease of net cloud absorption which needs to be considered for relevant studies such as the future change of hydrological cycle.

Using the state-of-the-art satellite observations and climate model simulations, this study provides an estimate of the change of ice cloud water path associated with future Walker circulation change. Though the cloud feedback associated with this change seems small due to compensating longwave and shortwave effect at the TOA, the change in the atmospheric absorption is not negligible and needs to be taken into account in relevant studies.

Though the radiative flux change at the TOA is small for the amount of IWP change we discussed here, the surface flux change is much larger (by a factor of ~5). Traditionally feedback analysis and study focus on the change of the TOA flux, since it is the net energy escaped to the space and it is straightforward to define the linear feedback from that perspective for a highly simplified climate system. Such focus of the TOA flux is sufficient if the only concern is the global mean surface temperature change. However, if the focus is beyond the mean surface temperature, a TOA-focused feedback study would have its limitation. For example, the change of hydrological cycle is more related to changes of surface energy balance instead of those of the TOA energy balance [*Pierrehumbert,* 2010]. Therefore, even just to understand how global-mean precipitation

changes in the future would need better knowledge about the change of energy balance at the surface (and the atmosphere). It is possible, if not very likely, that two models can have identical strength of cloud feedback at the TOA but different change of cloud radiative effect at the surface. Nowadays what people try to extract from GCM simulations is already much more beyond a single value about global-mean temperature, e.g., change of regional climate change patterns, precipitations, and even extreme events. These changes have immediate and important societal consequences but not merely related to the TOA flux change. More aspects of the energy balance need to be considered for a better depiction of the simulated climate changes and discrepancies among GCMs. Maybe it comes to a stage to re-evaluate the applicability of radiative feedback and to propose more suitable metrics for the climate change studies.

4.5 Acknowledgements

We are greatly indebted to Drs. H. Su and J. Jiang at NASA JPL for their help on understanding and processing MLS data and for their contributions to an early study on CMIP3 model and MLS data comparison. ECMWF reanalysis was obtained from the ECMWF data server and MLS and MODIS data from NASA DAAC services. GCM simulations were obtained from the WCRP CMIP3 and CMIP5 data archived at PCMDI, Lawrence Livermore National Laboratory. The calculation of ice cloud feedback with the GFDL model was carried out by Dr. Yi Ming at the GFDL.

4.6 Appendix

Model	Modeling Center
CMIP 3	
CCCMA CGCM3.1	Canadian Centre for Climate Modelling and Analysis, Canada
CNRM CM3	Center National de Recherches Meteorologiques, France
GFDL CM2.0	Geophysical Fluid Dynamics Laboratory, USA
GFDL CM2.1	Geophysical Fluid Dynamics Laboratory, USA
GISS EH	Goddard Institute for Space Studies, USA
GISS ER	Goddard Institute for Space Studies, USA
IAP FGOALS1.0.G	Institute for Atmospheric Physics, China
INM CM3.0	Institute for Numerical Mathematics, Russia
IPSL CM4	Institut Pierre Simon Laplace, France
MIROC 3.2 HIRES	Center for Climate System Research, Japan
MIROC 3.2 MEDRES	Center for Climate System Research, Japan
MPI ECHAM5	Max Planck Institute for Meteorology, Germany
NCAR CCSM3.0	National Center for Atmospheric Research, USA
UKMO HADGEM1	Met Office's Hadley Centre for Climate Prediction, UK
CMIP5	
CAN ESM2	Canadian Centre for Climate Modelling and Analysis, Canada
CNRM CM5	Center National de Recherches Meteorologiques, France
GFDL CM3	Geophysical Fluid Dynamics Laboratory, USA
GISS E2R	Goddard Institute for Space Studies, USA
HadGEM2 ES	Met Office's Hadley Centre for Climate Prediction, UK
INM CM4	Institute for Numerical Mathematics, Russia

Table 4.a.1. A list of PCMDI CMIP3 and CMIP5 GCMs used in this chapter.

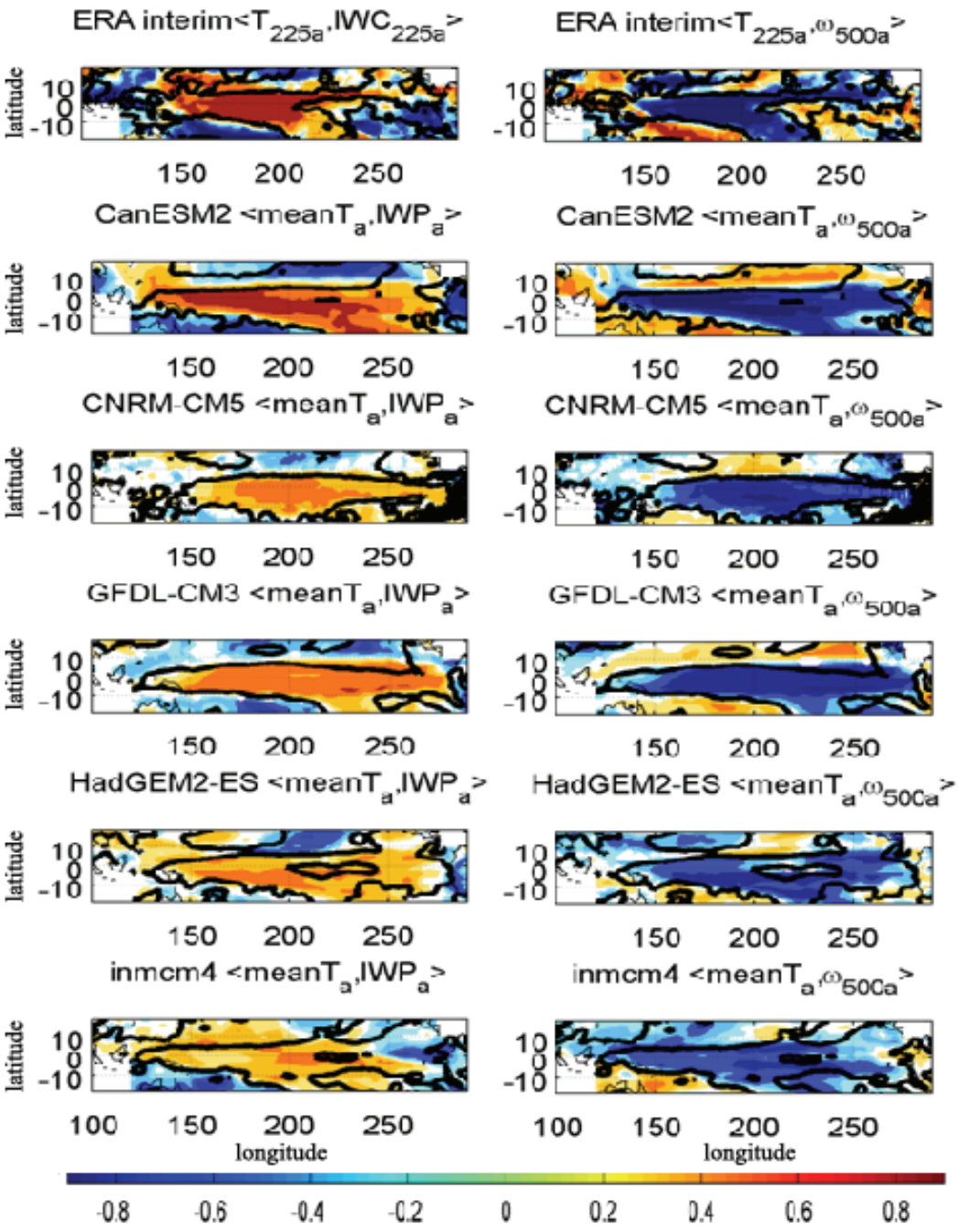

Figure 4.a.1. Similar to Figure 4.1, but for ERA-interim and five GCMs from CMIP5.

Chapter 5

The effect of changes of clear-sky radiative cooling on the weakening of tropical circulation in future global warming: a heuristic explanation

5.1 Introduction and motivation

Chapter 4 mentions the weakening of Walker circulation when we try to estimate the ice-cloud feedback associated with such change of tropical circulation. In the 1990s, there had been debates about how atmospheric circulation could change in a warmer climate. While many modeling studies have shown a weakening of the circulation (both zonal and meridional circulations) [*Betts and Ridgeway*, 1989; *Knutson and Manabe*, 1995; *Mitas and Clement*, 2006], the reanalysis products showed a strengthened Hadley circulation [*Tanaka et al*., 2004; *Quan et al*., 2004; *Mitas and Clement*, 2005]. In addition, a decadal trend in outgoing longwave radiation (OLR) that has been observed by ERBE satellites can be explained by postulating a strengthened tropical circulation in response to global warming [*Chen et al.*, 2002; *Wielicki et al.*, 2002]. However, later it was shown that the

decadal trend in observed OLR was most due to instrumentation issues instead of real physical signals [*Wong et al.*, 2006]. Since 2005, more studies about the circulation change in response to global warming have been carried out, partly due to the availability of IPCC AR4 archives to the entire community. Three of the most notable studies are summarized below. Using the west-east gradient of sea level pressure (∇SLP) along the equatorial Pacific region as a measure of the strength of atmospheric circulation over the Pacific, *Zhang and Song* [2006] analyzed ship-based observations and reanalysis dated back to 1950 and it showed a decreased trend of the ∇SLP, which suggests a weakening of the Walker circulation. They further contemplated that the change of lapse rate (thermal stability) is the physical reason for such a change in circulation. *Vecchi et al.* [2006] showed a decreased trend of ∇SLP from long-term span of observations of SLP over the tropical Pacific as well as from simulations carried out by five coupled-GCMs. *Vecchi and Soden* [2007] further examined twenty-two IPCC AR4 GCMs in the A1B scenario and showed that all the models consistently projected a weakening of tropical circulation under the global warming scenario. An ensemble mean of the twenty-two GCMs shows that the strength of the tropical circulation would weaken as the climate warms and that such a weakening would be dominated by the zonally asymmetric circulation (i.e. the Walker circulation) instead of meridional circulation.

In spite of the aforementioned studies, there has been no theory yet to satisfactorily explain the weakening of Walker circulation that has been observed in the SLP or has been simulated by the GCMs. Occasionally in conferences and meetings, the scaling argument proposed by *Held and Soden* [2006] is used to support the weakening of tropical circulation. The argument is summarized as below:

(1) Based on the global thermodynamic constraints on the hydrologic cycle, the global mean precipitation (P) would equal to the product of convective mass flux (Mc) and typical boundary layer mixing ratio (q), i.e.,

$$P = Mc \cdot q \qquad (5.1)$$

(2) The fractional change of global mean precipitation can then be written as

$$\frac{\delta P}{\overline{P}} = \frac{\delta Mc}{\overline{Mc}} + \frac{\delta q}{\overline{q}} \qquad (5.2)$$

where the overbar indicates the mean state and the δ is the deviation from the mean state.

(3) Under a warmer climate (e.g. A1B scenario), the IPCC AR4 GCMs project a smaller increased rate of global-mean precipitation (~2% K^{-1}) than that of water vapor (~7% K^{-1}, which roughly follows the Clausius-Clayperon relation). As a result, Mc must decrease rapidly and the GCMs show such a decrease of convective mass flux [*Held and Soden*, 2006].

While this scaling argument is elegant and simple, it is applicable only to a global average. For an average over a particular region, e.g., the tropical belt, a large portion of the moisture source for precipitation could possibly be supplied by the horizontal transport of water vapor from any other region; therefore, Eq. 5.1 is not held to be true anymore so the scaling argument in Eq. 5.2 is claimed invalid.

Numerous studies have used the radiative-convective equilibrium (RCE) model to understand the tropical circulation, especially the gross features of the time-invariant component of Walker circulation. Unlike zonal circulations (Hadley circulation), where

the interactions between the tropics and extra-tropics must be taken into account, the Walker circulation is confined in the tropics so a RCE model or a two-box model with one ascending and one descending branches is adequately a good first-order approximation. Under such equilibrium, downward motion at the descending branch causes adiabatic warming of the air parcel, which is balanced by the clear-sky radiative cooling. Therefore, the downward mass flux in the descending branch can be calculated from the clear-sky radiative cooling rate and the lapse rate. Meanwhile, the downward mass flux at the descending branch must be balanced by the upward mass flux at the ascending branch at each level when the system reaches equilibrium. The success of the RCE model and these balance relationships serve as motivation to explore the weakening of the Walker circulation in such a highly simplified model and theoretical framework. Though the lapse rate change is deemed as one of the reasons for the weakening of tropical circulation [*Knutson and Manabe*, 1995; *Zhang* and *Song*, 2006], the clear-sky radiation cooling rate will change in response to global warming and its contribute to the circulation change has not been discussed before. The main topic of this chapter is to explore the change of clear-sky cooling rate in response to the increase of greenhouse gases and global warming, and also to what extent it can be used to explain the weakening of tropical Walker circulation. Primarily, the change of vertical velocity as an indicator for the change of large-scale circulation will be used. Section 5.2 presents a heuristic argument based on the IR radiative transfer, water vapor feedback and the aforementioned balance relations to explain why and how the change of radiative cooling rate would affect the change of vertical velocity. In Section 5.3, the 1-D Radiative-Convective Equilibrium (RCE) simulation is shown to be able to reproduce the decrease

of vertical velocity. In Section 5.4 the estimated change of vertical velocity based on the simple RCE framework with the changes simulated by the GFDL coupled-GCM for A1B scenario [*Solomon et al.*, 2007] are compared. Discussion and conclusions are then presented in Section 5.5.

In terms of the GFDL simulation, two time periods are primarily analyzed. One period is 1971-2000 in the IPCC AR4 historical run simulated by the GFDL coupled-GCM, CM2.1 [*Delworth et al*., 2006]. The other period is 2071-2100 in the IPCC AR4 A1B scenario run (SRES A1B run) simulated by the CM2.1. For brevity, hereafter the first period will be referred to as 20C and the second period as 21C.

5.2 A heuristic argument on the change of vertical velocity in the tropical circulation

Using the theoretical framework of RCE that has already been discussed in Chapter 2, the adiabatic warming of downward motion in the descending branch is balanced by the clear-sky radiative cooling. Together with the hydrostatic equation, it means the vertical velocity can be written as

$$\omega = \frac{g \cdot Q_R}{C_p(\frac{dT}{dz} + \Gamma_d)} \tag{5.3}$$

where C_p is the heat capacity of dry air, T is the temperature, z is the altitude, Γ_d is the dry-adiabatic lapse rate, g is the gravity acceleration and Q_R is the clear-sky radiative cooling rate. If we use subscript $_f$ to denote future climate and subscript $_c$ to denote current climate, it is trivial to show that

$$\omega_f = \omega_c \frac{\left(1 + \frac{Q_{R_f} - Q_{R_c}}{Q_{R_c}}\right)}{\left(1 + \frac{\left(\frac{dT}{dz}\right)_f - \left(\frac{dT}{dz}\right)_c}{\left(\frac{dT}{dz} + \Gamma_d\right)_c}\right)} \tag{5.3a}$$

Note the temperature increase in the upper troposphere is faster than that of the lower troposphere and surface temperature increase, therefore, the lapse rate (*-dT/dz*) feedback is a negative feedback and the denominator in Eq. 5.1a is always positive. Thus, ***if lapse rate changes but Q_R remains unchanged, vertical velocity will decrease at every altitude according to Eq. 5.3a***. If the change of Q_R is negative, ω_f is guaranteed to be smaller than ω_c. If the change of Q_R is positive, the fractional change must be smaller than the fractional change of lapse rate in order to have ω_f smaller than ω_c.

Regarding the change of Q_R in response to global warming, following facts need to be taken into account:

(1) Clear-sky Q_R in the troposphere is mainly due to the water vapor absorption and emission. In the tropics above 750 hPa, it is mainly due to the absorption and emission of the water vapor pure rotational band (a.k.a. the far-IR band, < 600 cm^{-1}). Below 750 hPa, it is mainly due to the water vapor absorption and emission range being in the mid-IR window region. This can be clearly seen from the spectral cooling rate plot in Figure 5.1.

(2) Clear-sky Q_R can be well approximated by the cooling-to-space (CTS) approximation [*Rodgers and Walshaw*, 1966], i.e.,

$$Q_{R_v} \sim B_v(T)\frac{\partial \mathcal{T}_{vdiff}}{\partial z} \tag{5.4}$$

where diffusive transmissivity $\mathcal{T}_{vdiff} = 2\pi\int_0^1 \mathcal{T}_v \mu d\mu, \mu = \cos\theta,$

subscript *v* indicates frequency, $B_v(T)$ is the Planck function, $\mathcal{T}$ is the transmissivity at a given zenith angle θ.

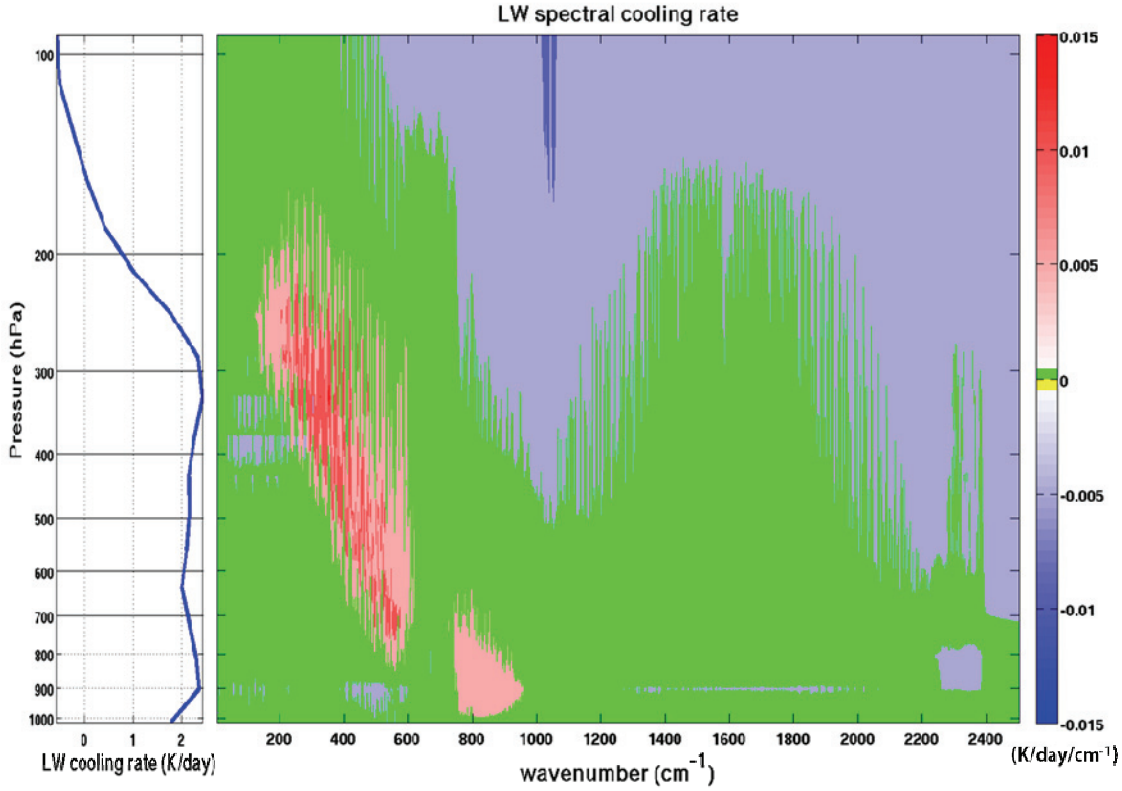

Figure 5.1. Typical tropical clear-sky cooling rate. The left panel shows the total LW cooling rate in K/day and the right panel shows the spectral cooling rate in the LW in K/day per cm^{-1}. A set of typical tropical sounding profiles [*McClatchey et al.*, 1972] is fed into MODTRAN5, an efficient and fast radiative transfer code, to calculate the spectral cooling rate. Note the green color in the right panel deliberately refers to slightly positive cooling rate.

(3) The derivative of $\mathcal{T}_{vdiff}$ with respect to z is usually termed as the weighting function $W(z)$. For an optically thick band such as water vapor far-IR band ($\mathcal{T}_{v\text{diff}}$ and $\mathcal{T}_v$ approaches zero at the surface),

$$W_v(z) = \frac{\partial \mathcal{T}_{vdiff}(z)}{\partial z} = \frac{\partial}{\partial z} 2\pi \int_0^1 \mathcal{T}_v(z;\mu)\,\mu d\mu = 2\pi\rho(z)k(z)\int_0^1 \mathcal{T}_v(z;\mu)\,d\mu \qquad (5.5)$$

which makes use of defintion $\mathcal{T}_v(z;\mu) = \exp\left[-\frac{\int_z^{+\infty}\rho(z)k_v(z)dz}{\mu}\right]$

where ρ is the mass density of absorber, k_v is the absorption coefficient. At the top of the atmosphere (TOA), $W_v(+\infty)=0$ because $\rho(+\infty)=0$ while the rest variables in Eq. 5.5 are all finite. At the surface, $W_v(0)$ is nearly zero because $\mathcal{T}(0;\mu)$ is close to zero for all zenith angles due to the large optical depth of the entire atmosphere. Meanwhile, it is trivial to show that $W_v(z)$ is non-negative within the atmosphere. Therefore, $W_v(z)$ must be bell-shaped with the maximum somewhere in the atmosphere and zero at both ends, in both current climate and in future climate. Furthermore, it can be shown that $W_v(z)$ attains its maximum when the optical depth $\tau \approx 1$ [*Goody and Yung*, 1989; *Stephen*, 1994]. For the water vapor far-IR band, $W_v(z)$ peaks in the troposphere and because of the CTS approximation, is very close to the altitude which has the maximum cooling rates as shown in Figure 5.1.

(4) As the surface temperature increases due to the increase of greenhouse gases, such as CO_2, the water vapor feedback will lead to an increase of water vapor in the entire troposphere. Since $\tau_v(z)$ monotonically increases from TOA downward to the surface, more water vapor means the altitude for the peak of $W_v(z)$ (i.e. the altitude for $\tau_v \approx 1$) in global warming scenario will be higher than that in current climate. If we denote the altitude for the peak of $W_v(z)$ for the entire far-IR band is z_c for current climate and z_f for the global warming scenario, we will have $z_f > z_c$. But at both the surface and TOA, $W_v(z)$ is zero regardless if using current or future climate. Therefore, the shape of $W_v(z)$ must change in following way:

(a) Above an altitude of z_0 that is between z_f and z_c, $W_v(z)$ of future climate is always larger than that of current climate.

(b) Below z_0, $W_v(z)$ of future climate is always smaller than that of current climate.

Such changes of the shape of $W_v(z)$ can indeed be seen from the GCM global warming experiments. Figure 5.2 shows the weighting function of the water vapor far-IR band as computed from the 20th century 30-year average (1971-2000) of temperature and humidity profiles from a GFDL coupled-model historical run, as well as the corresponding weighting function based on the 21st century 30-year average (2071-2100) from an SRES A1B run by the same model. The two weighting function profiles do change as explained above.

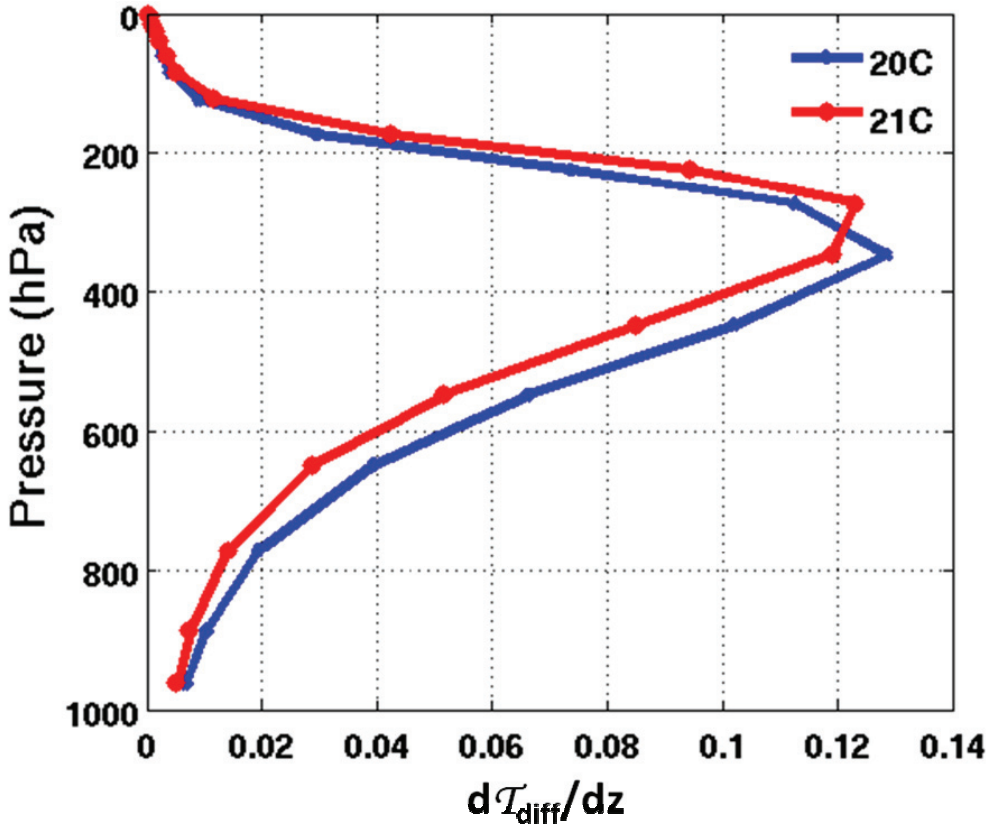

Figure 5.2. The derivative of diffusive transmission function with respect to altitude (i.e., the weight function) for the H_2O far-IR band (1-400 cm^{-1}). The blue curve is based on 30-year mean profiles of tropical temperature and humidity (1971-2000) simulated by the GFDL CM2.1 for the IPCC AR4 historical run (referred as 20C). The red curve is similar to the blue curve except the profiles are from 30-year means (2071-2100) from the GFDL CM2.1 SRES A1B simulation (referred as 21C).

(5) ***If everything else was unchanged***, such changes in $W_v(z)$ would directly translate to following conclusions:

(a) Above z_0, Q_R will be larger than the current value as global surface temperature increases and, given Eq. 5.3, a stronger downward velocity would be expected above z_0.

(b) Below z_0, the change is just opposite. Q_R will become smaller than the current value as global surface temperature increases and, therefore, a decrease of downward velocity would be expected. Figure 5.2 shows that z_0 is ~300 hPa (i.e., ~10 km), suggesting reduced downward vertical velocity in the descending branch over a majority of the troposphere, but an increase of downward velocity in the uppermost layer of troposphere. In the equilibrium state, the upward vertical velocity must change accordingly at each level. Therefore, a weakening of the circulation below z_0 would be expected for both ascending and descending branches.

As discussed in the beginning of this section, the inference of (a) on the current page might not be held true when the lapse rate change is considered, but the inference of (b) still holds as long as the lapse rate feedback is negative. In summary, the main idea of this argument is that the increase of water vapor in the atmosphere would lead to the change of vertical structure of clear-sky radiative cooling profile in the troposphere. To compensate such a change under the radiative-convective equilibrium, the downward vertical velocity has to be reduced below an altitude z_0 and has to be increased above it. However, in reality not only water vapor changes, but the temperature and lapse rate also would change with global warming. The temperature change also affects Q_R, while the lapse rate change directly affects the vertical velocity as shown in Eq. 5.3. In the next two

sections, to what extent lapse rate change matters and to what extent the change of clear-sky cooling rate must be taken into account will be explored.

5.3 Results from the RCE model

The same idealized steady-state radiative-convective model by *Minschwaner and Dessler* [2004] (hereafter *MD*04) that has been described in Chapter 2 is used here. This conceptual model separates the tropics into two boxes: one with the ascending motions in the convective region and the other with descending motion in the clear-sky region. The model describes the balance between adiabatic warming and clear-sky radiative cooling over the clear-sky region, as well as the conservation of humidity through the detrainment process, which assumes negligible contribution from evaporation of condensates. For brevity, the equations will not be given here and they can be found in Section 2.2.3. For any given surface temperature and surface relative humidity, the moist pseudoadiabatic profile of temperature is calculated and then the steady-state solution of the net radiative cooling rate, downward mass flux (M_d) and humidity are iteratively obtained. Note that the humidity is iteratively calculated from the convection detrainment layer to 80 hPa below the detrainment layer. Below this pressure range, the humidity is interpolated to humidity at the lifting condensation level and thus the results of the lower troposphere and planetary boundary layer (PBL) are simply interpolations after the upper-level humidity is determined. This simplified treatment for the lower troposphere and PBL can reduce the confidence of the change of vertical velocity computed from the *MD*04 model.

Figure 5.3a shows the equilibrium downward mass flux (M_d) from *MD*04 model for a surface temperature of 299 K and a surface temperature of 301.8K. The two values are chosen to mimic the global mean surface temperature change in the GFDL runs that are

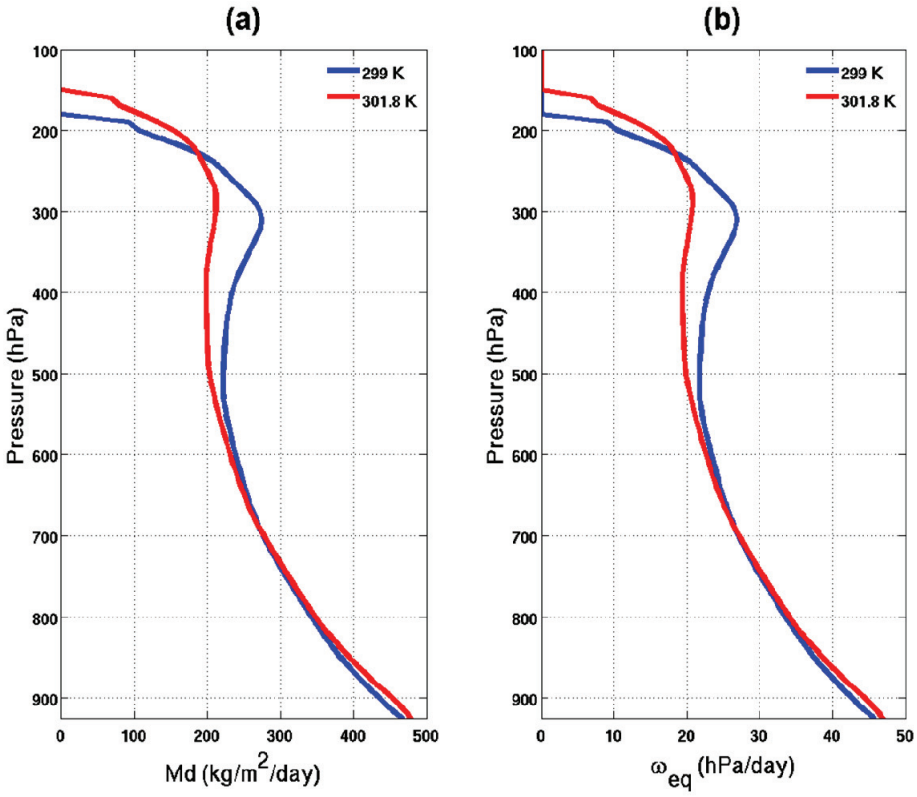

Figure 5.3. Profiles of the (a) equilibrium downward mass flux (Md) and (b) equilibrium vertical velocity (ω_{eq}) at the descending branch as calculated from *MD*04. Blue line is for prescribed surface temperature of 299K and red line is for surface temperature of 301.8K.

to be analyzed in the next section. The downward mass flux is decreased between 220 and 700 hPa and increased between 220 hPa and 150 hPa. Such an increase in the upper-most layer of the troposphere is consistent with the argument presented in Section 5.2. Figure 1b in the *MD*04 original paper also showed similar changes of mass flux when surface temperature increases. Correspondingly, the downward vertical velocity profiles for the two cases are shown in Figure 5.3b. Between 220 hPa and 150 hPa, the downward vertical velocity is enhanced in the warmer case and reduced below 220 hPa. The 1D-RCE simulation is consistent with the heuristic argument in Section 5.2 that the downward vertical velocity is reduced below a certain level (220 hPa in this case,

comparable to the 300 hPa indicated in Figure 5.2) and increased above that level in the corresponding warmer case.

5.4 Comparison with coupled-GCM simulations

As explained at the end of Section 5.1, 20C and 21C are used to denote the two 30-year periods that are analyzed. Since the Walker Circulation is the only focus, the inner tropics are defined as the tropical belt within 3°S-17°N, which is symmetric to the climatological position of ITCZ (Inter-Tropical Convergence Zone) at 7-8°N. Using the 30-year average of each period, two mean profiles are constructed for 3°S-17°N: one for 20C and one for 21C.

5.4.1 Estimated change of downward velocity from the clear-sky radiative cooling

Using the clear-sky net cooling rate and temperature from the GFDL output, the downward velocity can be derived based on Eq. 5.3. Figure 5.4a shows the profiles of the clear-sky net radiative cooling rates for 20C and 21C and Figure 5.4b shows the vertical velocity (hereafter, ω_{est}) estimated from such clear-sky radiative cooling rate. Above 300 hPa, the cooling rate of 21C is larger than that of 20C, which is consistent with the reasoning presented in Section 5.2. Above 250 hPa, the derived ω_{est} is larger in 21C than in 20C. Note the lapse rate change is included in our estimation. Thus, the increase of downward velocity in the upper most layer of the troposphere is still true when taking lapse rate change into account. As expected, below 250 hPa, ω_{est} is reduced in the case of 21C.

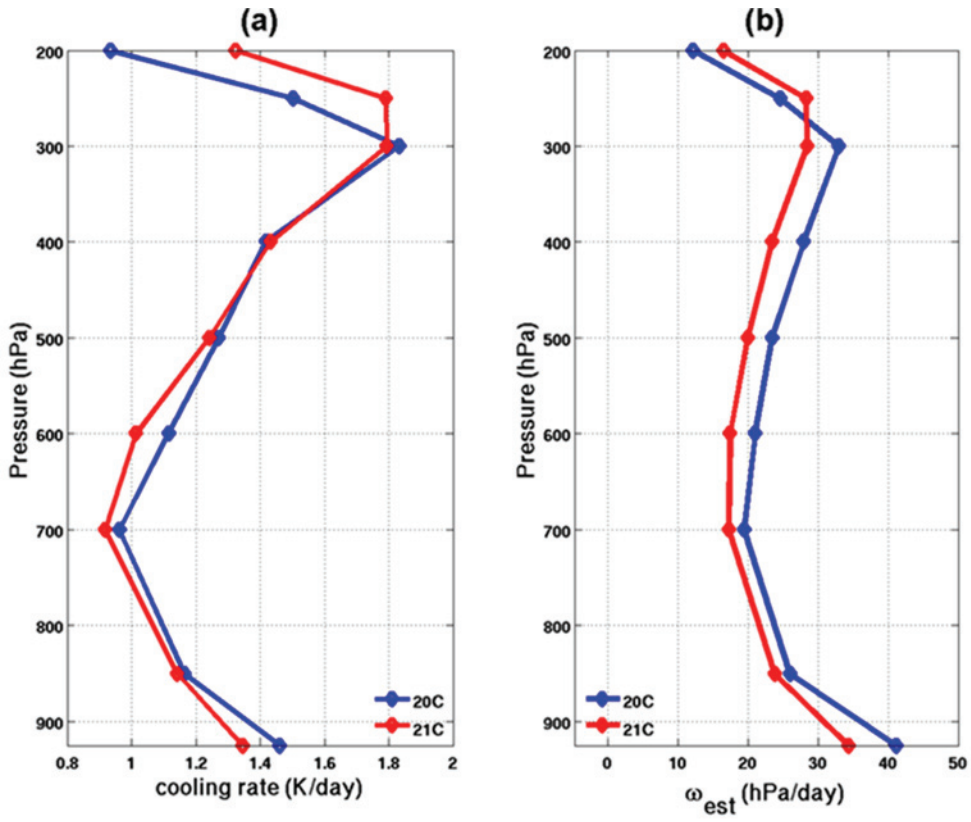

Figure 5.4. (a) 30-year mean of the inner tropical (3°N-17°N) clear-sky net radiative cooling rate calculated by the GFDL CM2.1 simulations of 20C (blue) and 21C (red). (b) The vertical velocity (ω_{est}) estimated from such clear-sky cooling rate by Eq. 5.3.

5.4.2 Direct output of ω from GFDL

It is not straightforward to obtain the exact counterpart in GCM simulations for the vertical velocity defined in the two-box RCE model (i.e. Eq. 5.3). A typical grid box of a GCM is ~ 200 km by 200 km. For any given GCM gridbox, even its grid-averaged vertical velocity is upward, it indeed does contain both the upward and downward motions within the gridbox because in most cumulus parameterizations, the convection (upward motion) is assumed to occupy only a small portion of the entire gridbox. Time

averages that are converted to monthly means or annual means further complicate the issue. Due to interest only in the vertical velocity at the downward branch of RCE framework, the mean vertical velocity profiles are calculated by:

(1) For each month and each pressure level, only average over the grid box with a positive monthly-mean vertical velocity in pressure (i.e. monthly-mean downward motion). Take the average as the monthly-mean vertical velocity at the descending branch

(2) Compute the 30-year mean based on the monthly mean computed in (1) and denote it as ω_{dn}.

(3) Compute the vertical velocity at the ascending branch in a similar fashion as (1) and denote as ω_{up}.

Figure 5.5a shows profiles of such vertical velocities for the 20C and 21C cases computed from the GFDL monthly-mean output. The vertical velocity calculated for the two branches are plotted separately. The corresponding fractional areas of ascending and descending branches are shown in Figure 5.5b.

Below 250 hPa, the values of ω_{dn} and ω_{up} decrease in 21C than in 20C, especially in the middle and upper troposphere (~300-700 hPa). Above 250 hPa, the values are only slightly larger in 21C than in 20C, which is not identifiable in Figure 5.5a. In addition to the velocity plot, Figure 5.5b plots the fractional areas for the large-scale ascending and descending branches as defined above. The area of descending branch is comparable to that of ascending branch in the middle and upper troposphere. In the planetary boundary layer and lower troposphere, the area of ascending branch is larger than that of descending branch.

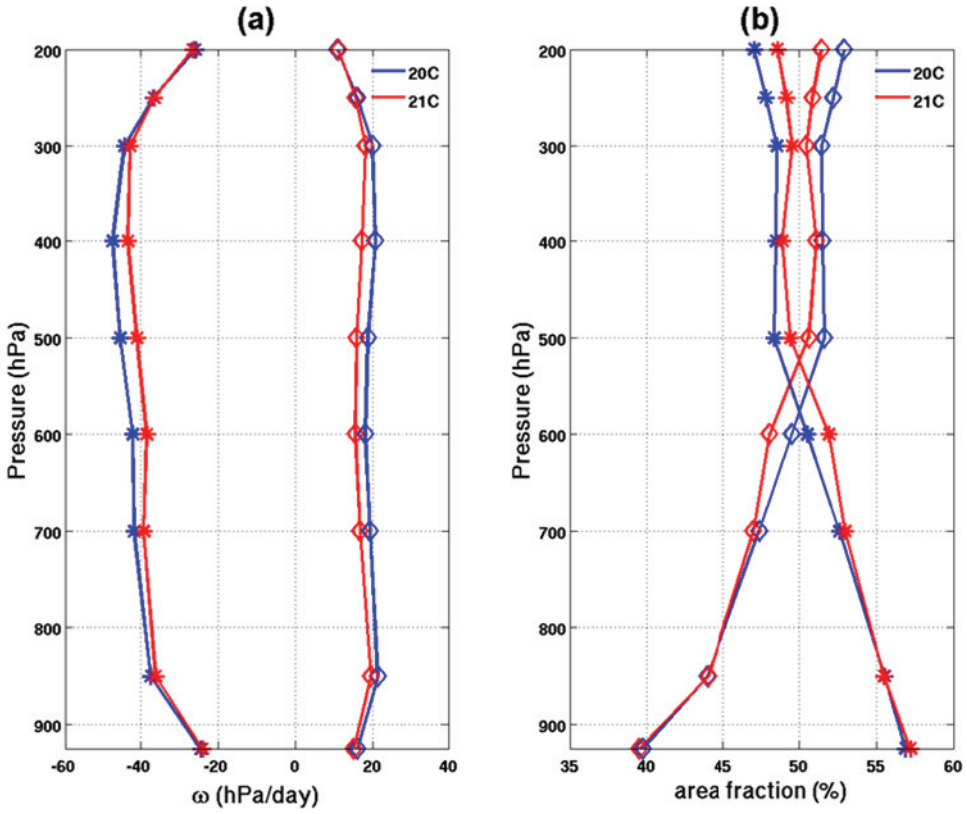

Figure 5.5. The GFDL CM2.1 mean profile of (a) vertical velocity, ω, in hPa/day and (b) fractional area for the ascending (lines with stars) and descending branches (lines with diamonds). The case of 20C is in blue and 21C in red.

5.4.3 Comparison between direct model output and estimation

Figure 5.6 summarizes the two sets of downward vertical velocity from GFDL CM2.1. One set is the direct output of ω over the descending area as described in Section 5.4.2 (ω_{dn}) and the other is counterpart derived in Section 5.4.1 by Eq. 5.3 (ω_{est}). Although ω_{est} is larger than ω_{dn} at all relevant pressure levels, both sets show a reduced vertical velocity below 300 hPa. The differences between 21C and 20C are presented in Figure 5.7, along with the differences calculated from *MD*04 for the surface temperatures of 299 K and 301.8 K. Three sets of ω are consistent in terms of the sign of the changes in the middle and upper troposphere; ω is increased at the uppermost layer of troposphere (above 240-

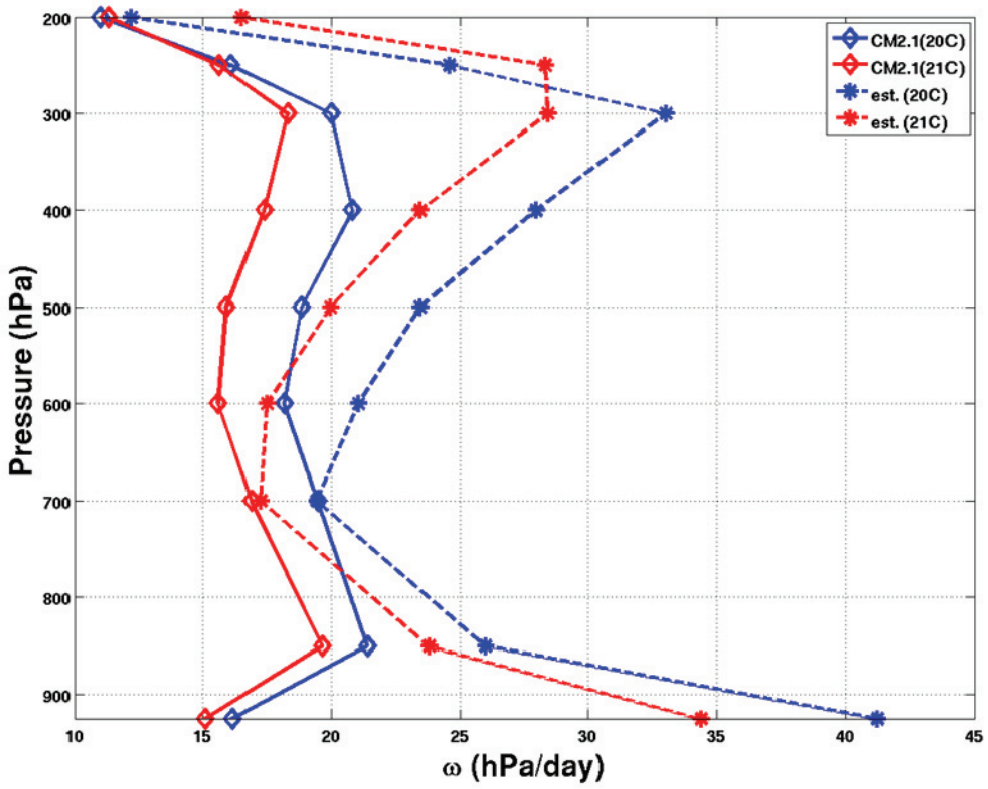

Figure 5.6. Mean vertical velocity of the descending branch. Solid lines with diamonds are directly output of the GFDL CM2.1 calculation and dashed lines with stars are estimated based on the CM2.1 clear-sky cooling rate and Eq. 5.3.

280 hPa) and weakened in the rest part of upper and middle troposphere. The magnitude of changes estimated by Eq. 5.3 is comparable to what CM2.1 computed in most of the troposphere and the largest differences being seen at the upper most troposphere (< 250 hPa) and at the PBL (> 925 hPa). *MD*04 results show a positive change of ω below 800 hPa but this is likely not trustworthy. As articulated in Section 5.3, changes in the lower troposphere and in PBL in the *MD*04 model may not be reliable. Nevertheless, both the GCM and such calculations based on the simple RCE framework show the results consistent with what the heuristic argument in Section 5.2 predicts about the sign of changes and the altitude of such changes.

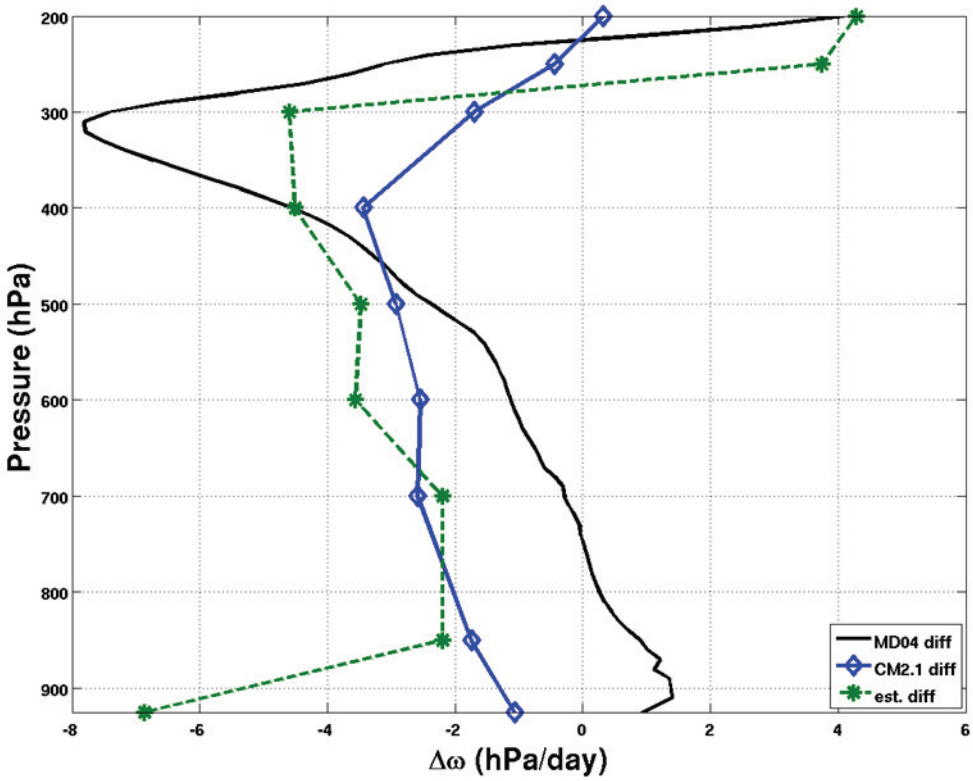

Figure 5.7. Profiles of the difference of vertical velocity. The black solid line is the vertical velocity difference between the two specified surface temperatures (shown in Figure 5.3). The vertical velocity difference over the descending area of the two centuries from GFDL CM2.1 is denoted as the blue line and the derived vertical velocity (ω_{est}) difference is denoted as the green line.

Because Eq. 5.3 is able to capture, to a large extent, the change of vertical velocity from current climate to future warmed climate, it can then be used to explore the sensitivity of such vertical velocity changes to the changes of radiative cooling rate as well as the changes of the lapse rate. This is done by calculating the vertical velocities with the 21C cooling rate and the 20C lapse rate (termed as "estimate 1") and then with the 20C cooling rate and the 21C lapse rate (termed as "estimate 2"). Then, the differences from the case with both 20C quantities are computed and compared to the corresponding difference shown in Figure 5.7 (the curve of "estimate").

The sensitivity results are summarized in Figure 5.8. Above 300 hPa, the change due to the cooling rate dominates the total change. This can be understood by the change of lapse rate. The lapse rate above 200-300 hPa is smaller than at levels below 300hPa due to the proximity to the tropopause. As a result, in response to the effects of global warming, lapse rate in such layers do not change as drastically as that in the layer right below it. Between 300 hPa and 600 hPa, the contribution of the lapse rate change dominates over that of the cooling rate. This is also the range where the lapse rate change is largest. Below 600 hPa, the contributions of the cooling rate change and lapse rate change are comparable to each other. As mentioned in Sections 5.1 and 5.2, if only the

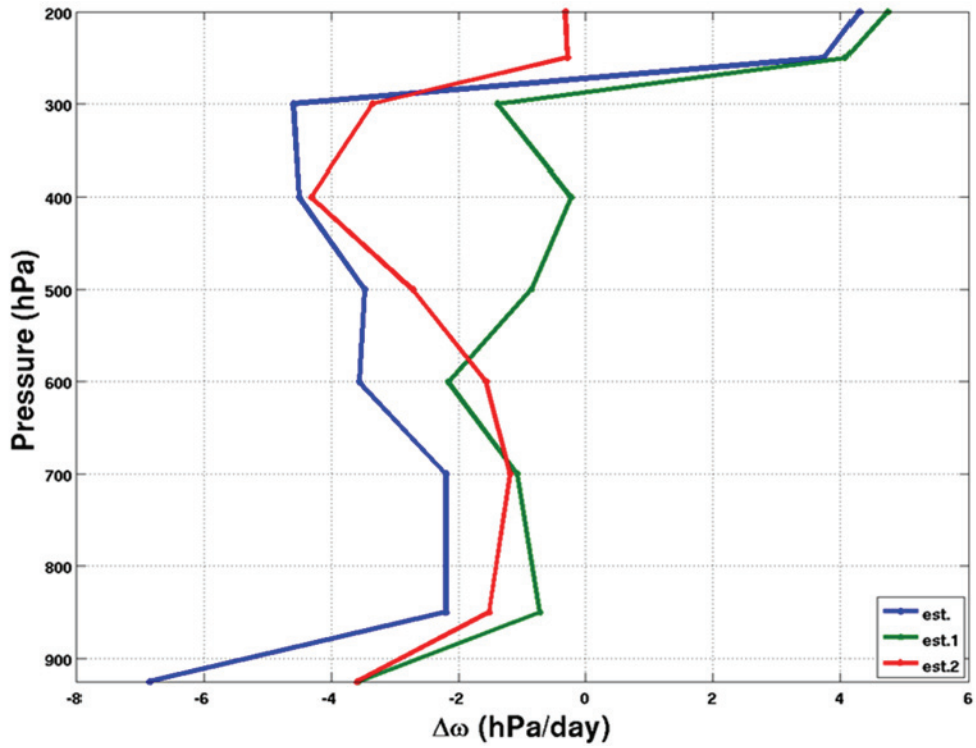

Figure 5.8. Profiles of the change of vertical velocity. Blue line (est.) indicates the difference of ω_{est} between the two centuries. Green line (est.1) is the change of ω if only the net cooling rate is changed. Red line (est. 2) is the change of ω if only the lapse rate is changed.

lapse rate changed, there would not be an increased downward vertical velocity in the uppermost part of the troposphere. This fact is shown in Figure 5.8 as well.

5.5 Conclusion and Discussion

Using the highly simplified 1-D RCE framework, a heuristic argument for how the change of water vapor due to global warming can affect the large-scale circulation (vertical velocity) is presented. Based on the two-box RCE model which depicts the tropics as two boxes, one with convective ascending and the other with large-scale radiatively induced subsidence, the downward vertical velocity is related to the clear-sky radiative cooling rate and to the lapse rate, as stated in Eq. 5.3. The clear-sky cooling rate can be related to the weighting function of water vapor bands (primarily the far-IR band) based on the CTS approximation. The shape of the weighting function will change in such a way to reduce clear-sky cooling rate in most of the troposphere but increase it in the uppermost part of the troposphere. This in turn would produce a decrease of vertical velocity in most of the troposphere and an increase of it in the upper portion of the troposphere. It is shown that Eq. 5.3 can be used to estimate the changes of vertical velocity from 20C to 21C and the estimates generally agree with the changes directly computed by the fully coupled-GCM. The slight increase of vertical velocity in the uppermost part of the troposphere is also seen in the GCM result, which can be explained by a change of the clear-sky cooling rate but not by the change of the lapse rate. The heuristic argument is confirmed by the GCM results as well as results from *MD*04 model. The sensitivity test shows that, at the different parts of the troposphere, the contributions of the lapse rate change and clear-sky cooling rate change to the total vertical velocity changes are different, with the lapse rate dominating in the middle troposphere but the

two factors are comparable in the lower troposphere. Above 300hPa, the change of the radiative cooling rate is the major contribution. In most of the troposphere, both radiative cooling rate change and lapse rate change are ingredients to reduce the vertical velocity and, hence, will weaken the circulation. *Knutson and Manabe* [1995] used the energy balance to explain why there is no enhanced Walker circulation when the convection/condensation heat is enhanced over the warm pool in a coupled-GCM. Three types of energies are always in balance: the convection/condensation heating, radiative cooling and dynamical cooling or heating (dependent on ascending or descending motion as well as the static stability). Over the convective region, most of the enhanced convection/condensation heating is counterbalanced by the enhanced radiative cooling which is resulted from the enhancement of both temperature and water vapor. The argument presented is consistent with their study but focuses on the subsidence/descending branch.

In the 1-D RCE argument, the increased downward motion in the uppermost part of the troposphere and the decreased downward motion below would imply a change of horizontal divergence at the turning point (~ 300 hPa). GCM simulations show a very small increase of downward motion (Figure 5.7), presumably due to the offset effect of the lapse rate change. In addition, the deviation from 1-D RCE framework should be taken into account if a more detailed discussion of vertical velocity change is preferred. Even for an idealized belt zone without diabatic flow across its boundary, it can be shown that the mean vertical velocity is not only related to the clear-sky cooling rate and lapse rate change, but also to the eddy mass flux along the vertical direction ($\overline{\omega'\rho'}/\overline{\rho}$), where symbols are defined as they normally are in the atmospheric dynamics textbook. In

reality, the diabatic flow across the boundary (e.g., the exchange between the tropics and extra-tropics) also needs to be considered. If the entire tropics (30°S-30°N) were chosen, instead of only the inner tropics for the analysis, the difference between the estimated ω and ω directly calculated from the CM2.1 would be much larger than what has been shown in this chapter. This highlights the contributions that would affect vertical velocity from other factors, such as aforementioned eddy flux and exchanges between tropics and extra-tropics. These factors should be taken into account for any future follow-up of this work in which to find a more complete understanding of the tropical circulation changes that are simulated by a GCM or that are observed.

5.6 Acknowledgements

We would like to acknowledge Prof. Andrew E. Dessler for the discussion at Gordon Research Conference which initiated this study. Prof. Kenneth R. Minschwaner provided guidance on the use of *MD*04 model. Calculations for Figures 5.1 and 5.2 were done in collaboration with Dr. Xiuhong Chen.

Chapter 6

Summary and Future work

6.1 Summary

The interannual variations of tropical upper tropospheric humidity (UTH) and high clouds as well as their relations with the large-scale dynamic/thermodynamic environment, have been examined in this study by using state-of-the-art GCM simulations, recently made available satellite observations, and reanalysis datasets. A simple radiative-convective equilibrium (RCE) framework has been used in a few of the chapters to elucidate the simple physics behind the complicated GCM simulations.

The start of this research examines the relations between the interannual anomalies of SST in the tropical strong precipitation regions (rainy-region SST) and the tropical UTH. The mean correlation coefficients between the interannual anomalies of UTH and the rainy-region SST are all higher than their counterparts when tropical-mean SST anomalies are used instead. The RCE model that assumes deep convection as the only source of water vapor is used to evaluate the contribution of tropical deep convection on the UTH variations. The dominant control of deep convection to the humidity is

corroborated in the lower portion (250-300 hPa) of the convective detrainment layer. Competition between deep convection and other mechanisms for regulating UTH varies significantly with different vertical ranges of the detrainment layer. Therefore, a reasonable representation of vertical convective detrainment profiles would be vital to simulating the moistening of the upper troposphere in the GCMs.

By separating the tropics into four ocean basins, the basin-scale interannual variations among UTH, cloud variables, and temperature variables of each basin are investigated. The interannual anomalies of basin-scale UTH show consistently positive correlations with those of basin-scale temperature variables, but diverse correlations with those of basin-scale cloud variables for each basin. The basin-scale UTH is modulated by the variations in the eastern Pacific (EP) and by its local convective activity, the latter of which is also affected by the EP variations. The EP can be deemed as the "forcing" region to influence interannual variability of the other ocean basins through the atmospheric bridge as well as the ocean tunnels. Four out of the five GCMs examined here have a seasonal dependence on the atmospheric bridge in the 21st century model runs, which is similar to that of the 20th century.

Current models and observations disagree significantly on the absolute amount of ice water path (IWP) in the atmosphere. Relationships between the IWP and the large-scale circulation are investigated over the tropical Pacific region. Two significantly linear relationships between the IWP and 500hPa vertical velocity (ω_{500}) are found: one is for their interannual anomalies in the current climate, and the other is for the long-term changes from the current to future climate. These two linear relationships are then correlated: the larger a modeled interannual variability is, the bigger the long-term

change of the same model. This provides a constraint of future IWP change associated with the large-scale circulation change. Together with the observed IWP_a-ω_{500a} relation, this constraint projects a ~3.38±0.42% decrease of IWP per 2hPa/day weakening of the ω_{500}, which is the simulated ensemble change of the Walker circulation over the tropical Pacific associated with every 1K global surface warming. Based on the GFDL simulation, this decrease of IWP would cause a 0.32±0.03Wm^{-2} (-0.05±0.007Wm^{-2}) change of cloud radiative effect at the surface (TOA) over the tropical Pacific for every 1K global warming. These results imply possible changes of the hydrological cycle in a warmer climate due to this decrease of the net cloud absorption.

A heuristic argument is presented to explain how the water vapor change, which is due to global warming, can affect the vertical velocity (i.e., the tropical Walker circulation). In a warmer climate, the increased surface temperature results in more water vapor in the atmosphere and together they change the vertical structure of the clear-sky radiative cooling rate (Q_R). Based on a two-box radiative-convective equilibrium (RCE) model, the Q_R can be linked to the vertical velocity of the descending branch of the Walker circulation. Such vertical structure changes of Q_R result in changes of the downward vertical velocity (i.e., changes of the circulation). Results based on this simple argument are consistent with what has been simulated by the GFDL GCM. A sensitivity test is carried out to examine the contributions of lapse rate and radiative cooling to the Walker circulation change and it is found that: (1) In the uppermost troposphere (< ~300hPa), the Q_R dominates the change of circulation and results in a slightly strengthened circulation in a warmer climate; (2) Between 300 and 500 hPa, the lapse rate dominates the change of circulation and leads to a weakened circulation; and (3)

Below 500 hPa, the lapse rate and Q_R have similar contributions to a weakened circulation.

6.2 Future work

The speculations and possible extensions for the future work are further discussed in this section. In Chapter 2, we focus on the variations of the tropical mean UTH, yet this arithmetical mean is not enough for a complete understanding of its impacts on the climate. *Sherwood et al.* [2006] and *Ryoo et al.* [2009] showed departures from a normal distribution of the tropical upper troposphere relative humidity, indicating the limited usage of the mean value to characterize the probability density function (PDF) of tropical relative humidity. A dry end of the PDF may have a stronger radiative impact than others, though. Using idealized GCM and reanalysis data, *O'Gorman et al.* [2011] recently demonstrated the limitation of poleward influence of inner-tropical humidity and provided a theoretical interpretation regarding the position of subtropical minima of humidity. How the observed and simulated PDF of the tropical UTH varies with dynamic and thermodynamic factor as well as to what degree CMIP3 and CMIP5 simulated changes of subtropical minima agree with these theoretical projections are worthy for further explorations.

In Chapter 3, we find that the behaviors of the relationship among the UTH, cloud variables, and temperature variables for the four tropical ocean basins are different and that the eastern Pacific (EP) serves as the forcing region. *Shin and Sardeshmukh* [2011] showed that a correct representation of tropical SST, especially the EP SST, is not only vital to the simulation of tropical climate but also crucial to the simulation of mid-latitude climate. Thus, it would be insightful to apply an atmospheric circulation model (e.g.

Quasi-equilibrium Tropical Circulation Model) with specified SSTs to further examine and delineate the physical mechanism of the basin-scale UTH variability.

The fact shown in Chapter 4, that models and observation agree so well on the fractional change of IWP with ω_{500} but disagree significantly on the absolute amount of IWP, is interesting and worthy for further understanding as well. It would be useful to understand to what extent the IWP would change with other factors (such as aerosol-cloud interaction) compared with the change with circulation. Meanwhile, Chapter 4 also points out the limitation of using TOA flux change alone to represent the future climate change and feedback. To further explore the implication of the study, it would be useful for us to explore an alternative way to delineate the feedback; for example, by defining the feedback at the TOA and the feedback at the surface.

The interactions between the tropics and extra-tropics are also worthwhile to study further. As noted in Chapter 5, we need to confine the latitude range such that the RCE model is adequate to approximate the tropics as two boxes with one ascending branch and one descending branch. However, in a real world situation, we cannot assume there are no source/sink terms from the north and south boundary of this latitude range. The contributions from the eddy flux and exchanges between tropics and extra-tropics should be taken into account to thoroughly understand the tropical circulation changes simulated by the GCM or observed in reality.

In addition to these possible research extensions, there are still many interesting topics for potential future work. Since we now have a decade of comprehensive high-quality observations from various aspects of our atmosphere from NASA TRMM, Terra, and A-Train satellite constellations, together with much more advanced reanalyses

project and vast amount of GCM simulations from CMIP5. These datasets can provide an exciting opportunity for climate diagnosis analysis with parallel usages of models and observations. While the studies here focus on the tropics, the same datasets can also be used to study water vapor and clouds in other climate zones, as well as the interactions between different climate zones. There have been recent studies suggesting the expansion of the Hadley circulation in the recent decades in response to global warming [*Fu et al.*, 2006; *Hu and Fu*, 2007; *Lu et al*., 2007; *Seidel and Randel*, 2007; *Seidel et al*., 2008], but the consequence of such expansion on water vapor, clouds, and precipitation has not been thorough examined yet. The synergistic use of observations, reanalyses, and GCM simulations would be ideal for diagnosing such issues.

Another interesting topic to go further in depth with is about variability and teleconnection patterns. While the ENSO dominates the interannual variability in the tropics, there are other patterns important for other regions and other timescales, such as the Arctic Oscillation (AO), Pacific Decadal Oscillation (PDO), Atlantic multidecadal oscillation (AMO), and Indian Ocean Dipole (IOD). To understand the atmospheric aspects associated these modes, including how clouds and radiation budget change with the mode variability, would expand our knowledge and provide a physical basis for us to postulate how such a mode will change in response to radiative perturbations, including the doubling of CO_2. From GCM simulations alone, how these major modes of atmospheric-ocean variability will change in the future climate is also worth for further investigation [*Palmer*, 1999].

Bibliography

Adler, R. F., et al. (2003), The version-2 global precipitation climatology project (GPCP) monthly precipitation analysis (1979–present), *J. Hydrometeorol.*, *4*, 1147–1167.

Alexander, M. A., N.-C. Lau, and J. D. Scott (2004), Broadening the atmospheric bridge paradigm: ENSO teleconnections to the North Pacific in summer and to the tropical west Pacific-Indian oceans over the seasonal cycle, in *Earth's Climate: The Ocean-Atmosphere Interaction*, *Geophys. Monogr. Ser.*, vol. 147, edited by C. Wang, S.-P. Xie, and J. A. Carton, pp. 85–104, AGU, Washington, D. C.

Alexander, M. A., I. Bladé, M. Newman, J. R. Lanzante, N.-C. Lau, and J. D. Scott (2002), The atmospheric bridge: The influence of ENSO teleconnections on air-sea interaction over the global oceans, *J. Clim.*, *15*, 2205–2231.

Bates, J. J., and D. L. Jackson (2001), Trends in upper-tropospheric humidity, *Geophys. Res. Lett.*, *28*(9), 1695–1698, doi:10.1029/2000GL012544.

Battisti, D. S., and E. S. Sarachik (1995), Understanding and predicting ENSO, *Rev. Geophys.*, *33*, 1367–1376.

Bell, T. L. (1980), Climate sensitivity from fluctuation dissipation: Some simple model tests,*J. Atmos. Sci.*, *37*, 1700–1707.

Betts, A. K. (1990), Greenhouse warming and the tropical water budget, *Bull. Am. Meteorol. Soc.*, *71*, 1464–1465.

Betts, A. K., and B. A. Albrecht (1987), Conserved Variable Analysis of the Convective Boundary-Layer Thermodynamic Structure over the Tropical Oceans, *J. Atmos. Sci.*, *44*(1), 83-99.

Betts, A. K., and W. Ridgway (1989), Climatic equilibrium of the atmospheric convective boundary layer over a tropical ocean, *J. Atmos. Sci.*, *46*, 2621–2641.

Bhat, G. S., et al. (2004), Sea surface temperature of the Bay of Bengal derived from the TRMM Microwave Imager, *J. Atmos. Ocean. Technol.*, *21*, 1283–1290.

Bony, S., et al. (2006), How well do we understand and evaluate climate change feedback processes?, *J. Clim.*, *19*, 3445–3482.

Boville, B. A., P. J. Rasch, J. J. Hack, and J. R. McCaa (2006), Representation of clouds and precipitation processes in the Community Atmosphere Model Version 3(CAM3), *J. Clim.*, *19*, 2184–2198, doi:10.1175/JCLI3749.1.

Bretherton, C. S., M. E. Peters, and L. E. Back (2004), Relationships between water vapor path and precipitation over the tropical oceans, *J. Clim.*, *17*, 1517–1528.

Bretherton, C. S., M. Widmann, V. P. Dymnikov, J. M. Wallace, and I. Bladé (1999), The effective number of spatial degrees of freedom of a time-varying field, *J. Clim.*,*12*, 1990–2009.

Broccoli, A. J., and S. A. Klein (2010), Comment on "Observational and model evidence for positive low-level cloud feedback," *Science*, *329*, 277, doi:10.1126/science.1186796.

Camp, C. D., M. S. Roulston, and Y. L. Yung (2003), Temporal and spatial patterns of the interannual variability of total ozone in the tropics, *J. Geophys. Res.*, *108*(D20), 4643, doi:10.1029/2001JD001504.

Chahine, M. T. (1974), Remote sounding cloudy atmospheres: I. The single cloud layer, *J. Atmos. Sci.*, *31*, 233–243.

Chen, J., B. E. Carlson, and A. D. Del Genio (2002), Evidence for strengthening of the tropical general circulation in the 1990s, *Science*, *295*, 838–841, doi:10.1126/science.1065835.

Chen, J. Y., A. D. Del Genio, B. E. Carlson, and M. G. Bosilovich (2008a), The spatiotemporal structure of twentieth-century climate variations in observations and reanalyses. Part I: Long-term trend, *J. Clim.*, *21*, 2611–2633.

Chen, J., A. D. Del Genio, B. E. Carlson, and M. Bolsilovich (2008b), The spatiotemporal structure of 20th century climate variations in observations and reanalyses. Part II: Pacific pan-decadal variability, *J. Clim.*, *21*, 2634–2650, doi:10.1175/2007JCLI2012.1.

Chuang, H., X. Huang, and K. Minschwaner (2010), Interannual variations of tropical upper tropospheric humidity and tropical rainy-region SST: Comparisons between models, reanalyses, and observations, *J. Geophys. Res.*, *115*, D21125, doi:10.1029/2010JD014205

Cionni, I., G. Visconti, and F. Sassi (2004), Fluctuation dissipation theorem in a general circulation model, *Geophys. Res. Lett.*, *31*, L09206, doi:10.1029/2004GL019739.

Clarke, L., J. Edmonds, H. Jacoby, H. Pitcher, J. Reilly, R. Richels (2007), Scenarios of Greenhouse Gas Emissions and Atmospheric Concentrations. Sub-report 2.1A of Synthesis and Assessment Product 2.1 by the U.S. Climate Change Science Program

and the Subcommittee on Global Change Research. Department of Energy, Office of Biological & Environmental Research, Washington, D.C., USA, 154 pp.

Clement, A. C., R. Burgman, and J. R. Norris (2009), Observational and model evidence for positive low-level cloud feedback, *Science*, *325*, 460–464, doi:10.1126/science.1171255.

de Boyer Montégut, C., G. Madec, A. S. Fischer, A. Lazar, and D. Iudicone (2004), Mixed layer depth over the global ocean: An examination of profile data and a profile-based climatology, *J. Geophys. Res.*, *109*, C12003, doi:10.1029/2004JC002378.

Delworth, T. L., et al. (2006), GFDL's CM2 global coupled climate models. part I: Formulation and simulation characteristics, *J. Clim.*, *19*, 643–674, doi:10.1175/JCLI3629.1.

Deser, C., and M. L. Blackmon (1995), On the relationship between tropical and North Pacific sea surface temperature variations, *J. Clim.*, *8*, 1677–1680.

Dessler, A. E., and S. C. Sherwood (2000), Simulations of tropical upper tropospheric humidity, *J. Geophys. Res.*, *105*, 20,155–20,163.

Dessler, A. E., Z. Zhang, and P. Yang (2008), Water-vapor climate feedback inferred from climate fluctuations, 2003–2008, *Geophys. Res. Lett.*, *35*, L20704, doi:10.1029/2008GL035333.

Donner, L. J., et al. (2011), The dynamical core, physical parameterizations, and basic simulation characteristics of the atmospheric component of the GFDL Global Coupled Model CM3, *J. Clim.*, *24*, 3484–3519, doi:10.1175/2011JCLI3955.1.

Fetzer, E. J., B. H. Lambrigtsen, A. Eldering, H. H. Aumann, and M. T. Chahine(2006), Biases in total precipitable water vapor climatologies from Atmospheric Infrared Sounder and Advanced Microwave Scanning Radiometer, *J. Geophys. Res.*, *111*, D09S16, doi:10.1029/2005JD006598.

Folkins, I. (2002), Origin of lapse rate changes in the upper tropical troposphere, *J. Atmos. Sci.*, *59*, 992–1005.

Folkins, I., S. J. Oltmans, and A. M. Thompson (2000), Tropical convective outflow and near surface equivalent potential temperatures, *Geophys. Res. Lett.*, *27*(16), 2549–2552.

Folkins, I., K. K. Kelly, and E. M. Weinstock (2002), A simple explanation for the increase in relative humidity between 11 and 14 km in the tropics, *J. Geophys. Res.*,*107*(D23), 4736, doi:10.1029/2002JD002185.

Fu, Q., C. M. Johanson, J. M. Wallace, and T. Reichler (2006), Enhanced midlatitude tropospheric warming in satellite measurements, *Science*, *312*, 1179, doi:10.1126/science.1125566.

Fu, R., et al. (1992), Cirrus-cloud thermostat for tropical sea-surface temperatures tested using satellite data, *Nature*, *358*(6385), 394–397, doi:10.1038/358394a0.

Fueglistaler, S., A. E. Dessler, T. J. Dunkerton, I. Folkins, Q. Fu, and P. W. Mote(2009), Tropical tropopause layer, *Rev. Geophys.*, *47*, RG1004, doi:10.1029/2008RG000267.

Gill, A. E. (1980), Some simple solutions for heat-induced tropical circulation, *Q. J. R. Meteorol. Soc.*, *106*, 447–462, doi:10.1002/qj.49710644905.

Gleckler, P. J., K. E. Taylor, and C. Doutriaux (2008), Performance metrics for climate models, *J. Geophys. Res.*, *113*, D06104, doi:10.1029/2007JD008972.

Goddard, L., and N. E. Graham (1999), Importance of the Indian Ocean for simulating rainfall anomalies over the eastern and southern Africa, *J. Geophys. Res.*, *104*(D16), 19,099–19,116.

Goody, R. M., and Y. L. Yung (1989), Atmospheric Radiation: Theoretical Basis, 519pp., Oxford University Press, New York.

Gregory, D., and P. R. Rowntree (1990), A mass flux convection scheme with representation of cloud ensemble characteristics and stability-dependent closure, *Mon. Weather. Rev.*, *118*, 1483–1506.

Gregory, D., and D. Morris (1996), The sensitivity of climate simulations to the specification of mixed phase clouds, *Clim. Dyn.*, *12*(9), 641–651.

Gregory, D., and S. Allen (1991), The effect of convective downdraughts upon NWP and climate simulations, *in Ninth conference on numerical weather prediction, Denver, Colorado*, 122–123.

Hack, J. J. (1994), Parameterization of moist convection in the National Center for Atmospheric Research Community Climate Model (CCM2), *J. Geophys. Res.*, *99*, 5551–5568, doi:10.1029/93JD03478.

Hall, A., and X. Qu (2006), Using the current seasonal cycle to constrain snow albedo feedback in future climate change,*Geophys. Res. Lett.*, *33*, L03502, doi:10.1029/2005GL025127.

Hartmann, D. L., and M. L. Michelsen (1993), Large-scale effects on the regulation of tropical sea surface temperature, *J. Clim.*, *6*, 2049–2062.

Hartmann, D. L., L. A. Moy, and Q. Fu (2001), Tropical convection and the energy balance at the top of the atmosphere, *J. Clim.*, *14*, 4495–4511.

Hartmann, D. L., and K. Larson (2002), An important constraint on tropical cloud-climate feedback, *Geophys. Res. Lett.*, *29*(20), 1951, doi:10.1029/2002GL015835.

Hartmann, D. L., and M. L. Michelsen (2002), No evidence for iris, *Bull. Am. Meteorol. Soc.*, *83*, 249–254.

Held, I. M., and B. J. Soden (2000), Water vapor feedback and global warming, *Annu. Rev. Energy Environ.*, *25*, 441–475, doi:10.1146/annurev.energy.25.1.441.

Held, I. M., and B. J. Soden (2006), Robust responses of the hydrological cycle to global warming, *J. Clim.*, *19*, 5686–5699, doi:10.1175/JCLI3990.1.

Hong, C. C. H., T. Li, L. Ho, and Y. C. Chen (2010), Asymmetry of the Indian Ocean basinwide SST anomalies: Roles of ENSO and IOD, *J. Clim.*, *23*, 3563–3576, doi:10.1175/2010JCLI3320.1.

Hong, C.-C., M.-M. Lu, and M. Kanamitsu (2008), Temporal and spatial characteristics of positive and negative Indian Ocean dipole with and without ENSO, *J. Geophys. Res.*, *113*, D08107, doi:10.1029/2007JD009151.

Houze, R. A., and A. K. Betts (1981), Convection in GATE, *Rev. Geophys. Space Phys.*, *19*(4), 541–576, doi:10.1029/RG019i004p00541.

Hu, Y., and Q. Fu (2007), Observed poleward expansion of the Hadley circulation since 1979, *Atmos. Chem. Phys.*, *7*, 5229–5236, doi:10.5194/acp-7-5229-2007.

Huang, X., B. J. Soden, and D. L. Jackson (2005), Interannual co-variability of tropical temperature and humidity: A comparison of model, reanalysis data and satellite observation, *Geophys. Res. Lett.*, *32*, L17808, doi:10.1029/2005GL023375.

Huang, X. L., V. Ramaswamy, and M. D. Schwarzkopf (2006), Quantification of the source of errors in AM2 simulated tropical clear-sky outgoing longwave radiation, *J. Geophys. Res.*, *111*, D14107, doi:10.1029/2005JD006576.

Huffman, G. J., R. Adler, M. Morrissey, D. Bolvin, S. Curtis, R. Joyce, B. McGavock, and J. Susskind (2001), Global precipitation at one-degree daily resolution from multi-satellite observations, *J. Hydrometeorol.*, *2*, 36–50.

Huffman, G. J., et al. (2007), The TRMM multi-satellite precipitation analysis: Quasi-global, multi-year, combined-sensor precipitation estimates at fine scale, *J. Hydrometeorol.*,*8*, 38–55, doi:10.1175/JHM560.1.

Ingram, W. J. (2002), On the robustness of the water vapor feedback: GCM vertical resolution and formulation, *J. Climate*, *15*, 917–921.

Jakob, C. (2002), Ice clouds in Numerical Weather Prediction models - progress, problems and prospects. In "Cirrus", edited by David K. Lynch et al., Oxford University Press, 327-345.

John, V. O., and B. J. Soden (2006), Does convectively-detrained cloud ice enhance water vapor feedback?, *Geophys. Res. Lett.*, *33*, L20701, doi:10.1029/2006GL027260.

John, V. O., and B. J. Soden (2007), Temperature and humidity biases in global climate models and their impact on climate feedbacks, *Geophys. Res. Lett.*, *34*, L18704, doi:10.1029/2007GL030429.

Kiehl, J. T., J. J. Hack, G. B. Bonan, B. A. Boville, D. L. Williamson, and P. J. Rasch (1998), The National Center for Atmospheric Research Community Climate Model: CCM, *J. Clim.*, *11*, 1131–1150.

King, M. D., W. P. Menzel, Y. J. Kaufman, D. Tanre, B. C. Gao, S. Platnick, S. A. Ackerman, L. A. Remer, R. Pincus, and P. A. Hubanks (2003), Cloud and aerosol properties, precipitable water, and profiles of temperature and water vapor from MODIS,*IEEE Trans. Geosci. Remote Sens.*, *41*, 442–458.

Klein, S. A., B. J. Soden, and N.-C. Lau (1999), Remote sea surface temperature variations during ENSO: Evidence for a tropical atmospheric bridge, *J. Clim.*, *12*, 917–932.

Knutson, T. R., and S. Manabe (1995), Time-mean response over the tropical pacific to increased CO_2 in a coupled ocean-atmosphere model, *J. Clim.*, *8*, 2181–2199.

Knutti, R., G. A. Meehl, M. R. Allen, and D. A. Stainforth (2006), Constraining climate sensitivity from the seasonal cycle in surface temperature, *J. Clim.*, *19*, 4224–4233.

Kuang, Z., and D. L. Hartmann (2007), Testing the fixed anvil temperature hypothesis in a cloud-resolving model, *J. Clim.*, *20*, 2051–2057.

Kubota, T., and T. Terao (2004), Interdecadal variability of the seasonal-scale persistence in the tropical mean tropospheric temperature, *J. Meteorol. Soc. Jap.*, *82*, 1213–1221.

Lacis, A. A., G. A. Schmidt, D. Rind, and R. A. Ruedy (2010), Atmospheric CO_2: Principal Control Knob Governing Earth's Temperature, *Science*, *330*(6002), 356-359.

Lau, N.-C. (1997), Interactions between global SST anomalies and the midlatitude atmospheric circulation, *Bull. Am. Meteorol. Soc.*, *78*, 21–33.

Lau, N., and M. J. Nath (1994), A modeling study of the relative roles of tropical and extratropical SST anomalies in the variability of the global atmosphere-ocean system, *J. Clim.*, *7*, 1184–1207.

Lau, N., and M. J. Nath (2001), Impact of ENSO on SST variability in the North Pacific and North Atlantic: Seasonal dependence and role of extratropical sea-air coupling, *J. Clim.*, *14*, 2846–2866.

Le Treut, H., R. Somerville, U. Cubasch, Y. Ding, C. Mauritzen, A. Mokssit, T. Peterson and M. Prather (2007): Historical Overview of Climate Change. In: Climate Change 2007: The Physical Science Basis. Contribution of Working Group I to the Fourth Assessment Report of the Intergovernmental Panel on Climate Change [Solomon, S., D. Qin, M. Manning, Z. Chen, M. Marquis, K.B. Averyt, M. Tignor and H.L. Miller (eds.)]. Cambridge University Press, Cambridge, United Kingdom and New York, NY, USA.

Leith, C. E. (1975), Climate response and fluctuation dissipation, *J. Atmos. Sci.*, *32*, 2022–2026.

Li, J.-L., et al. (2005), Comparisons of EOS MLS cloud ice measurements with ECMWF analyses and GCM simulations: Initial results, *Geophys. Res. Lett.*, *32*, L18710, doi:10.1029/2005GL023788.

Li, T., B. Wang, C.-P. Chang, and Y. Zhang (2003), A theory for the Indian Ocean dipole-zonal mode, *J. Atmos. Sci.*, *60*, 2119–2135.

Lin, B., B. A. Wielicki, L. H. Chambers, Y. X. Hu, and K. M. Xu (2002), The iris hypothesis: A negative or positive cloud feedback?, *J. Clim.*, *15*, 3–7.

Lindzen, R. S. (1990), Some coolness concerning global warming, *Bull. Am. Meteorol. Soc.*, *71*, 288–299

Lindzen, R. S., M. D. Chou, and A. Y. Hou (2001), Does the Earth have an adaptive infrared iris?, *Bull. Am. Meteorol. Soc.*, *82*, 417–432.

Liou, K. (1986), Influence of cirrus clouds on weather and climate processes: A global perspective, *Mon. Weather Rev.*, *114*(6), 1167–1199.

Liou, K.-N., and S.-Z. Ou (1989), The role of cloud microphysical processes in climate: An assessment from a one-dimensional perspective, *J. Geophys. Res.*, *94*, 8599–8607, doi:10.1029/JD094iD06p08599.

Liu, Z., and H. Yang (2003), Extratropical control of tropical climate, the atmospheric bridge and oceanic tunnel, *Geophys. Res. Lett.*, *30*(5), 1230, doi:10.1029/2002GL016492.

Liu, Z., and M. Alexander (2007), Atmospheric bridge, oceanic tunnel, and global climatic teleconnections, *Rev. Geophys.*, *45*, RG2005, doi:10.1029/2005RG000172.

Livesey, N. J., et al. (2007), Earth Observing System (EOS) Microwave Limb Sounder (MLS) Version 2.2 Level 2 data quality and description document. JPL technical report D-33509.

Livesey, N. J., et al. (2011), Earth Observing System (EOS) Aura Microwave Limb Sounder (MLS) version 3.3 level 2 data quality and description document, JPL D-33509, Jet Propulsion Laboratory, California Institute of Technology, Pasadena, California, USA, 162 pp.

Lohmann, U., and E. Roeckner (1996), Design and performance of a new cloud microphysics scheme developed for the ECHAM general circulation model, *Clim. Dyn.*, *12*, 557–572, doi:10.1007/s003820050128.

Lu, J., G. A. Vecchi, and T. Reichler (2007), Expansion of the Hadley cell under global warming, *Geophys. Res. Lett.*, *34*, L06805, doi:10.1029/2006GL028443.

McClatchey, R. A., R. W. Fenn, J. E. A. Selby, P. E. Volz, and J. S. Garing (1972), Optical properties of the atmosphere, 3e de., pp. 113, Air Force Cambridge Research Laboratory.

Meehl, G. A., T.F. Stocker, W.D. Collins, P. Friedlingstein, A.T. Gaye, J.M. Gregory, A. Kitoh, R. Knutti, J.M. Murphy, A. Noda, S.C.B. Raper,, and A. J. W. a. Z.-C. Z. I.G. Watterson (2007), Global Climate Projections. In: Climate Change 2007: The Physical Science Basis.

Miloshevich, L. M., A. Paukkunen, H. Vömel, and S. J. Oltmans (2004), Development and validation of a time-lag correction for Vaisala radiosonde humidity measurements, *J. Atmos. Oceanic Technol.*, *21*, 1305–1327.

Miloshevich, L. M., H. Vömel, A. Paukkunen, A. J. Heymsfield, and S. J. Oltmans(2001), Characterization and correction of relative humidity measurements from Vaisala RS80-A radiosondes at cold temperatures, *J. Atmos. Oceanic Technol.*, *18*, 135–156.

Miloshevich, L. M., H. Vömel, D. N. Whiteman, B. M. Lesht, F. J. Schmidlin, and F. Russo (2006), Absolute accuracy of water vapor measurements from six operational radiosonde types launched during AWEX-G and implications for AIRS validation, *J. Geophys. Res.*, *111*, D09S10, doi:10.1029/2005JD006083.

Ming, Y., V. Ramaswamy, and G. Persad (2010), Two opposing effects of absorbing aerosols on global-mean precipitation, *Geophys. Res. Lett.*, *37*, L13701, doi:10.1029/2010GL042895.

Minschwaner, K., and A. E. Dessler (2004), Water vapor feedback in the tropical upper troposphere: Model results and observations, *J. Clim.*, *17*, 1272–1282.

Mitas, C. M., and A. Clement (2005), Has the Hadley cell been strengthening in recent decades?, *Geophys. Res. Lett.*, *32*, L03809, doi:10.1029/2004GL021765.

Mitas, C. M., and A. Clement (2006), Recent behavior of the Hadley cell and tropical thermodynamics in climate models and reanalyses, *Geophys. Res. Lett.*, *33*, L01810, doi:10.1029/2005GL024406.

Moorthi, S., and M. J. Suarez (1992), Relaxed Arakawa-Schubert; A parameterization of moist convection for general circulation models, *Mon. Weather Rev.*, *120*, 978–1002.

Nordeng, T. E. (1994), Extended versions of the convective parameterization scheme at ECMWF and their impact on the mean and transient activity of the model in the tropics, *Technical Memorandum No. 206, European Centre for Medium-Range Weather Forecasts, Reading, United Kingdom.*

North, G. R., R. E. Bell, and J. W. Hardin (1993), Fluctuation dissipation in a general circulation model, *Clim. Dyn.*, *8*, 259–264.

O'Gorman, P. A. (2011), The Effective Static Stability Experienced by Eddies in a Moist Atmosphere, *J. Atmos. Sci.*,, *68*(1), 75-90.

Palmer, T. N. (1999), A nonlinear dynamical perspective on climate prediction, *J. Clim.*,*12*(2), 575–591.

Pierce, D. W., T. P. Barnett, E. J. Fetzer, and P. J. Gleckler (2006), Three-dimensional tropospheric water vapor in coupled climate models compared with observations from the AIRS satellite system, *Geophys. Res. Lett.*, *33*, L21701, doi:10.1029/2006GL027060.

Pierrehumbert, R. (2010), Principles of Planetary Climate. Cambridge University Press, 652pp, Pierrehumbert RT 2010: Principles of Planetary Climate. Cambridge University Press, 2652pp.

Pierrehumbert, R. T. (1995), Thermostats, radiator fins, and the local runaway greenhouse, *J. Atmos. Sci.*, *52*, 1784–1806.

Pierrehumbert, R. T. (1998), Lateral mixing as a source of subtropical water vapor,*Geophys. Res. Lett.*, *25*, 151–154.

Pierrehumbert, R. T., and R. Roca (1998), Evidence for control of Atlantic subtropical humidity by large scale advection, *Geophys. Res. Lett.*, *25*, 4537–4540.

Pierrehumbert RT, B. H., and Roca R (2007), On the relative humidity of the atmosphere. in The Global Circulation of the Atmosphere, T. Schneider and A. Sobel, eds. Princeton University Press.

Qu, X., and A. Hall (2006), Assessing snow albedo feedback in simulated climate change,*J. Clim.*, *19*(11), 2617–2630, doi:10.1175/JCLI3750.1.

Quan, X.-W., H. F. Diaz, and M. P. Hoerling (2004), Changes in the tropical Hadley cell since 1950, in *The Hadley Circulation: Present, Past, and Future*, edited by H. F. Diaz and R. S. Bradley, pp. 85–120, Cambridge Univ. Press, New York, doi:10.1007/978-1-4020-2944-8_3.

Ramanathan, V., and W. Collins (1991), Thermodynamics regulation of ocean warming by cirrus clouds deduced from observations of the 1987 El Nino, *Nature*, *351*, 27–32.

Randall, D. A., and D.-M. Pan, 1993: Implementation of the Arakawa-Schubert cumulus parameterization with a prognostic closure. In , a Meteorological Monograph published by the American Meteorological Society, K. Emanuel and D. Raymond, Eds., pp. 137 - 144.

Randall, D.A., R.A. Wood, S. Bony, R. Colman, T. Fichefet, J. Fyfe, V. Kattsov, A. Pitman, J. Shukla, J. Srinivasan, R.J. Stouffer, A. Sumi and K.E. Taylor, 2007: Climate Models and Their Evaluation. In: *Climate Change 2007: The Physical Science Basis. Contribution of Working Group I to the Fourth Assessment Report of the Intergovernmental Panel on Climate Change* [Solomon, S., D. Qin, M. Manning, Z. Chen, M.C. Marquis, K.B. Averyt, M.Tignor and H.L. Miller (eds.)]. Cambridge University Press, Cambridge, United Kingdom and New York, NY, USA, 996 pp.

Rasch, P. J., and J. E. Kristjánsson (1998), A comparison of the CCM3 model climate using diagnosed and predicted condensate parameterizations, *J. Clim.*, *11*, 1587–1614.

Read, W. G., et al. (2007), Aura Microwave Limb Sounder upper tropospheric and lower stratospheric H_2O and relative humidity with respect to ice validation, *J. Geophys. Res.*, *112*, D24S35, doi:10.1029/2007JD008752.

Reynolds, R. W., and D. C. Marsico (1993), An improved real-time global sea surface temperature analysis, *J. Clim.*, *6*, 114–119.

Reynolds, R. W., N. A. Rayner, T. M. Smith, D. C. Stokes, and W. Wang (2002), An improved in situ and satellite SST analysis for climate, *J. Clim.*, *15*, 1609–1625.

Rienecker, M. M., et al. (2011), MERRA: NASA's modern-era retrospective analysis for research and applications, *J. Clim.*, *24*, 3624–3648, doi:10.1175/JCLI-D-11-00015.1.

Rodgers, C. D., and C. D. Walshaw (1966), The computation of infra-red cooling rate in planetary atmospheres, *Q. J. R. Meteorol. Soc.*, *92*, 67–92.

Rotstayn, L. D. (2000), On the "tuning" of autoconversion parameterizations in climate models, *J. Geophys. Res.*, *105*(D12), 15,495–15,507, doi:10.1029/2000JD900129.

Ryoo, J.-M., T. Ugasa, and D. W. Waugh (2009), PDFs of tropospheric humidity, *J. Clim.*, *22*, 3357–3373.

Saha, S., et al. (2010), The NCEP climate forecast system reanalysis, *Bull. Am. Meteorol. Soc.*, *91*, 1015–1057, doi:10.1175/2010BAMS3001.1

Saji, N. H., B. N. Goswami, P. N. Vinayachandran, and T. Yamagata (1999), A dipole mode in the tropical Indian Ocean, *Nature*, *401*, 360–363, doi:10.1038/43854.

Salathé, E. P., and D. L. Hartmann (1997), A trajectory analysis of tropical upper-tropospheric moisture and convection, *J. Clim.*, *10*, 2533–2547.

Schoeberl, F., et al. (2006), Overview of the EOS Aura Mission, *IEEE Trans. Geosci. Remote Sens.*, *44*, 1066–1074.

Schwartz, M. J., et al. (2008), Validation of the Aura Microwave Limb Sounder temperature and geopotential height measurements, *J. Geophys. Res.*, *113*, D15S11, doi:10.1029/2007JD008783.

Seidel, D. J., and W. J. Randel (2007), Recent widening of the tropical belt: Evidence from tropopause observations, *J. Geophys. Res.*, *112*, D20113, doi:10.1029/2007JD008861.

Seidel, D. J., Q. Fu, W. J. Randel, and T. J. Reichler (2008), Widening of the tropical belt in a changing climate, *Nat. Geosci.*, *1*(1), 21–24.

Sherwood, S. C. (1996a), Maintenance of the free-tropospheric tropical water vapor distribution, part I: Clear regime budget, *J. Clim.*, *9*, 2903–2918.

Sherwood, S. C. (1996b), Maintenance of the free-tropospheric tropical water vapor distribution, part II: Simulation by large-scale advection, *J. Clim.*, *9*, 2919–2934.

Sherwood, S. C., and A. E. Dessler (2003), Convective mixing near the tropopause: Insights from seasonal variations, *J. Atmos. Sci.*, *60*(21), 2674–2685.

Sherwood, S. C., E. R. Kursinski, and W. G. Read (2006), A distribution law for free-tropospheric relative humidity, *J. Clim.*, *19*, 6267–6277, doi:10.1175/JCLI3978.1.

Sherwood, S. C., R. Roca, T. M. Weckwerth, and N. G. Andronova (2010), Tropospheric water vapor, convection, and climate, *Rev. Geophys.*, *48*, RG2001, doi:10.1029/2009RG000301.

Shin, S.-I., and P. D. Sardeshmukh (2011), Critical influence of the pattern of tropical ocean warming on remote climate trends, *Clim. Dyn.*, *36*, 1577–1591, doi:10.1007/s00382-009-0732-3.

Simmons, A., et al. (2006), ERA_Interim: New ECMWF reanalysis products from 1989 onwards, *, ECMWF Newsletter,*, *110, 25-35.*, Simmons, A., et al. (2006), ERA_Interim: New ECMWF reanalysis products from 1989 onwards, ECMWF Newsletter, 2110, 2025-2035.

Simmons, A., S. Uppala, D.P. Dee, and S. Kobayashi (2007), ERA_Interim: New ECMWF reanalysis products from 1989 onwards, *ECMWF Newsletter*, *110*, 25-35.

Smil, V. (2003), The Earth's Biosphere: Evolution, Dynamics, and Change, MIT Press., pp107.

Smith, R. N. B. (1990), A scheme for predicting layer clouds and their water content in a general circulation model, *Q. J. R. Meteorol. Soc.*, *116*, 435–460, doi:10.1002/qj.49711649210.

Sobel, A. H., I. M. Held, and C. S. Bretherton (2002), The ENSO signal in tropical tropospheric temperature, *J. Clim.*, *15*, 2702–2706.

Soden, B. J. (1997), Variations in the tropical greenhouse effect during El Niño, *J. Clim.*,*10*, 1050–1055.

Soden, B. J., and F. P. Bretherton (1994), Soden, B. J., and F. P. Bretherton (1994), Evaluation of water vapor distribution in general circulation models using satellite observations, *J. Geophys. Res.*, *99*(D1), 1187–1210, doi:10.1029/93JD02912.

Soden, B. J., and R. Fu (1995), A satellite analysis of deep convection, upper tropospheric humidity, and the greenhouse effect, *J. Clim.*, *8*, 2333–2351.

Soden, B. J., and J. R. Lanzante (1996), An assessment of satellite and radiosonde climatologies of upper-tropospheric water vapor, *Journal of Climate*, *9*(6), 1235-1250.

Soden, B. J., and I. M. Held (2006), An assessment of climate feedbacks in coupled ocean–atmosphere models, *J. Clim.*, *19*(14), 3354–3360, doi:10.1175/JCLI3799.1.

Soden, B. J., R. T. Wetherald, G. L. Stenchikov, and A. Robock (2002), Global cooling after the eruption of Mount Pinatubo: A test of climate feedback by water vapor,*Science*, *296*, 727–730.

Soden, B. J., D. L. Jackson, V. Ramaswamy, M. D. Schwarzkopf, and X. L. Huang (2005), The radiative signature of upper tropospheric moistening, *Science*, *310*, 841–844.

Solomon, S., D. Qin, M. Manning, Z. Chen, M. Marquis, K.B. Averyt, M. Tignor and , and H. L. M. (eds.) (2007), Contribution of Working Group I to the Fourth Assessment Report of the Intergovernmental Panel on Climate Change, Cambridge University Press, Cambridge, United Kingdom and New York, NY, USA, 996 pp.

Stephens, G. L. (1994), Remote Sensing of the Lower Atmosphere: An Introduction. Oxford Univ. Press, March 1994.

Stephens, G. L. (2005), Cloud feedbacks in the climate system: A critical review, *J. Clim.*, *18*, 237–273.

Stone, P. H., and J. H. Carlson (1979), Atmospheric lapse rate regimes and their parameterization, *J. Atmos. Sci.*, *36*, 415–423.

Su, H., and J. D. Neelin (2002), Teleconnection mechanisms for tropical Pacific descent anomalies during El Nino, *J. Atmos. Sci.*, *59*, 2694–2712.

Su, H., J. D. Neelin, and C. Chou (2001), Tropical teleconnection and local response to SST anomalies during the 1997–1998 El Niño, *J. Geophys. Res.*, *106*(D17), 20, 025–20, 043.

Su, H., D. Neelin, and J. E. Meyerson (2003), Sensitivity of tropical tropospheric temperature to sea surface temperature forcing, *J. Clim.*, *16*, 1283–1301.

Su, H., et al. (2008a), Variations of tropical upper tropospheric clouds with sea surface temperature and implications for radiative effects, *J. Geophys. Res.*, *113*, D10211, doi:10.1029/2007JD009624.

Su, H., J. H. Jiang, D. G. Vane, and G. L. Stephens (2008b), Observed vertical structure of tropical oceanic clouds sorted in large-scale regimes, *Geophys. Res. Lett.*, *35*, L24704, doi:10.1029/2008GL035888.

Su, H., W. G. Read, J. H. Jiang, J. W. Waters, D. L. Wu, and E. J. Fetzer (2006), Enhanced positive water vapor feedback associated with tropical deep convection: New evidence from Aura MLS,*Geophys. Res. Lett.*, *33*, L05709, doi:10.1029/2005GL025505.

Su, H., J. H. Jiang, J. Teixeira, A. Gettelman, X. Huang, G. Stephens, D. Vane, and V. S. Perun (2011), Comparison of regime-sorted tropical cloud profiles observed by CloudSat with GEOS5 analyses and two general circulation model simulations, *J. Geophys. Res.*, *116*, D09104, doi:10.1029/2010JD014971.

Sun, D. Z., and R. S. Lindzen (1993), Distribution of tropical tropospheric water vapor, *J. Atmos. Sci.*, *50*, 1644–1660.

Sun, D. Z., and I. M. Held (1996), A comparison of modeled and observed relationships between interannual variations of water vapor and temperature, *Journal of Climate*, *9*(4), 665-675.

Sun, D. Z., C. Covey, and R. S. Lindzen (2001), Vertical correlations of water vapor in GCMs, *Geophysical Research Letters*, *28*(2), 259-262.

Susskind, J., C. Barnet, J. Blaisdell, L. Iredell, F. Keita, L. Kouvaris, G. Molnar, and M. Chahine (2006), Accuracy of geophysical parameters derived from Atmospheric Infrared Sounder/Advanced Microwave Sounding Unit as a function of fractional cloud cover, *Journal of Geophysical Research-Atmospheres*, *111*(D9).

Tanaka, H. L., N. Ishizaki, and A. Kitoh (2004), Trend and interannual variability of Walker, monsoon and Hadley circulations defined by velocity potential in the upper troposphere, *Tellus, Ser. A*, *56*, 250–269.

Tao, W. K., et al. (2003), Microphysics, radiation and surface processes in the Goddard Cumulus Ensemble (GCE) model, *Meteorol. Atmos. Phys.*, *82*, 97–137, doi:10.1007/s00703-001-0594-7.

Thompson, R. M. Jr., S. W. Payne, E. E. Recker, and R. J. Reed (1979), Structure and properties of synoptic-scale wave disturbances in the intertropical convergence zone of the eastern Atlantic, *J. Atmos. Sci*, *36*, 53–72.

Tiedtke, M. (1989), A comprehensive mass flux scheme for cumulus parameterization in large-scale models, *Mon. Weather Rev.*, *117*, 1779–1800.

Tiedtke, M. (1993), Representation of clouds in large-scale models, *Mon. Weather Rev.*,*121*, 3040–3061.

Trenberth, K., J. Fasullo, and L. Smith (2005), Trends and variability in column-integrated atmospheric water vapor, *Clim. Dyn.*, *24*(7–8), 741–758, doi:10.1007/s00382-005-0017-4.

Udelhofen, P. M., and D. L. Hartmann (1995), Influence of tropical cloud systems on the relative humidity in the upper troposphere, *J. Geophys. Res.*, *100*, 7423–7440.

Uppala, S., Dee, D., Kobayashi, S., Berrisford, P., and A. Simmons (2008), Towards a climate data assimilation system: status update of ERA Interim, *ECMWF Newsletter*, *115*, 12-18.

Uppala, S., P. Kallberg, A. Hernandez, S. Saarinen, M. Fiorino, X. Li, K. Onogi, N. Sokka, U. Andrae, V. Da Costa Bechtold (2004), ERA-40: ECMWF 45-year reanalysis of the global atmosphere and surface conditions 1957-2002. ECMWF Newsletter No. 101 - Summer/Autumn 2004: 2-21.

Uppala, S. M., et al. (2005), The ERA-40 re-analysis, *Q. J. R. Meteorol. Soc.*,*131*(612), 2961–3012, doi:10.1256/qj.04.176.

Vecchi, G. A., and B. J. Soden (2007), Global warming and the weakening of the tropical circulation, *J. Clim.*, *20*, 4316–4340, doi:10.1175/JCLI4258.1.

Vecchi, G. A., B. J. Soden, A. T. Wittenberg, I. M. Held, A. Leetmaa, and M. J. Harrison (2006), Weakening of the tropical Pacific atmospheric circulation due to anthropogenic forcing, *Nature*, *441*(7089), 73–76, doi:10.1038/nature04744.

Vinayachandran, P. N., N. H. Saji, and T. Yamagata (1999), Response of the equatorial Indian Ocean to an unusual wind event during 1994, *Geophys. Res. Lett.*, *26*(11), 1613–1616.

Waliser, D. E., et al. (2009), Cloud ice: A climate model challenge with signs and expectations of progress, *J. Geophys. Res.*, *114*, D00A21, doi:10.1029/2008JD010015.

Wallace, J. M. (1992), Effect of deep convection on the regulation of tropical sea surface temperature, *Nature*, *357*, 230–231.

Wallace, J. M., and D. S. Gutzler (1981), Teleconnections in the geopotential height field during the Northern Hemisphere winter, *Mon. Weather Rev.*, *109*, 784–812.

Waters, J. W., et al. (2006), The Earth Observing System Microwave Limb Sounder (EOS MLS) on the Aura satellite, *IEEE Trans. Geosci. Remote Sens.*, *44*, 1075–1092.

Webster, P. J., A. M. Moore, J. P. Loschnigg, and R. R. Leben (1999), Coupled ocean-atmosphere dynamics in the Indian Ocean during 1997–98, *Nature*, *401*, 356–360, doi:10.1038/43848.

Wielicki, B. A., et al. (2002), Evidence for large decadal variability in the tropical mean radiative energy budget, *Science*, *295*, 841–844, doi:10.1126/science.1065837.

Wong, T. B. A., R. B. Wielicki, I. I. I. Lee, G. L. Smith, K. A. Bush, and J. K. Willis(2006), Reexamination of the observed decadal variability of the Earth

radiation budget using altitude-corrected ERBE/ERBS nonscanner WFOV data, *J. Clim.*, *19*, 4028–4040, doi:10.1175/JCLI3838.1.

Wright, J. S., R. Fu, and A. J. Heymsfield (2009), A statistical analysis of the influence of deep convection on water vapor variability in the tropical upper troposphere, Atmos,*Chem. Phys.*, *9*, 5847–5864, doi:10.5194/acp-9-5847-2009.

Wu, D. L., J. H. Jiang, and C. P. Davis (2006), EOS MLS cloud ice measurements and cloudy-sky radiative transfer model, *IEEE Trans. Geosci. Remote Sens.*, *44*, 1156–1165, doi:10.1109/TGRS.2006.869994.

Wu, D. L., J. H. Jiang, W. G. Read, R. T. Austin, C. P. Davis, A. Lambert, G. L. Stephens, D. G. Vane, and J. W. Waters (2008), Validation of the Aura MLS cloud Ice Water Content (IWC) measurements, *J. Geophys. Res.*, *113*, D15S10, doi:10.1029/2007JD008931.

Wu, D. L., R. T. Austin, M. Deng, S. L. Durden, A. J. Heymsfield, J. H. Jiang, A. Lambert, J. L. Li, N. J. Livesey, G. M. McFarquhar, J. V. Pittman, G. L. Stephens, S. Tanelli, D. G. Vane, and D. E. Waliser (2009), Comparisons of global cloud ice from MLS, CloudSat, and correlative data sets, *Journal of Geophysical Research-Atmospheres*, *114*.

Xie, P., J. E. Janowiak, P. A. Arkin, R. Adler, A. Gruber, R. Ferraro, G. J. Huffman and S. Curtis (2003), GPCP pentad precipitation analyses: An experimental dataset based on gauge observations and satellite estimates, *J. Clim.*, *16*, 2197–2214.

Xie, S.-P., C. Deser, G. A. Vecchi, J. Ma, H. Teng, and A. T. Wittenberg (2010), Global warming pattern formation: Sea surface temperature and rainfall, *J. Clim.*, *23*, 966–986, doi:10.1175/2009JCLI3329.1.

Xie, S.-P., and S. G. H. Philander (1994), A coupled ocean-atmosphere model of relevance to the ITCZ in the eastern Pacific, *Tellus A*, *46*, 340–350.

Xu, K.-M., and K. A. Emanuel (1989), Is the tropical atmosphere conditionally unstable?,*Mon. Weather Rev.*, *117*, 1471–1479.

Yukimoto S, N. A., Kitoh A, Sugi M, Kitamura Y, Hosaka M, Shibata K, Maeda S, Uchiyama T (2001), The new Meteorological Research Institute coupled GCM (MRI-CGCM2)—Model climate and variability. *Pap Meteor Geophys*, 2051:2047–2088.

Zelinka, M. D., and D. L. Hartmann (2010), Why is longwave cloud feedback positive?, *J. Geophys. Res.*, *115*, D16117, doi:10.1029/2010JD013817.

Zelinka, M. D., S.A. Klein, and D.L. Hartmann (2011), Computing and Partitioning Cloud Feedbacks using Cloud Property Histograms. Part I: Cloud Radiative Kernels. J. Climate, December 2011, *doi:10.1175/JCLI-D-11-00248.1*.

Zhang, G. J., and N. A. McFarlane (1995), Sensitivity of climate simulations to the parameterization of cumulus convection in the Canadian climate centre general circulation model, *Atmos. Ocean*, *33*, 407–446, doi:10.1080/07055900.1995.9649539.

Zhang, M., and H. Song (2006), Evidence of deceleration of atmospheric vertical overturning circulation over the tropical Pacific, *Geophys. Res. Lett.*, *33*, L12701, doi:10.1029/2006GL025942.

Zhang, M., W. Lin, C. S. Bretherton, J. J. Hack, and P. J. Rasch (2003), A modified formulation of fractional stratiform condensation rate in the NCAR Community Atmospheric Model (CAM2), *J. Geophys. Res.*, *108*(D1), 4035, doi:10.1029/2002JD002523.